Synthesis and application of multifunctional iron oxide-graphene oxide nanocomposite materials for sulfur pollutant removal

Amanda Ineza Mugisha

A thesis submitted in partial fulfillment of the requirements for the Master of Applied Science degree in Chemical Engineering

Department of Chemical and Biological Engineering
Faculty of Engineering
University of Ottawa
August 2024

Abstract

Sulfur pollution mainly comes from the utilization of fossil fuels, which contain sulfur compounds such as thiol, sulfide, and thiophene. Their combustion releases in the atmosphere sulfur dioxide (SO_2), a toxic gas harmful to both the environment and human health. Petroleum refineries also generate wastewater with reactive and odorous sulfide compounds. To address these issues, this work proposes the synthesis of a multifunctional composite material consisting of graphene oxide (GO)-iron oxide. This material is proposed to be used as an adsorbent for the capture of gaseous SO_2 at room temperature and as a catalyst for the oxidation of organic sulfide compounds to sulfone and sulfoxide, applicable in fuel desulfurization or wastewater treatment processes.

The properties and SO_2 capture capacities of GO-iron oxide material, obtained from the wet deposition of iron oxide nanoparticles on GO, were evaluated by studying the impact of different nanoparticle synthesis preparations. Three different methods were used: a polyol method and two co-precipitation methods, using either sodium hydroxide (NaOH) or ammonium hydroxide (NH_4OH) as reducing agents. The deposition of iron nanoparticles on the GO surface was confirmed through transmission electron microscopy (TEM), showing dispersed and round-shaped nanoparticles of less than 10 nm. In all cases, iron was mostly found in the Fe^{3+} oxidation state. However, the final iron content in the GO-iron oxide materials after wet deposition was different for each nanoparticle synthesis method, as indicated by Inductively coupled plasma atomic emission spectroscopy (ICP-OES) analysis. The breakthrough curves and the capacity calculations showed that the material containing nanoparticles from NH_4OH reduction had the highest capture capacity (3.1 mg $SO_2/g_{sorbent}$), five times greater than pristine GO. However, the SO_2 capture capacities based on iron content were respectively 114.1, 207.0, and 207.2 mg SO_2/g_{Fe} for $GOFe_2O_3$-polyol, $GOFe_2O_3$-NaOH, and $GOFe_2O_3$-NH4, suggesting that both the type and concentration of nanoparticles influence the capacity. Additionally, based on X-ray photoelectron spectroscopy (XPS) analysis, it was suggested that the adsorbed SO_2 might interact with iron oxide or directly to the surface of GO. The regeneration tests indicated incomplete desorption at 100°C, with capture capacity decreasing after the first cycle and stabilizing after the second cycle.

The catalytic activity of GO-iron oxide was also tested at 50°C using thioanisole as organic sulfide. In this case, iron magnetite nanoparticles were synthesized using co-precipitation and deposited on GO through wet deposition as well. The addition of magnetite was confirmed through

TEM, Fourier-transform infrared spectroscopy (FTIR), UV absorption, and X-ray powder diffraction (XRD). GO-Fe_2O_3 presented interesting catalytic activity with the oxidation of thioanisole to heavy sulfone compounds with 64.2% conversion. The addition of H_2O_2 increases the conversion to 92.8%. The photocatalytic activity of the material was accessed using UV, sunlight, and visible light in the absence of H_2O_2. UV light promotes the highest conversion with 89.6% followed by sunlight (77.7%) and visible light (75.2%).

These results suggest that graphene oxide-iron oxide has potential for SO_2 adsorption and catalytic oxidation of organic sulfide compounds. However, further optimization of the system and material is necessary for a more comprehensive evaluation. For instance, multiple regeneration cycles in the case of SO_2 capture have to be done to ensure the material's capacity stability over time. Additional analyses, such as XRD and high-resolution transmission electron microscopy (HR-TEM), are required to confirm the exclusive presence of Fe_2O_3. Increasing the iron concentration could facilitate the use of XPS to identify the interaction of SO_2 with the material. Finally, studying the effect of the nanoparticle size in the case of organic sulfide oxidation could enhance the photocatalytic activity of the GO-Fe_2O_3 material under low-energy light sources like visible light.

Keywords : sulfur dioxide; adsorption; oxidation; organic sulfide; catalyst; iron oxide; desulfurization, photocatalyst

Résumé

La pollution par le soufre provient principalement de l'utilisation de combustibles fossiles, qui contiennent des composés soufrés tels que le thiol, le sulfure et le thiophène. Leur combustion libère dans l'atmosphère du dioxyde de soufre (SO_2), un gaz toxique nocif pour l'environnement et la santé humaine. Les raffineries de pétrole génèrent également des eaux usées contenant des composés sulfureux réactifs et odorants. Pour répondre à ces problèmes, ce travail propose la synthèse d'un matériau multifonctionnel composé d'oxyde de graphène (GO) et d'oxyde de fer. Ce matériau est proposé pour être utilisé comme adsorbant pour la capture du SO_2 gazeux à température ambiante et comme catalyseur pour l'oxydation des composés sulfureux organique en sulfone et sulfoxide, applicable dans les processus de désulfuration des combustibles ou de traitement des eaux usées.

Les propriétés et les capacités de capture du SO_2 du matériau GO-oxyde de fer, obtenu par dépôt humide de nanoparticules d'oxyde de fer sur le GO, ont été évaluées en étudiant l'impact de différentes méthodes de synthèse de nanoparticules. Trois méthodes différentes ont été utilisées : une méthode polyol et deux méthodes de co-précipitation, utilisant soit de l'hydroxyde de sodium (NaOH) soit de l'hydroxyde d'ammonium (NH_4OH) comme agents réducteurs. Le dépôt de nanoparticules de fer sur la surface du GO a été confirmé par microscopie électronique à transmission (TEM), montrant des nanoparticules dispersées et de forme ronde de moins de 10 nm pour les nanoparticules de co-précipitation. Dans tous les cas, le fer se trouvait principalement à l'état d'oxydation Fe_{3+}. Cependant, la teneur finale en fer dans les matériaux GO-oxyde de fer après dépôt humide variait selon chaque méthode de synthèse de nanoparticules, comme l'indique l'analyse par spectrométrie d'émission atomique à plasma inductif (ICP-OES). Les courbes de percée et les calculs de capacité ont montré que le matériau contenant les nanoparticles proveant de la réduction avec NH_4OH avait la plus grande capacité de capture (3.1 mg $SO_2/g_{adsorbant}$), cinq fois supérieure à celle du GO pur. Cependant, les capacités de capture du SO_2 basées sur la teneur en fer étaient respectivement de 114.1, 207.0 et 207.2 mg SO_2/g_{Fe} pour $GOFe_2O_3$-polyol, $GOFe_2O_3$-NaOH et $GOFe_2O_3$-NH_4, suggérant que le type et la concentration des nanoparticules influencent la capacité. De plus, selon l'analyse par spectroscopie photoélectronique à rayons X (XPS), il a été suggéré que le SO_2 adsorbé pourrait interagir avec l'oxyde de fer ou directement avec la surface du GO. Les tests de régénération ont indiqué une désorption incomplète à 100°C,

avec une capacité de capture diminuant après le premier cycle et se stabilisant après le deuxième cycle.

L'activité catalytique du GO-oxyde de fer a également été testée à 50°C en utilisant du thioanisole comme organique sulfure. Dans ce cas, des nanoparticules de magnétite de fer ont été synthétisées par co-précipitation et déposées sur le GO par dépôt humide également. L'ajout de magnétite a été confirmé par TEM, spectroscopie infrarouge à transformée de Fourier (FTIR), absorption UV et diffraction des rayons X (XRD). GO-Fe_3O_4 a présenté une activité catalytique intéressante avec l'oxydation du thioanisole en composés de sulfone lourds avec une conversion de 64,2%. L'ajout de H_2O_2 augmente la conversion à 92,8%. L'activité photocatalytique du matériau a été évaluée en utilisant des UV, la lumière du soleil et la lumière visible en l'absence de H_2O_2. La lumière UV favorise la conversion la plus élevée avec 89,6%, suivie par la lumière du soleil (77,7%) et la lumière visible (75,2%).

Ces résultats suggèrent que l'oxyde de graphène-oxyde de fer a un potentiel pour l'adsorption du SO_2 et l'oxydation catalytique des composés sulfureux organiques. Cependant, une optimisation supplémentaire du système et du matériau est nécessaire pour une évaluation plus complète. Par exemple, il est nécessaire de réaliser plusieurs cycles de régénération dans le cas de la capture du SO_2 pour garantir la stabilité de la capacité du matériau dans le temps. Des analyses supplémentaires, telles que la diffraction des rayons X (XRD) et la microscopie électronique à transmission haute résolution (HR-TEM), sont requises pour confirmer la présence exclusive de Fe_2O_3. Augmenter la concentration en fer pourrait faciliter l'utilisation de la XPS pour identifier l'interaction du SO_2 avec le matériau. Enfin, étudier l'effet de la taille des nanoparticules dans le cas de l'oxydation des organiques sulfures pourrait améliorer l'activité photocatalytique du matériau GO- Fe_3O_4 sous des sources de lumière à faible énergie comme la lumière visible.

Mots clés : dioxyde de soufre; adsorption; oxydation; soufre organique; catalyseur; oxyde de fer; désulfuration; photocatalyseur.

Statement of Contributors or Collaborators and Co-authorship

I hereby declare that I am the sole author of this thesis.

Chapter 1 was solely authored by me with editorial comments by Prof. Clémence Fauteux-Lefebvre. This chapter provides a literature review on commonly used adsorbents for sulfur dioxide capture and the reactions employed for organic sulfide oxidation. It concludes with a presentation of the research objectives.

Chapter 2 was written by me with editorial comments by Prof. Clémence Fauteux-Lefebvre. The SO_2 capture experiments, the breakthrough curves analysis, and the capture capacity calculation were conducted by me. The setup of the SO_2 capture montage was done by me in collaboration with student Samuel Karki (master's student of prof. Fauteux-Lefebvre) and the technicians Franco Ziroldo, Gérard Nina. TEM, ICP-OES, and XPS sample preparation were performed by me and the sample analyses were respectively effectuated by Dr. Yun Liu and Nelson Rutajoga with MatChar at the University of Ottawa. XPS characterizations were conducted by Dr Lihong Shang from McGill University and part of the curve fitting analysis was done by me. This chapter will be submitted as an article.

Chapter 3 was written by me with editorial comments by Profs. Carlos Alberto Huerta Aguilar and Clémence Fauteux-Lefebvre. The synthesis of metal nanoparticles and the nanomaterial composite (graphene oxide-iron oxide) was carried out by me. The study of the impact of the surfactant (sucrose) and the stabilizing agent (citric acid) on nanoparticle synthesis was conducted by me. Thioanisole oxidation experiments were performed by me and Prof. Aguilar at Tecnológico de Monterrey, Puebla, Mexico. HPLC samples preparation and characterization, the kinetic study of the thioanisole oxidation reactions, and the atomic absorption samples analysis were conducted by me with the support of Prof. Aguilar. HRTEM was conducted by Carlos Alberto Camacho at Tecnológico de Monterrey, Puebla, Mexico. XRD, SAED, FTIR, UV-Vis, and GC-MS sample preparation and characterization were conducted by Prof. Aguilar at Tecnológico de Monterrey, Puebla, Mexico. This work will be included in an article to be submitted.

Chapter 4 is the conclusion and presents the possible future work on the topic. It was solely authored by me with editorial comments by Prof. Fauteux-Lefebvre.

Appendices were solely authored by me.

Acknowledgments

I would like to express my profound gratitude to my supervisor, Prof. Clémence Fauteux-Lefebvre, for her immense support and guidance throughout this project. Her expertise, along with her patience, understanding, and encouragement, provided invaluable support during this research and played a crucial role in the completion of this thesis.

I would like to express my sincere thanks to Prof. Carlos Alberto Huerta Aguilar at Tecnológico de Monterrey, Puebla, Mexico, for his support and active participation during and after my research at Tecnológico de Monterrey, and Prof. Alma Cuellar for her continuous support throughout my research stay at Tecnológico de Monterrey.

I wish to thank Dr. Yun Liu for assisting with the TEM analysis, and Nelson Rutajoga for the ICP-OES analysis. I would like to also thank Frantz Célestin for handling off-campus sample shipments, and technicians Franco Ziroldo, and Gérard Nina for their technical and mechanical support in improving the capture setup. Thanks to Babak Shalchi at CanmetMaterials for the TEM analysis and Dr. Lihong Shang from McGill University for the XPS analysis.

Acknowledgments to the Natural Sciences and Engineering Research Council of Canada (NSERC), the International Experiment Scholarships (EIS), and the University of Ottawa for their financial support.

I would like to extend my sincere thanks to my lab mates, Xinlong Chen, Samuel Karki, and Joanne Woloszyn, as well as to the undergraduate student I had the privilege of supervising, David Omayeke, for their assistance throughout the project.

Finally, I would like to thank my parents, friends, and my fiancé, whose continual support was essential in completing this thesis.

I dedicate this thesis to my parents, to whom I owe an immense debt of gratitude for their unwavering support and love.

Mr. Mugisha Pierre and Mrs. Jeanne Butozi Furaha.

Table of Contents

List of Figures

List of Tables

Abbreviations and Symbols

FGD	Flue gas desulfurization
GO	Graphene oxide
AC	Activated carbon
CNTs	Carbon nanotubes
SWCNT	Single walls carbon nanotube
DFT	Density functional theory
HDS	Hydrodesulfurization
ODS	Oxidative desulfurization
NaOH	Sodium hydroxide
NH_4OH	Ammonium hydroxide
H_2O_2	Hydrogen peroxide
CA	Citric acid
Scr	Sucrose
UV	Ultraviolet
UV-Vis	Ultraviolet-visible
HPLC	High-performance liquid chromatography
GC-MS	Gas chromatography-mass spectrometry
FTIR	Fourier transform infrared spectroscopy
XRD	X-Ray diffraction
XPS	X-Ray photoelectron spectroscopy
ICP-OES	Inductively coupled plasma atomic emission spectroscopy
HRTEM	High-resolution transmission electron microscopy

Chapter 1. Introduction

1.1. A pollutant named sulfur

Sulfur is an essential element. In living organisms, it appears in cysteine and methionine amino acids, used to make proteins [1]. Moreover, sulfur is required for the production of sulfuric acid used in the production of fertilizers, wood preservatives, automobile batteries [2,3]. However, certain sulfur compounds, such as sulfides and sulfur oxides, are toxic to the environment and health. Petroleum, natural gas, and other fossil fuels constitute the primary source of sulfur pollution. In 2013, they represented 57.2% of global sulfur production [1]. Natural gas from commercial fields can contain up to 20% hydrogen sulfide (H_2S) while typical crude oil may contain up to 5 wt% sulfur compounds such as thiol, sulfides, thiophenes [1,4].

Sulfur compounds are undesirable in liquid fuels due to their numerous harmful effects. They cause corrosion in refining equipment and the premature failure of combustion engines [4,5]. H_2S and other sulfide molecules are highly reactive with metals, causing damage to storage tanks and pipelines, which leads to high maintenance costs. Sulfur also contributes to catalyst poisoning in the refining process [4,5]. The sulfur species adsorbed on the surface or active sites of the metals in the catalysts formed metal sulfide, causing inactivation or reduction of the catalytic activity. In addition, wastewater generated by fuel refining processes contains reactive and odorous sulfur such as hydrogen sulfide and mercaptans [6,7].

During combustion processes, the sulfur present in fuel is converted to sulfur oxide (SO_x) and released into the atmosphere if not captured properly. Sulfur dioxide (SO_2) represents about 90% of ambient SO_x [1]. SO_2 poses significant risks to human health, causing the deterioration of the respiratory system and an elevated risk of heart disease, while also impacting the environment [8,9]. In the atmosphere, hydroxyl radicals oxidize SO_2, leading to the formation of sulfuric acid in the presence of water [9]. Sulfuric acid contributes to soil deterioration, the formation of acid fog, and destabilization of aquatic ecosystems [9,10]. Dry acid deposition, a result of SO_2 emissions, further accelerates the degradation of building materials, stones, and status which increases the maintenance costs [9,10].

1.2. Sulfur dioxide emission control challenges

In Canada, the primary anthropogenic source of SO_2 emission comes from the combustion of fossil fuels such as oil, coal, natural gas [11]. In 2021, the oil and gas industries held 41% of the total national SO_x, electric power generation for 26%, and ore and mineral industries accounted for 25% of total SO_x emissions [12].

The SO_x emissions in Canada decreased by 79% between 1990 and 2021 [12]. This reduction is attributed to several factors, including the closure of coal-fired power plants and major smelters, the reduction of coal consumption, the adoption of low-sulfur heavy fuel oil, and the implementation of pollution control equipment [12].

Controlling SO_2 emissions can be achieved either through pre-combustion removal of sulfur from the fuel or by implementing post-combustion desulfurization treatments on the exiting flue gas. However, obtaining cleaner fuel is expensive and can alter fuel efficiency, hence why most of the emission control focuses on post-combustion treatments [13,14]. Post-combustion treatment involves using flue gas desulfurization (FGD) techniques, which include a range of methods to remove SO_2 from industrial combustion exhaust gases. FGD techniques such as wet scrubbers, spray dry absorption, and sorbent injection are the most used technologies for SO_2 removal at the industrial level mainly due to their simplicity and high desulfurization capacity [13,14]. Other methods, including biological and electronic technologies, are currently being studied for their potential to achieve high-efficiency sulfur removal. Electronic techniques, which use electron beam irradiation, come with drawbacks such as high costs, significant energy consumption, and high safety protection. Meanwhile, biological methods are heavily dependent on water [13].

1.2.1. Flue gas desulfurization (FGD) – wet and dry scrubbers

In most currently used FGD techniques, a suitable alkaline sorbent is brought into contact with the SO_2 gas present in the flue gas and reacts to produce sulfite and or sulfate compounds [15]. The physical characteristics of these compounds vary from sludge to a dry powdered material depending on the process [16]. These FGD processes can be categorized as wet FGD, dry, and semi-dry FGD based on the amount of water used [13,15,17].

Wet scrubber methods, also known as wet FGD, represent more than 80% of the desulfurization techniques used in coal-fired plants [15,17]. These techniques are well established and can achieve removal efficiencies up to 99% [15,17,18]. In wet FGD systems, the sorbents are

typically in a slurry or solution form, and a counter-current spray tower is used as the absorption column [15,19]. In addition to allowing a larger contact surface between the gas and liquid, spray towers are simple scrubbers that help prevent scale buildup, clogging, or erosion, which affect FGD reliability and absorber efficiency [20]. Limestone (calcium carbonate) is the most common reagent used, owing to its accessibility and cost-effectiveness. Limestone reacts with SO_2 in flue gas to form a calcium sulfite slurry. This slurry is then oxidized to produce calcium sulfate, commonly known as gypsum [15]. Alternative sorbents such as calcium oxide (quicklime) and calcium hydroxide (hydrated lime), derived from limestone calcination, offer enhanced reactivity but are expensive [15]. Other sorbents utilized include ammonia, magnesium carbonate, and sodium-based compounds [15].

Despite their effectiveness, wet FGD systems have high capital and operating costs due to their reliance on water and heat. During the process, flue gas becomes saturated with water, requiring evaporation. A significant portion of the feed water evaporates and exits with the flue gas, while the remaining water, filled with gypsum and other impurities (chlorides, heavy metals) is treated in a water treatment plant before discharge [15,17]. They also require corrosion-resistant materials due to the presence of highly corrosive gases [13,15]. Moreover, the reaction between limestone and SO_2 results in the formation of carbon dioxide (CO_2), which is emitted alongside the scrubbed flue gas, contributing to CO_2 emissions [15]. Wet FGD systems are primarily used for high SO_2 concentration [22] (sulfur fuel content up to 3.5% [17]). Under low concentrations, longer columns and more water will be required to maximize the contact time which will further increase the costs.

Spray dry scrubbers, also called semi-dry FGD, are the second most widely used FGD technology. It utilizes lime (quicklime or hydrated lime) as the primary sorbent [17]. Hot flue gases are mixed in a spray dryer vessel with a mist of finely atomized fresh lime slurry which absorbs and reacts with SO_2 while almost simultaneously drying [19,23]. Factors influencing the absorption chemistry include flue gas temperature, SO_2 concentration, and the size of the sprayed slurry droplets [17]. Spray dry scrubbers offer the advantage of having dry products that are easier to dispose of; however, they achieve a sulfur removal efficiency not greater than 90%. [17].

Finally, sorbent injection, categorized as dry desulfurization technologies, was developed for lower sulfur content fuel where wet FGD was not cost-effective [15,17,23]. Depending on the injection point of the sorbent, four types are distinguished: furnace sorbent injection, economizer sorbent injection, duct sorbent injection, and hybrid sorbent injection (a combination of two points

of injection). In a dry injection system, there is no dedicated absorber column, a dry hydrated calcium or sodium-based sorbent, in powder or pellet form is directly brought into contact with the flue gas at the injection point. The sorbent reacts with SO_2 and the produced sulfate solid and the unreacted remaining sorbent are collected in a particulate control device (a baghouse) [17,19]. Some of the solids are recirculated to the reaction and the rest is sent to disposal. Sorbent injection systems offer advantages such as relatively low capital and operating costs, easy retrofitting, and easy operation and maintenance with no slurry handling. However, they typically achieve only about 50% sulfur removal efficiency and the sorbent is expensive compared to the one used in wet FGD [17].

1.2.2. Adsorption

Adsorption has been an attractive dry FGD method due to the water-free operation, the simplicity of the process, and the affordability of certain adsorbents such as activated carbon, zeolites, and metal oxide, which can be derived from waste materials or can be found naturally [13,24,25]. The adsorbents can be regenerated through chemical or physical treatments, reducing the costs associated with their use, and the generated SO_2 can be converted to sulfuric acid [13]. Although regeneration is possible with wet FGD, it further increases the capital and operating costs [13]. Moreover, physical adsorption typically occurs at low temperatures, near room temperature, thus reducing the energy demands. This technique is effective for gas streams containing low levels of SO_2 [22], which is advantageous given increasingly stringent regulations on SO_2 emissions [21]. It can serve as a complementary technique when a very pure outlet gas is required or can be used alone when the exhaust gas contains low SO_2 concentrations (less than 500 ppm [22]). However, the capture efficiency of this technique is still much lower compared to wet FGD and therefore not yet widely used on an industrial scale [13]. Numerous studies are being conducted to improve the capture capacity of existing adsorbents [25–30] or even create new adsorbents with enhanced capture capacity [31]. Carbonaceous materials, including activated carbon, carbon nanotubes, and graphene oxide are particularly studied as adsorbents for SO_2 removal due to their high surface area and high stability against moisture and corrosive gases [30].

<u>Activated carbon</u>

Activated carbon is distinguished by its high surface area, good porosity distribution, and high surface reactivity [13,32]. Research conducted by Raymundo-Pinero et al. indicates that the SO_2

adsorption potential of activated carbon is related to the structure and porosity of the carbon material, the chemical nature of the surface, and the adsorption site's oxidation capacity [33]. They noted that increasing the pore size of activated carbon fibers through heat treatment enhances SO_2 adsorption but reduces its oxidation to SO_3, which in turn diminishes the overall adsorption capacity. On the other hand, activated carbon with smaller pore sizes and uniform porosity exhibits lower SO_2 adsorption and oxidation capacity compared to activated carbon fibers with the same pore dimensions [33]. These observations highlight the influence of the material structural configurations on its adsorption capacity [33–35].

The effect of surface functionalization on SO_2 absorption was explored in several studies [26,27,36,37]. The research conducted by Zhao et al. revealed that activated carbons with more oxygen groups have higher catalytic activity [36]. They explained that this enhancement was due to the presence of carbonyl and ketene oxygen groups on the surface, which possess C=O bonds with Bronsted basic properties [26,36,37]. Given that SO_2 is an acidic gas, it is initially adsorbed onto these basic active sites and subsequently transformed into adsorbed SO_3 and H_2SO_4 in the presence of oxygen and water vapor in the system [26,36]. Expanding on this, Liu Xiao-Li and colleagues investigated the effect of adding iron oxide to both nitric acid-treated activated carbon and untreated activated carbon. Their findings indicate that the addition of iron oxide nanoparticles improves SO_2 removal by increasing the average pore size, which allows gas molecules to move freely, and enhancing the catalytic oxidation, as evidenced by the higher yields of SO_4^{2-} [26]. However, iron oxide and the generated adsorbed H_2SO_4 lead to the formation of $Fe_2(SO_4)_3$, which can block the micropores and ultimately deactivate the carbon material [26].

In addition to the surface functionalization of adsorbents, numerous studies have shown that the presence of oxygen and water in flue gases influences the adsorption of SO_2 on activated carbon [27,34,38]. Falk et al. studied the adsorption of SO_2 on activated carbon under various gas conditions, maintaining a temperature constant of 30°C [34]. The results indicated that the capture efficiency increases in the presence of water and oxygen. SO_2 desorption was not observed following the desorption cycle with pure nitrogen at 30°C, but SO_2 adsorbed under dry air conditions did desorb [34]. This was explained by the oxidation of SO_2, by the adsorbed O_2 from flue gas, resulting in the formation of SO_3, which reacts rapidly with H_2O to form H_2SO_4 [34].

Martin et al. explained that the reversible and irreversibly SO_2 adsorbed on their activated carbon can be attributed to physiosorbed SO_2 and chemisorbed species such as SO_3 [39]. Paoli

Davini demonstrated that adding metal, especially vanadium and iron, further enhances the capture capacity of SO_2 in the presence of water and oxygen [27].

While activated carbons are cost-effective, they typically require chemical and/or thermal pre-treatments to improve their adsorption capacities. Additionally, the consumption of carbon by oxidation at high-temperature limit the sorbent life after repeated adsorption-regeneration cycles [14].

Carbon nanotubes

Carbon nanotubes (CNTs) are made of rolled-up sheets of single-layer or multi-layer graphene [40]. They have emerged as attractive adsorbents for gas pollutant removal mainly due to their highly porous structure and large surface area, comparable to activated carbon [41,42]. They also have high chemical stability and corrosion resistance [30]. Gas molecules can be adsorbed on both the outer and inner surfaces of CNTs [41,43]. The strong Van der Waal forces between tubes cause them to form bundles, creating additional adsorption sites within the interstitial channels and at the periphery of the bundles where two adjacent parallel CNTs meet (also called groove sites) [41,43].

The external sites, being directly accessible to the adsorbate, are where most adsorption typically occurs [41]. The chemically inert nature of the surface makes the adsorption to be predominantly physisorption [41]. The effectiveness of SO_2 adsorption on CNTs is enhanced by larger diameters [29,42]. Sun et al. demonstrated that the SO_2 adsorption phenomena on CNTs is physisorption in the low-temperature range and changes to chemisorption at a high-temperature range [44]. This change was attributed to the contribution of electrons from delocalized pi-bonds in aromatic rings, forming Lewis basic sites capable of chemically adsorbing acid gases [44].

Functionalization of CNTs, metal doping, or creating vacancy defects are effective methods for improving their adsorption capacities [28,29,43,45,46]. Mehdi Yoosefian et al. investigate the adsorption capacity of CNTs for SO_2 by creating vacancy defects in a single-walled CNT (SWCNT) and replacing the carbon atoms with Pt noble metal [47]. Using density functional theory (DFT), they investigate the adsorption of single and double SO_2 gas molecules in two orientations with the oxygen or sulfur atom near the metal. The DFT analysis revealed stronger adsorption in the configuration oxygen-Pt/SWCNT and higher adsorption energy for the second SO_2 molecule, suggesting the influence of the first adsorbed molecule [47]. Natural bond orbital analysis showed a charge transfer from the SWCNT to the SO_2 molecule [47]. Libao et al. also

observed an increase in charge transfer from metal-doped CNT to SO_2 molecule when investigating the adoption capacity of pristine CNTs, metal-doped CNTs with and without vacancy defects [28]. Their DFT analysis demonstrated enhanced adsorption with vacancy-defected CNTs and even higher with Fe-doped CNTs. The latter decreased the adsorption distance by up to 44.8%, and increased the adsorption energy and the charge transfer, suggesting chemical adsorption on Fe-doped CNTs compared to weak physical adsorption on pristine CNTs These metals offer more active sites than the carbon atoms and can form stable chemical structures [28]. The presence of vacancy defects in CNTs induces magnetic moments, enhancing the reactivity of C atoms at defects and the S atom can stabilize these defects through the formation of an S-C bond [28,45].

Zhang et al. used DFT and experimental studies to investigate the effect of hydroxyl groups on carbon nanotubes for sulfur hexafluoride (SF6) decomposed gases (SO_2F_2, SOF_2, SO_2, and CF_4) adsorption. Their studies showed that SWCNT-OH had the highest sensitivity to SO_2 compared to the other gases [48]. Moreover, Zhang et al. investigated the sensitivity of carboxyl and hydroxyl modified SWCNTs toward SO_2. The results revealed that COOH-SWCNT exhibited a higher sensitivity due to its higher oxidizability which promotes the charge transfer between the SO_2 molecules and the CNT [49].

Graphene oxide

Another carbon material that has recently sparked interest in gas adsorption is graphene oxide. It is mainly synthesized by the modified Hummers method [50] from graphite and possesses higher surface area, good porosity, and multiple oxygen functional groups [50,51]. The most accepted model to represent GO structure is the Lerf-Klinowski model where the surface is decorated with epoxy, hydroxyl, carbonyl, and carboxylic groups at the edges [50]. The GO layers are held together by hydrogen bonds and the oxygen functional group is covalently bonded to the carbon atoms creating sp^3 hybridized carbon atoms [52]. Their 2D structure provides a high surface area to volume ratio which increases their reaction rate [53]. GO was successfully used in electronic devices as sensors [50,54] for energy and gas storage [50,51], as catalyst support for metal oxide nanoparticles [55].

For SO_2 removal, only a few studies have investigated the adsorption capacity of GO toward SO_2. Babu et al. demonstrated that the adsorption of pure SO_2 on GO is done by physisorption even in the presence of a significant amount of oxygen functionalities on the surface [51]. On the

other hand, Long et al. showed that upon adsorption of SO_2 by foams GO or GO suspensions at room temperature, the material acts as an oxidant and a catalyst to form SO_3. The presence of oxygen increases the production of SO_3 and in contact with water, sulfuric acid is formed [56]. Zhanga et al. studied the mechanism of adsorption and the oxidation of SO_2 on GO surface through Density Functional Theory (DFT) calculations [57]. GO was found to adsorb SO_2 through H-bonding interactions between its hydroxyl groups and SO_2. These hydroxyl groups also promote the oxidation of SO_2 by the epoxy groups by reducing the oxidation barrier [57].

In contrast to activated carbon and CNTs, there have been relatively fewer studies exploring the impact of adding metal nanoparticles to graphene oxide on its capacity to capture SO_2.

1.3. Organic Sulfide compounds removal

Sulfur pollutants in fuel streams lead to the emission of SO_2 when these fuels are burned, whether in transportation or oil refinery processes [1,58]. Additionally, sulfide-containing wastewater such as hydrogen sulfide, mercaptans, and dimethyl sulfide are responsible for the unpleasant odor in sewers or near wastewater treatment facilities [59–61]. Therefore it is crucial to desulfurize fuels and wastewater to mitigate pollution.

Hydrodesulfurization (HDS) is the most common method for reducing or eliminating sulfur from crude oil [58]. Hydrogen is used with catalysts to decompose sulfur compounds into hydrogen sulfide and hydrocarbons which are further used for sulfuric acid production and as refinery fuel gas respectively [62]. However, HDS is an expensive method due to its requirement for high hydrogen pressure (12-130 atm) and elevated temperatures (300-400°C) [5,58,63]. It requires high capital costs to build thick wall reactors capable of withstanding high-pressure conditions [58]. Additionally, compounds with more substitute rings such as benzothiophene are more difficult to decompose due to the strong steric hindrance [58]. Alternatively, catalytic oxidative desulfurization (ODS) is a cost-effective method as it can operate under relatively mild conditions (typically below 100°C and at atmospheric pressure)[5,58,64,65]. Sulfur compounds are initially oxidized to their corresponding sulfoxides or sulfones, which are then separated from fuel through extraction and adsorption techniques [66]. Sulfones have higher polarity which increases their solubility in polar solutions such as methanol, and acetonitrile [66].

For wastewater desulfurization, biological technologies are preferred for treating waste streams with low to medium sulfide concentrations [67]. These methods use microorganisms to convert sulfur compounds into sulfate, offering advantages such as operation at ambient temperatures, no need for catalysts, and reduced production of contaminated byproduct streams [67,68]. However, some sulfide compounds, like dimethyl sulfoxide (DMSO), are resistant to biodegradation and can be reduced to harmful volatile compounds like methyl mercaptan, dimethyl sulfide, and hydrogen sulfide [69,70]. To address this, oxidizing DMSO to produce dimethyl sulfone—a biodegradable compound—can prevent the formation of these noxious byproducts [70]. Combining oxidation with biological processes could therefore provide a practical solution for managing DMSO-containing wastewater [70,71].

In the last years, selective oxidation of sulfur-containing compounds (sulfides, sulfoxides, or thiophenes) has been studied for fuel desulfurization or wastewater treatments [5]. Various oxidants such as hydrogen peroxide (H_2O_2), oxygen, ozone [4,72] have been used, with H_2O_2 being the most commonly used oxidizing agent [5,72,73]. Its widespread use arises from its high chemical reactivity, wide availability, and the production of water as a by-product, making it environmentally friendly. Additionally, H_2O_2 has a good oxidation potential, is low cost, and is considered safe to use and store [73,74]. While H_2O_2 can oxidize sulfide to sulfoxide and sulfone without any activators, this typically requires longer reaction times [72,73]. To enhance the effectiveness of the oxidation process, H_2O_2 can be used with carboxylic acids such as formic acid, and acetic acid to form organic peracids which are highly reactive. However, these organic oxidants are also highly corrosive and pose problems in maintaining and recovering equipment [5,58]. An alternative approach involves using heterogeneous catalysts given their potential to be recovered and reused in further cycles [58,73,75].

Carbon-based materials have proven effective as catalyst supports in sulfide oxidation for removing thiophene compounds from fuel. Their high surface area allows for excellent dispersion of catalytic active phases. Abdelrahman et al. [76] and Huang et al. [77] achieved over 90% conversion of dibenzothiophene and benzothiophene, respectively, using nitrogen-doped onion-like carbon (NOLC) supported phosphotungstic acid and graphene oxide-supported keplerate nanoball iso-polyoxomolybdate (Mo132). They attributed these results to the high dispersion of the active phase and increased adsorption of sulfur compounds. However, Hou et al. [78] reported that increasing the amount of molybdenum dioxide (MoO_2) on graphite carbon nitride (g-C_3N_4)

reduces the catalyst's surface area, leading to poor dispersion of active sites. Thus, an optimal balance between active phase loading and maintaining a high surface area is crucial.

Surface functional groups also contribute significantly to desulfurization performance. Abdelrahman et al. found that graphene oxide (GO) enhances sulfur compound adsorption due to the Lewis acidic nature of its defect sites, which brings sulfur compounds and the oxidant closer, improving the oxidation reaction [76]. Furthermore, Haw et al. showed that acidic groups, especially oxygenated groups on activated carbon, enhance desulfurization performance through acid-base interactions between the carbon surface and sulfur molecules [79]. Gu et al. identified carbonyl groups as the primary oxygen groups responsible for increasing the catalytic activity of oxidized carbon nanotubes (CNTs) [80].

Furthermore, carbon-based materials can generate oxidizing species like hydroxyl radicals (OH·) from hydrogen peroxide [65,81,82]. After fluorine (3.03 eV), OH· possesses the highest reduction potential of 2.8 V, surpassing that of superoxide (2.42 eV), ozone (2.07 eV), and hydrogen peroxide (1.77 V) [74]. Additionally, OH· is highly reactive, nonselective, and capable of oxidizing and decomposing numerous hazardous compounds [74,83]. The catalytic activity of carbon materials in hydrogen peroxide decomposition was found to be governed by their electron donor capability, which is associated with the presence of delocalized π-electrons in the surface-conjugated system [81,82]. The reaction of the carbon material surface with H_2O_2 will result in an oxidized carbon surface with increased sp^3 carbon hybridization [81,82]. Studies have shown that the catalytic generation of OH· by GO is further enhanced by the addition of iron oxide through the Fenton process [84,85]. The Fenton process produces OH· through the oxidation of ferrous ions, as shown in the following equation [85]:

$$Fe^{2+} + H_2O_2 \rightarrow Fe^{3+} + OH^- + OH \cdot \quad (1.1)$$

When used as a support, GO has been shown to participate in the regeneration of Fe^{2+} by donating its electrons [85,86]. The produced OH· radicals were shown to effectively oxidize sulfide compounds in their corresponding sulfone for oxidative desulfurization treatment and DMSO removal from wastewater [64,87].

1.4. Graphene oxide-iron oxide nanocomposites

Graphene oxide-metal nanocomposites have been widely used as adsorbents for heavy metals removal in wastewater [88,89] and as heterogeneous catalysts in multiple organic reactions such as oxidation, reduction, or cross-coupling reactions [90,91]. Rodríguez-García et al, conducted research on the application of GO-iron oxide nanocomposites in gaseous CO_2 capture technologies, revealing higher adsorption of CO_2 compared to GO alone [92]. The addition of Fe_3O_4 nanoparticles was found to expand the GO layers thereby creating porosity which increases the CO_2 adsorption. Their findings demonstrated that the adsorption of CO_2 is a reversible physisorption mechanism and the material exhibits good CO_2/N_2 selectivity, recyclability, and thermal stability. Taking into account these findings and the improved efficiency of SO_2 removal achieved through the addition of oxygen functional groups or metal oxides on carbon nanotubes and activated carbon, it is conceivable that metal oxide-modified graphene oxide might be a suitable adsorbent for SO_2 removal. Moreover, such materials could be applied for sulfide oxidation [64,85,86,93].

Iron oxide nanoparticles are extensively used as catalysts due to their affordability, low toxicity, and excellent dispersibility [94,95]. The catalytic properties of these nanoparticles are significantly influenced by their shape, size, dispersity, and chemical composition [91,94]. These characteristics can be controlled through various synthesis methods including precipitation, hydrothermal, impregnation, polyol [94].

1.4.1. Precipitation/co-precipitation

The precipitation method is the most used approach for synthesizing metal-based nanoparticle catalysts on an industrial scale, owing to its cost-effectiveness and high yield [96,97]. This process typically involves precursors, a reducing agent, and a stabilizing agent or capping agent [96,98]. The synthesis is an oxidation-reduction reaction between the precursors and organic or inorganic reducing agents [96]. Precipitation synthesis occurs in three steps namely, supersaturation, nucleation, and growth [98]. The supersaturation can be achieved by adding a base, acid, or complex-forming agents, through physical changes such as temperature variation or a combination of these methods[98]. The system is unstable at the supersaturation stage and precipitation can occur as a result of any small perturbations[98]. Solid formation occurs through nucleation and growth. In conditions of high supersaturation, the nucleation rate can be higher than the crystal

growth leading to the formation of numerous small particles [98]. During precipitation, salts may be hydrolyzed into their hydroxide or oxide forms [99]. The resulting colloidal suspension is then filtered and dried and a calcination step may be required to convert the hydroxide compounds into oxides [99] Metal hydroxides and carbonates are the preferred precipitate intermediates due to their low solubility, which easily leads to very high supersaturation and results in small particle sizes. These compounds are also easily decomposed by heat into oxide and the toxicity and environmental impact resulting from calcination are minimal [98,100].

Co-precipitation involves the simultaneous precipitation of more than one compound from a solution [101]. It is important to avoid independent or consecutive precipitation to ensure intimate mixing of the catalyst components [100]. Iron oxide nanoparticles are typically produced by simultaneous precipitation of ferrous and ferric ions, initiated by the addition of a base, generally NaOH or NH_3H_2O at room or elevated temperature [102–105]. The reaction mechanism occurs as below [106]:

$$Fe^{2+} + 2Fe^{3+} + OH^- \rightarrow Fe_3O_4 \downarrow + 4H_2O \quad (1.2)$$

The resulting magnetite nanoparticles are unstable and can easily oxidize to form ferric nanoparticles (Fe_2O_3) [103,106]. Stabilizing agents or surfactants are used to control nanoparticle size and stabilize the colloidal dispersions [53]. Surfactants such as oleic acid [107], citric acid [108] polyvinyl alcohol [109], and glucose [110] have been used to improve the dispersity of iron oxide nanoparticles. Various parameters, including the type and concentration of precursors, the temperature, the mixing sequence, and the pH level influence the properties of the nanoparticles such as particle size, purity, surface area, and chemical composition [98,100,111]. Despite these controls, the method's inherent rapid particle formation limits its ability to produce uniform and monodispersed nanoparticles [103,106,112].

Precipitation or co-precipitation methods can be used to obtain supported catalysts, where the precursors are directly precipitated on the support [100]. However, this method is favored when the desired loading is higher than 10-20% [100].

1.4.2. Impregnation

The impregnation method is commonly employed for synthesizing supported catalysts with lower-weight nanoparticle deposition [100]. A specific volume of the solution containing the

active phase precursor is brought into contact with the solid support, followed by drying to eliminate the imbibed solvent. Subsequently, the catalyst is activated by calcination or reduction [99,100]. Preferably, pre-shaped supports are used because their texture is maintained in the final catalyst [98]. Impregnation can be carried out using an excess of solution (wet impregnation) or with a volume slightly less than or equal to the pore volume of the support (in incipient wetness impregnation) [100,113]. The latter demands precise reaction control and additional applications of the solution may be necessary [98]. In both techniques, temperature is a key factor as it influences the precursor solubility and the solution viscosity, thereby affecting the wetting time [100]. It's a simple technique with a limited amount of waste but requires materials that can withstand high temperatures as calcination temperatures [99,113].

1.4.3. Polyol

Polyol synthesis refers to the use of polyols to reduce metal salts to metal particles [114]. In a polyol synthesis, a metal precursor is mixed in a liquid polyol such as ethylene glycol, diethylene glycol, or tetra-ethylene glycol, and heated to a specific temperature, potentially reaching the polyol's point [106]. This process allows the polyol to be oxidized, enabling the reduction of metal precursors [115]. Here, the polyol acts as both a solvent and reducing agent, while also serving as a stabilizer to control nanoparticle growth and prevent agglomeration [106,116–118]. Various factors influence the type of nanoparticles obtained and the reagents must be chosen carefully.

A typical synthesis of iron oxide nanoparticles using the polyol method involves the reduction of iron (III) acetylacetonate ($Fe(acac)_3$) in a polyol solvent [114,119]. In a study conducted by Cai et al, tri-ethylene glycol was found to produce non-agglomerated magnetite particles with uniform shape and narrow size distribution [114]. However, polyols such as diethylene glycol and tetra-ethylene glycol resulted in unstable particle suspension in water or ethanol and highly agglomerate nanoparticles, respectively [114]. The reaction with ethylene glycol mainly produced the intermediate alkoxy-salt [114,120]. The choice of polyol solvent plays an important role in defining the morphology and colloidal stability of the nanoparticles.

Vega-Chacón et al. studied the effects of both the type and concentration of the ferric precursor on the average particle size of magnetite nanoparticles using a tri-ethylene glycol polyol solution [119]. The results indicated that a higher concentration of Fe^{3+} leads to larger particles, and

$Fe(acac)_3$ precursors produced larger nanoparticles than iron (III) nitrate nonahydrate ($Fe(NO_3)_3.9H_2O$), which is a cheaper and less toxic precursor.

In the study conducted by Christopher Panaritis et al., ethylene glycol containing tetramethylammonium hydroxide (TMAOH) was used to control nanoparticle size, and a mixture of 5 nm iron oxide nanowire composed of Fe_2O_3, Fe_3O_4, and FeO from $Fe(NO_3)_3.9H_2O$ iron salts was obtained. [121]. Christina Bock et al. explained that the addition of a base solution in polyol synthesis reduces nanoparticle size [117]. They explained that the aldehydes generated from ethylene glycol oxidation are unstable and easily oxidized to glycolic acid, which in an alkaline media, is presented in its deprotonated form as glycolate anion. This anion was identified as a stabilizing agent in the formation of PtRu alloy [117].

The polyol method is highly effective for producing iron oxide nanoparticles of various shapes and sizes. These nanoparticles, synthesized using the polyol method, are easily dispersed in aqueous media and polar solvents due to their hydrophilic surface ligands. They also exhibit high crystallinity because of the relatively high synthesis temperatures [106]. However, the method's sensitivity to reaction temperature, duration, and choice of precursors complicates the reproducibility of the method [122].

1.4.4. Hydrothermal method

In the hydrothermal method, the reaction takes place in an aqueous media, in a sealed vessel or autoclave, under high pressures (up to 2000 psi) and high temperatures ranging from 100°C to 250°C [123,124]. The solvent is usually water, with a hydroxide solution such as NaOH used as a mineralizer, and metal alkoxides or metal salts provide the metal ions [124]. The method exploits the water's ability to hydrolyze and dehydrate metal salts under elevated conditions, along with the very low solubility of the resulting metal oxide in water at these conditions to generate supersaturation [125]. The mineralizer functions as a catalyst to accelerate the reaction or as a solvent that dissolves and facilitates the precipitation of solid materials [126]. Similar to co-precipitation, the supersaturation state is followed by nucleation and particle growth [124]. The solvent, temperature, and duration of the reaction are important parameters influencing the size and morphology of the Fe_3O_4 nanoparticles [116,125]. At high temperatures, nucleation occurs more rapidly than grain growth, resulting in small nanoparticles. However, a longer reaction time will increase their size [116]. This method is also used for growing crystals of iron oxide

nanoparticles. In this case, the precipitation occurs at conditions similar to the co-precipitation method, followed by hydrothermal treatment in an autoclave [98,100,127]. This process involves structural changes in the solid, such as increased crystals and particle size [100].

Hydrothermal synthesis is relatively less explored as a method for synthesizing iron oxide nanoparticles, although it allows the production of monodispersed particles with precise control over their shape and size in addition to their chemical homogeneity and good dispersibility [103,128]. However, it is worth noting that this method requires supercritical solvent conditions and uses expensive autoclaves [101].

1.5. Research question and objectives

Graphene oxide and iron oxide nanoparticles have individually exhibited promising results as SO_2 capture materials [51,56,129,130]. Moreover, Zhang et al. explained that the S-C covalent interaction of SO_3 with the GO surface is higher than that of SO_2 [57]. Building on this, an iron oxide-modified graphene oxide was previously synthesized and tested in our research group, revealing a significant enhancement in SO_2 capture efficiency with the addition of iron oxide particles on the surface of GO [31]. Additionally, GO and iron oxide nanoparticles have been effectively used as heterogeneous catalysts in the oxidation of various sulfide compounds [64,93]. Therefore, to significantly mitigate sulfur-based pollution, this study proposes a multifunctional composite material consisting of graphene oxide and iron oxide nanoparticles to enhance SO_2 gas removal through adsorption technology and to catalyze the oxidation of organic sulfide to sulfone, thus facilitating the removal of organic sulfide from fuels or wastewater.

From this objective, the following research questions arise: how does the type of iron oxide nanoparticles influence the capture capacity of the GO-iron oxide nanocomposite? Can the composite be used as a catalyst in the oxidation reaction of organic sulfide compounds and exhibit photocatalytic properties? The study addresses the following objectives:

- Investigate the impact of the different nanoparticle preparation methods on the structure of the synthesized GO-iron oxide material as well as its capture capacity for SO_2.
- Evaluate the regenerability of the adsorbent.
- Assess the catalytic performance of the GO-iron oxide nanocomposite in the organic sulfide oxidation process, highlighting thioanisole as the chosen sulfide compound.

1.6. Content of the thesis

The thesis consists of four chapters. Chapter 1 presented the project background, literature review, and research objectives. Chapter 2 explores the capture capacity of the GO-iron oxide material for SO_2 removal at room temperature, examining the effect of various nanoparticle synthesis methods. This chapter also includes the regeneration tests of the adsorbent at different temperatures (room temperature and 100°C). Chapter 3 looks at the catalytic properties of the GO-iron oxide material in the oxidation of thioanisole. The photocatalytic activity was also evaluated using different light irradiations such as UV, visible light, and sunlight. Finally, chapter 4 summarizes the report with key findings from the previous chapters and potential future work for the project.

References

1. Robinson, P.R. Sulfur Removal and Recovery. In *Springer Handbook of Petroleum Technology*; Hsu, C.S., Robinson, P.R., Eds.; Springer Handbooks; Springer International Publishing: Cham, 2017; pp. 649–673 ISBN 978-3-319-49347-3.
2. Sulfuric Acid - DCCEEW Available online: https://www.dcceew.gov.au/environment/protection/npi/substances/fact-sheets/sulfuric-acid (accessed on 6 May 2024).
3. Toxicology, N.R.C. (US) C. on SULFURIC ACID. In *Emergency and Continuous Exposure Limits for Selected Airborne Contaminants: Volume 1*; National Academies Press (US), 1984.
4. Ahmad, W. Sulfur in Petroleum: Petroleum Desulfurization Techniques. In *Applying Nanotechnology to the Desulfurization Process in Petroleum Engineering*; 2016; pp. 1–52 ISBN 978-1-4666-9545-0.
5. Hulea, V.; Dumitriu, E.; Fajula, F. Mild Oxidation of Organosulfur Compounds with H2O2 over Metal-Containing Microporous and Mesoporous Catalysts. *Catalysts* **2021**, *11*, 867, doi:10.3390/catal11070867.
6. Ben Hariz, I.; Al Ayni, F.; Monser, L. Removal of Sulfur Compounds from Petroleum Refinery Wastewater through Adsorption on Modified Activated Carbon. *Water Sci Technol* **2014**, *70*, 1376–1382, doi:10.2166/wst.2014.384.
7. Habibi, M.H.; Vosooghian, H. Photocatalytic Degradation of Some Organic Sulfides as Environmental Pollutants Using Titanium Dioxide Suspension. *Journal of Photochemistry and Photobiology A: Chemistry* **2005**, *174*, 45–52, doi:10.1016/j.jphotochem.2005.02.012.
8. Khalaf, E.M.; Mohammadi, M.J.; Sulistiyani, S.; Ramírez-Coronel, A.A.; Kiani, F.; Jalil, A.T.; Almulla, A.F.; Asban, P.; Farhadi, M.; Derikondi, M. Effects of Sulfur Dioxide Inhalation on Human Health: A Review. *Reviews on Environmental Health* **2022**, doi:10.1515/reveh-2022-0237.
9. A. Tewari; N. P. Shukla Air Pollution - Adverse Effects of Sulfur Dioxide. *Reviews on Environmental Health* **1991**, *9*, 39–46, doi:10.1515/REVEH.1991.9.1.39.
10. Effects of Acid Rain Available online: https://www.epa.gov/acidrain/effects-acid-rain.
11. National Pollutant Release Inventory: Sulphur Dioxide Available online: https://www.canada.ca/en/environment-climate-change/services/national-pollutant-release-inventory/tools-resources-data/sulphur-dioxide.html (accessed on 12 February 2024).
12. Canada's Air Pollutant Emissions Inventory Report 2023: Chapter 2.2 (accessed on 25 September 2023).
13. Hanif, M.A.; Ibrahim, N.; Abdul Jalil, A. Sulfur Dioxide Removal: An Overview of Regenerative Flue Gas Desulfurization and Factors Affecting Desulfurization Capacity and Sorbent Regeneration. *Environ Sci Pollut Res* **2020**, *27*, 27515–27540, doi:10.1007/s11356-020-09191-4.
14. Mathieu, Y.; Tzanis, L.; Soulard, M.; Patarin, J.; Vierling, M.; Molière, M. Adsorption of SOx by Oxide Materials: A Review. *Fuel Processing Technology* **2013**, *114*, 81–100, doi:10.1016/j.fuproc.2013.03.019.
15. Carpenter, A.M. Low Water FGD Technologies Available online: https://usea.org/publication/low-water-fgd-technologies-ccc210 (accessed on 5 February 2024).

16. Cheremisinoff, N.P. 2 - Solid Wastes. In *Clean Electricity Through Advanced Coal Technologies*; Cheremisinoff, N.P., Ed.; William Andrew Publishing: Oxford, 2012; pp. 31–61 ISBN 978-1-4377-7815-1.
17. Poullikkas, A. Review of Design, Operating, and Financial Considerations in Flue Gas Desulfurization Systems. *Energy Technology & Policy* **2015**, *2*, 92–103, doi:10.1080/23317000.2015.1064794.
18. Flagiello, D.; Erto, A.; Lancia, A.; Di Natale, F. Experimental and Modelling Analysis of Seawater Scrubbers for Sulphur Dioxide Removal from Flue-Gas. *Fuel* **2018**, *214*, 254–263, doi:10.1016/j.fuel.2017.10.098.
19. Srivastava, R.K. CONTROLLING SO2 EMISSIONS: A REVIEW OF TECHNOLOGIES (EPA/600/R-00/093) (accessed on 6 February 2024).
20. Air Pollution Control Technology Fact Sheet (accessed on 6 February 2024).
21. Gutiérrez Ortiz, F.J.; Vidal, F.; Ollero, P.; Salvador, L.; Cortés, V.; Giménez, A. Pilot-Plant Technical Assessment of Wet Flue Gas Desulfurization Using Limestone. *Ind. Eng. Chem. Res.* **2006**, *45*, 1466–1477, doi:10.1021/ie051316o.
22. Yu, X.; Hao, J.; Xi, Z.; Liu, T.; Lin, Y.; Xu, B. Investigation of Low Concentration SO2 Adsorption Performance on Different Amine-Modified Merrifield Resins. *Atmospheric Pollution Research* **2019**, *10*, 404–411, doi:10.1016/j.apr.2018.08.015.
23. Sargent & Lundy LLC *Flue Gas Desulfurization Technology Evaluation. Dry Lime vs Wet Limestone FGD*; Sargent & Lundy LLC: 55 East Monroe Street Chicago, IL 60603-5780 USA, 2007; p. 64;.
24. Rezaei, F.; Rownaghi, A.A.; Monjezi, S.; Lively, R.P.; Jones, C.W. SOx/NOx Removal from Flue Gas Streams by Solid Adsorbents: A Review of Current Challenges and Future Directions. *Energy Fuels* **2015**, *29*, 5467–5486, doi:10.1021/acs.energyfuels.5b01286.
25. Savage, M.; Cheng, Y.; Easun, T.L.; Eyley, J.E.; Argent, S.P.; Warren, M.R.; Lewis, W.; Murray, C.; Tang, C.C.; Frogley, M.D.; et al. Selective Adsorption of Sulfur Dioxide in a Robust Metal–Organic Framework Material. *Advanced Materials* **2016**, *28*, 8705–8711, doi:10.1002/adma.201602338.
26. Liu, X.-L.; Guo, J.-X.; Chu, Y.-H.; Luo, D.-M.; Yin, H.-Q.; Sun, M.-C.; Yavuz, R. Desulfurization Performance of Iron Supported on Activated Carbon. *Fuel* **2014**, *123*, 93–100, doi:10.1016/j.fuel.2014.01.068.
27. Davini, P. The Effect of Certain Metallic Derivatives on the Adsorption of Sulphur Dioxide on Active Carbon. *Carbon* **2001**, *39*, 419–424, doi:10.1016/S0008-6223(00)00134-2.
28. An, L.; Jia, X.; Liu, Y. Adsorption of SO_2 Molecules on Fe-Doped Carbon Nanotubes: The First Principles Study. *Adsorption* **2019**, *25*, 217–224, doi:10.1007/s10450-019-00026-4.
29. Li, W.; Ma, J.-J.; Liu, P.; Pan, Z.-L.; He, Q.-Y. First-Principles Study of the Adsorption Sensitivity of Ni-Doped Single-Walled Zigzag (n,0)CNTs (N=4,5,6) toward SO2 Molecules. *Applied Surface Science* **2015**, *335*, 17–22, doi:10.1016/j.apsusc.2015.01.181.
30. Babu, D.J.; Puthusseri, D.; Kühl, F.G.; Okeil, S.; Bruns, M.; Hampe, M.; Schneider, J.J. SO2 Gas Adsorption on Carbon Nanomaterials: A Comparative Study. *Beilstein J Nanotechnol* **2018**, *9*, 1782–1792, doi:10.3762/bjnano.9.169.
31. Sanyal, T.S.; Mugisha, A.I.; Sowinski, A.; Fauteux-Lefebvre, C. Enhancement of Sulfur Oxide Capture Capacity by Deposition of Iron Oxide Particles on Graphene Oxide. *Catalysts* **2023**, *13*, 1469, doi:10.3390/catal13121469.

32. Pradhan, B.K.; Sandle, N.K. Effect of Different Oxidizing Agent Treatments on the Surface Properties of Activated Carbons. *Carbon* **1999**, *37*, 1323–1332, doi:10.1016/S0008-6223(98)00328-5.
33. Raymundo-Piñero, E.; Cazorla-Amorós, D.; Salinas-Martinez de Lecea, C.; Linares-Solano, A. Factors Controling the SO2 Removal by Porous Carbons: Relevance of the SO2 Oxidation Step. *Carbon* **2000**, *38*, 335–344, doi:10.1016/S0008-6223(99)00109-8.
34. Ahnert, F.; Heschel, W. Multicomponent Adsorption of Butane, NO2 and SO2 on Activated Carbon. *Adsorption Science & Technology* **2002**, *20*, 353–370, doi:10.1260/02636170260295542.
35. Daley, M.A.; Mangun, C.L.; DeBarrb, J.A.; Riha, S.; Lizzio, A.A.; Donnals, G.L.; Economy, J. Adsorption of SO2 onto Oxidized and Heat-Treated Activated Carbon Fibers (ACFs). *Carbon* **1997**, *35*, 411–417, doi:10.1016/S0008-6223(97)89612-1.
36. Zhao, X.S.; Cai, G.Y.; Wang, Z.Z.; Wang, Q.X.; Yang, Y.H.; Luo, J.S. Influences of Surface Functional Groups on Catalytic Activity over Activated Carbon Catalysts for Sulfur Dioxide Removal from Flue Gases. *Applied Catalysis B: Environmental* **1994**, *3*, 229–238, doi:10.1016/0926-3373(94)00002-6.
37. Guo, J.; Liang, J.; Chu, Y.-H.; Sun, M.-C.; Yin, H.-Q.; Li, J.-J. Desulfurization Activity of Nickel Supported on Acid-Treated Activated Carbons. *Applied Catalysis A: General* **2012**, *421–422*, 142–147, doi:10.1016/j.apcata.2012.02.010.
38. Carrasco-Marin, F.; Utrera-Hidalgo, E.; Rivera-Utrilla, J.; Moreno-Castilla, C. Adsorption of SO2 in Flowing Air onto Activated Carbons from Olive Stones. *Fuel* **1992**, *71*, 575–578, doi:10.1016/0016-2361(92)90156-I.
39. Dynamic Adsorption on Activated Carbons of SO2 Traces in Air: I. Adsorption Capacities. *Carbon* **2002**, *40*, 2235–2246, doi:10.1016/S0008-6223(02)00108-2.
40. Nazal, M.K. An Overview of Carbon-Based Materials for the Removal of Pharmaceutical Active Compounds. In *Carbon-Based Material for Environmental Protection and Remediation*; IntechOpen, 2020 ISBN 978-1-78984-587-7.
41. Ren, X.; Chen, C.; Nagatsu, M.; Wang, X. Carbon Nanotubes as Adsorbents in Environmental Pollution Management: A Review. *Chemical Engineering Journal* **2011**, *170*, 395–410, doi:10.1016/j.cej.2010.08.045.
42. Hu, Z.; Xie, H.; Wang, Q.; Chen, S. Adsorption and Diffusion of Sulfur Dioxide and Nitrogen in Single-Wall Carbon Nanotubes. *Journal of Molecular Graphics and Modelling* **2019**, *88*, 62–70, doi:10.1016/j.jmgm.2019.01.003.
43. Zhang, X.; Cui, H.; Gui, Y.; Tang, J. Mechanism and Application of Carbon Nanotube Sensors in SF6 Decomposed Production Detection: A Review. *Nanoscale Res Lett* **2017**, *12*, 177, doi:10.1186/s11671-017-1945-8.
44. Sun, F.; Gao, J.; Zhu, Y.; Chen, G.; Wu, S.; Qin, Y. Adsorption of SO2 by Typical Carbonaceous Material: A Comparative Study of Carbon Nanotubes and Activated Carbons. *Adsorption* **2013**, *19*, 959–966, doi:10.1007/s10450-013-9504-9.
45. Lu, X.; Sun, C.; Li, F.; Cheng, H.-M. Selected Absorption Behavior of Sulfur on Single-Walled Carbon Nanotubes by DFT. *Chemical Physics Letters* **2008**, *454*, 305–309, doi:10.1016/j.cplett.2008.02.027.
46. Iraji, N.; Hojjat, M.; Aghamiri, S.; Talaie, M.R.; Molyanyan, E. Adsorption of CO2 and SO2 on Multi-Walled Carbon Nanotubes: Experimental Data and Modeling Using Artificial Neural Network. *Journal of Particle Science and Technology* **2019**, *5*, 33–45, doi:10.22104/jpst.2019.3317.1140.

47. Yoosefian, M.; Zahedi, M.; Mola, A.; Naserian, S. A DFT Comparative Study of Single and Double SO2 Adsorption on Pt-Doped and Au-Doped Single-Walled Carbon Nanotube. *Applied Surface Science* **2015**, *349*, 864–869, doi:10.1016/j.apsusc.2015.05.088.
48. Zhang, X.; Meng, F.; Yang, B. Use of Hydroxyl-Modified Carbon Nanotubes for Detecting SF6 Decomposition Products under Partial Discharge in Gas Insulated Switchgear. *IEEE Transactions on Dielectrics and Electrical Insulation* **2013**, *20*, 2246–2253, doi:10.1109/TDEI.2013.6678876.
49. Zhang, X.; Yang, B.; Dai, Z.; Luo, C. The Gas Response of Hydroxyl Modified SWCNTs and Carboxyl Modified SWCNTs to H2S and SO2. *Przegląd Elektrotechniczny* **2012**, 311–314.
50. Dreyer, D.R.; Park, S.; Bielawski, C.W.; Ruoff, R.S. The Chemistry of Graphene Oxide. *Chem. Soc. Rev.* **2009**, *39*, 228–240, doi:10.1039/B917103G.
51. Babu, D.J.; Kühl, F.G.; Yadav, S.; Markert, D.; Bruns, M.; Hampe, M.J.; Schneider, J.J. Adsorption of Pure SO_2 on Nanoscaled Graphene Oxide. *RSC Adv.* **2016**, *6*, 36834–36839, doi:10.1039/C6RA07518E.
52. Hajian, R.; Fung, K.; Chou, P.P.; Wang, S.; Balderston, S.; Aran, K. Functionalized Graphene Oxide: Properties & Applications Available online: https://www.sigmaaldrich.com/CA/en/technical-documents/technical-article/materials-science-and-engineering/batteries-supercapacitors-and-fuel-cells/functionalized-graphene-oxide (accessed on 19 July 2024).
53. Shanmugam, V.; Mensah, R.A.; Babu, K.; Gawusu, S.; Chanda, A.; Tu, Y.; Neisiany, R.E.; Försth, M.; Sas, G.; Das, O. A Review of the Synthesis, Properties, and Applications of 2D Materials. *Particle & Particle Systems Characterization* **2022**, *39*, 2200031, doi:10.1002/ppsc.202200031.
54. Zhu, Y.; Murali, S.; Cai, W.; Li, X.; Suk, J.W.; Potts, J.R.; Ruoff, R.S. Graphene and Graphene Oxide: Synthesis, Properties, and Applications. *Advanced Materials* **2010**, *22*, 3906–3924, doi:10.1002/adma.201001068.
55. Sachdeva, H. Recent Advances in the Catalytic Applications of GO/rGO for Green Organic Synthesis. *Green Processing and Synthesis* **2020**, *9*, 515–537, doi:10.1515/gps-2020-0055.
56. Long, Y.; Zhang, C.; Wang, X.; Gao, J.; Wang, W.; Liu, Y. Oxidation of SO_2 to SO_3 Catalyzed by Graphene Oxide Foams. *J. Mater. Chem.* **2011**, *21*, 13934–13941, doi:10.1039/C1JM12031J.
57. Zhang, H.; Cen, W.; Liu, J.; Guo, J.; Yin, H.; Ning, P. Adsorption and Oxidation of SO2 by Graphene Oxides: A van Der Waals Density Functional Theory Study. *Applied Surface Science* **2015**, *324*, 61–67, doi:10.1016/j.apsusc.2014.10.087.
58. Betiha, M.A.; Rabie, A.M.; Ahmed, H.S.; Abdelrahman, A.A.; El-Shahat, M.F. Oxidative Desulfurization Using Graphene and Its Composites for Fuel Containing Thiophene and Its Derivatives: An Update Review. *Egyptian Journal of Petroleum* **2018**, *27*, 715–730, doi:10.1016/j.ejpe.2017.10.006.
59. Odor Control in Wastewater Treatment: The Removal of Thioanisole from WaterA Model Case Study by Pulse Radiolysis and Electron Beam Treatment Available online: https://pubs.acs.org/doi/epdf/10.1021/es990692v (accessed on 12 October 2023).
60. Federation, W.E. Liquid Stream Fundamentals: Odor Control. **2017**.
61. Talaiekhozani, A.; Bagheri, M.; Goli, A.; Talaei Khoozani, M.R. An Overview of Principles of Odor Production, Emission, and Control Methods in Wastewater Collection and

Treatment Systems. *Journal of Environmental Management* **2016**, *170*, 186–206, doi:10.1016/j.jenvman.2016.01.021.
62. Carruthers, J.E.; Solomon, L.H.; Waddams, A.L. Petroleum Refining Available online: https://www.britannica.com/technology/petroleum-refining.
63. Shiraishi, Y.; Hirai, T.; Komasawa, I. A Deep Desulfurization Process for Light Oil by Photochemical Reaction in an Organic Two-Phase Liquid−Liquid Extraction System. *Ind. Eng. Chem. Res.* **1998**, *37*, 203–211, doi:10.1021/ie970388f.
64. Flores, R.; Rodas, A.; Gasperin, R. Oxidative Desulfurization of Diesel Fuel Oil Using Supported Fenton Catalysts and Assisted with Ultrasonic Energy. *Pet. Sci.* **2019**, *16*, 1176–1184, doi:10.1007/s12182-019-0349-z.
65. Roman, F.F.; Diaz de Tuesta, J.L.; Silva, A.M.T.; Faria, J.L.; Gomes, H.T. Carbon-Based Materials for Oxidative Desulfurization and Denitrogenation of Fuels: A Review. *Catalysts* **2021**, *11*, 1239, doi:10.3390/catal11101239.
66. Campos-Martin, J. m.; Capel-Sanchez, M. c.; Perez-Presas, P.; Fierro, J. l. g. Oxidative Processes of Desulfurization of Liquid Fuels. *Journal of Chemical Technology & Biotechnology* **2010**, *85*, 879–890, doi:10.1002/jctb.2371.
67. Lin, S.; Mackey, H.R.; Hao, T.; Guo, G.; van Loosdrecht, M.C.M.; Chen, G. Biological Sulfur Oxidation in Wastewater Treatment: A Review of Emerging Opportunities. *Water Research* **2018**, *143*, 399–415, doi:10.1016/j.watres.2018.06.051.
68. Pudi, A.; Rezaei, M.; Signorini, V.; Andersson, M.P.; Baschetti, M.G.; Mansouri, S.S. Hydrogen Sulfide Capture and Removal Technologies: A Comprehensive Review of Recent Developments and Emerging Trends. *Separation and Purification Technology* **2022**, *298*, 121448, doi:10.1016/j.seppur.2022.121448.
69. Baldoni-Andrey, P.; Commarieu, A.; Plisson-Saune, S. Treatment of Wastewater Containing Dimethyl Sulfoxide (DMSO). In *Environmental Chemistry: Green Chemistry and Pollutants in Ecosystems*; Lichtfouse, E., Schwarzbauer, J., Robert, D., Eds.; Springer: Berlin, Heidelberg, 2005; pp. 615–620 ISBN 978-3-540-26531-3.
70. Cojocariu, A.M.; Mutin, P.H.; Dumitriu, E.; Vioux, A.; Fajula, F.; Hulea, V. Removal of Dimethylsulfoxide from Wastewater Using Mild Oxidation with H2O2 over Ti-Based Catalysts. *Chemosphere* **2009**, *77*, 1065–1068, doi:10.1016/j.chemosphere.2009.08.059.
71. Maciuca, A.-L.; Dumitriu, E.; Fajula, F.; Hulea, V. Catalytic Oxidation Processes for Removing Dimethylsulfoxide from Wastewater. *Chemosphere* **2007**, *68*, 227–233, doi:10.1016/j.chemosphere.2007.01.028.
72. Tumula, V.R.; Bondwal, S.; Bisht, P.; Pendem, C.; Kumar, J. Oxidation of Sulfides to Sulfones with Hydrogen Peroxide in the Presence of Acetic Acid and Amberlyst 15. *Reac Kinet Mech Cat* **2012**, *107*, 449–466, doi:10.1007/s11144-012-0491-8.
73. Kaczorowska, K.; Kolarska, Z.; Mitka, K.; Kowalski, P. Oxidation of Sulfides to Sulfoxides. Part 2: Oxidation by Hydrogen Peroxide. *Tetrahedron* **2005**, *61*, 8315–8327, doi:10.1016/j.tet.2005.05.044.
74. Kumari, P.; Kumar, A. ADVANCED OXIDATION PROCESS: A Remediation Technique for Organic and Non-Biodegradable Pollutant. *Results in Surfaces and Interfaces* **2023**, *11*, 100122, doi:10.1016/j.rsurfi.2023.100122.
75. Lima, N.A.; Alencar, L.D.D.S.; Mendonça, G.C.; Mesquita, A.; Silva, A.V.P.; Rosmaninho, M.G.; Taylor, J.G.; Fajardo, H.V.; Moraes, L.C.; Bernardi, M.I.B. *Heterogeneous Catalysis for Thioanisole Oxidation Using Hydrogen Peroxide and Copper, Nickel and Zinc Tungstates Prepared by the Polymeric Precursor Method*; In Review, 2020;

76. Abdelrahman, A.A.; Betiha, M.A.; Rabie, A.M.; Ahmed, H.S.; Elshahat, M.F. Removal of Refractory Organo-sulfur Compounds Using an Efficient and Recyclable {Mo132} Nanoball Supported Graphene Oxide. *Journal of Molecular Liquids* **2018**, *252*, 121–132, doi:10.1016/j.molliq.2017.12.124.
77. Huang, P.; Liu, A.; Kang, L.; Dai, B.; Zhu, M.; Zhang, J. Heteropolyacid Supported on Nitrogen-Doped Onion-Like Carbon as Catalyst for Oxidative Desulfurization. *ChemistrySelect* **2017**, *2*, 4010–4015, doi:10.1002/slct.201700226.
78. Hou, L.; Zhao, R.; Li, X.; Gao, X. Preparation of MoO2/g-C3N4 Composites with a High Surface Area and Its Application in Deep Desulfurization from Model Oil. *Applied Surface Science* **2018**, *434*, 1200–1209, doi:10.1016/j.apsusc.2017.10.076.
79. Haw, K.-G.; Bakar, W.A.W.A.; Ali, R.; Chong, J.-F.; Kadir, A.A.A. Catalytic Oxidative Desulfurization of Diesel Utilizing Hydrogen Peroxide and Functionalized-Activated Carbon in a Biphasic Diesel–Acetonitrile System. *Fuel Processing Technology* **2010**, *91*, 1105–1112, doi:10.1016/j.fuproc.2010.03.021.
80. Gu, Q.; Ding, Y.; Liu, Z.; Lin, Y.; Schlögl, R.; Heumann, S.; Su, D. Probing the Intrinsic Catalytic Activity of Carbon Nanotubes for the Metal-Free Oxidation of Aromatic Thiophene Compounds in Ionic Liquids. *Journal of Energy Chemistry* **2019**, *32*, 131–137, doi:10.1016/j.jechem.2018.07.004.
81. Voitko, K.; Tóth, A.; Demianenko, E.; Dobos, G.; Berke, B.; Bakalinska, O.; Grebenyuk, A.; Tombácz, E.; Kuts, V.; Tarasenko, Y.; et al. Catalytic Performance of Carbon Nanotubes in H2O2 Decomposition: Experimental and Quantum Chemical Study. *Journal of Colloid and Interface Science* **2015**, *437*, 283–290, doi:10.1016/j.jcis.2014.09.045.
82. Nguyen, L.V.; Busquets, R.; Ray, S.; Cundy, A.B. Graphene Oxide-Based Degradation of Metaldehyde: Effective Oxidation through a Modified Fenton's Process. *Chemical Engineering Journal* **2017**, *307*, 159–167, doi:10.1016/j.cej.2016.08.052.
83. WANG, J.L.; XU, L.J. Advanced Oxidation Processes for Wastewater Treatment: Formation of Hydroxyl Radical and Application. *Critical Reviews in Environmental Science and Technology* **2012**, *42*, 251–325, doi:10.1080/10643389.2010.507698.
84. Thomas, N.; Dionysiou, D.D.; Pillai, S.C. Heterogeneous Fenton Catalysts: A Review of Recent Advances. *J Hazard Mater* **2021**, *404*, 124082, doi:10.1016/j.jhazmat.2020.124082.
85. Nidheesh, P.V. Graphene-Based Materials Supported Advanced Oxidation Processes for Water and Wastewater Treatment: A Review. *Environ Sci Pollut Res* **2017**, *24*, 27047–27069, doi:10.1007/s11356-017-0481-5.
86. Zubir, N.A.; Yacou, C.; Motuzas, J.; Zhang, X.; Zhao, X.S.; Costa, J.C.D. da The Sacrificial Role of Graphene Oxide in Stabilising a Fenton-like Catalyst GO–Fe3O4. *Chem. Commun.* **2015**, *51*, 9291–9293, doi:10.1039/C5CC02292D.
87. Bellotindos, L.M.; Lu, M.; Methatham, T.; Lu, M. Factors Affecting Degradation of Dimethyl Sulfoxide (DMSO) by Fluidized-Bed Fenton Process. *Environmental Science and Pollution Research* **2014**, *21*, 14158–14165, doi:10.1007/s11356-014-3320-y.
88. Su, H.; Ye, Z.; Hmidi, N. High-Performance Iron Oxide-Graphene Oxide Nanocomposite Adsorbents for Arsenic Removal. *Colloids and Surfaces A: Physicochemical and Engineering Aspects* **2017**, *522*, doi:10.1016/j.colsurfa.2017.02.065.
89. Rodríguez, C.; Tapia, C.; Leiva-Aravena, E.; Leiva, E. Graphene Oxide–ZnO Nanocomposites for Removal of Aluminum and Copper Ions from Acid Mine Drainage Wastewater. *Int J Environ Res Public Health* **2020**, *17*, 6911, doi:10.3390/ijerph17186911.

90. Shabestari, M.E.; Martín, O.; Díaz-García, D.; Gómez-Ruiz, S.; Gonzalez, V.J.; Baselga, J. Facile and Rapid Decoration of Graphene Oxide with Copper Double Salt, Oxides and Metallic Copper as Catalysts in Oxidation and Coupling Reactions. *Carbon* **2020**, *161*, 7–16, doi:10.1016/j.carbon.2020.01.015.
91. Soni, J.; Sethiya, A.; Sahiba, N.; Agarwal, S. Recent Advancements in Organic Synthesis Catalyzed by Graphene Oxide Metal Composites as Heterogeneous Nanocatalysts. *Applied Organometallic Chemistry* **2021**, *35*, e6162, doi:10.1002/aoc.6162.
92. Rodríguez-García, S.; Santiago, R.; López-Díaz, D.; Merchán, M.D.; Velázquez, M.M.; Fierro, J.L.G.; Palomar, J. Role of the Structure of Graphene Oxide Sheets on the CO2 Adsorption Properties of Nanocomposites Based on Graphene Oxide and Polyaniline or Fe3O4-Nanoparticles. *ACS Sustainable Chem. Eng.* **2019**, *7*, 12464–12473, doi:10.1021/acssuschemeng.9b02035.
93. Zhou, X.; Wang, T.; Liu, H.; Gao, X.; Wang, C.; Wang, G. Desulfurization through Photocatalytic Oxidation: A Critical Review. *ChemSusChem* **2021**, *14*, 492–511, doi:10.1002/cssc.202002144.
94. Ali, A.; Zafar, H.; Zia, M.; Haq, I. ul; Phull, A.R.; Ali, J.S.; Hussain, A. Synthesis, Characterization, Applications, and Challenges of Iron Oxide Nanoparticles. *NSA* **2016**, *9*, 49–67, doi:10.2147/NSA.S99986.
95. Akbari, A.; Amini, M.; Tarassoli, A.; Eftekhari-Sis, B.; Ghasemian, N.; Jabbari, E. Transition Metal Oxide Nanoparticles as Efficient Catalysts in Oxidation Reactions. *Nano-Structures & Nano-Objects* **2018**, *14*, 19–48, doi:10.1016/j.nanoso.2018.01.006.
96. Shnoudeh, A.J.; Hamad, I.; Abdo, R.W.; Qadumii, L.; Jaber, A.Y.; Surchi, H.S. Chapter 15 - Synthesis, Characterization, and Applications of Metal Nanoparticles. In *Biomaterials and Bionanotechnology*; Academic Press, 2019; pp. 527–612 ISBN 978-0-12-814427-5.
97. Mazrouaa, A.M.; Mohamed, M.G.; Fekry, M. Physical and Magnetic Properties of Iron Oxide Nanoparticles with a Different Molar Ratio of Ferrous and Ferric. *Egyptian Journal of Petroleum* **2019**, *28*, 165–171, doi:10.1016/j.ejpe.2019.02.002.
98. Campanati, M.; Fornasari, G.; Vaccari, A. Fundamentals in the Preparation of Heterogeneous Catalysts. *Catalysis Today* **2003**, *77*, 299–314, doi:10.1016/S0920-5861(02)00375-9.
99. Deraz, N.M. The Comparative Jurisprudence of Catalysts Preparation Methods: I. Precipitation and Impregnation Methods. *Journal of Industrial and Environmental Chemistry* **2017**, *1*.
100. Perego, C.; Villa, P. Catalyst Preparation Methods. *Catalysis Today* **1997**, *34*, 281–305, doi:10.1016/S0920-5861(96)00055-7.
101. Srivastava, A.; Katiyar, A. 10 - Zinc Oxide Nanostructures. In *Ceramic Science and Engineering*; Misra, K.P., Misra, R.D.K., Eds.; Elsevier Series on Advanced Ceramic Materials; Elsevier, 2022; pp. 235–262 ISBN 978-0-323-89956-7.
102. Jamkhande, P.G.; Ghule, N.W.; Bamer, A.H.; Kalaskar, M.G. Metal Nanoparticles Synthesis: An Overview on Methods of Preparation, Advantages and Disadvantages, and Applications. *Journal of Drug Delivery Science and Technology* **2019**, *53*, 101174, doi:10.1016/j.jddst.2019.101174.
103. Lu, A.-H.; Salabas, E.L.; Schüth, F. Magnetic Nanoparticles: Synthesis, Protection, Functionalization, and Application. *Angewandte Chemie International Edition* **2007**, *46*, 1222–1244, doi:10.1002/anie.200602866.

104. Sun, S.; Zeng, H. Size-Controlled Synthesis of Magnetite Nanoparticles. *J. Am. Chem. Soc.* **2002**, *124*, 8204–8205, doi:10.1021/ja026501x.
105. Besenhard, M.O.; LaGrow, A.P.; Hodzic, A.; Kriechbaum, M.; Panariello, L.; Bais, G.; Loizou, K.; Damilos, S.; Margarida Cruz, M.; Thanh, N.T.K.; et al. Co-Precipitation Synthesis of Stable Iron Oxide Nanoparticles with NaOH: New Insights and Continuous Production via Flow Chemistry. *Chemical Engineering Journal* **2020**, *399*, 125740, doi:10.1016/j.cej.2020.125740.
106. Wu, W.; Wu, Z.; Yu, T.; Jiang, C.; Kim, W.-S. Recent Progress on Magnetic Iron Oxide Nanoparticles: Synthesis, Surface Functional Strategies and Biomedical Applications. *Science and Technology of Advanced Materials* **2015**, *16*, 023501, doi:10.1088/1468-6996/16/2/023501.
107. Willis, A.L.; Turro, N.J.; O'Brien, S. Spectroscopic Characterization of the Surface of Iron Oxide Nanocrystals. *Chem. Mater.* **2005**, *17*, 5970–5975, doi:10.1021/cm051370v.
108. Dheyab, M.A.; Aziz, A.A.; Jameel, M.S.; Noqta, O.A.; Khaniabadi, P.M.; Mehrdel, B. Simple Rapid Stabilization Method through Citric Acid Modification for Magnetite Nanoparticles. *Sci Rep* **2020**, *10*, 10793, doi:10.1038/s41598-020-67869-8.
109. Lee, J.; Isobe, T.; Senna, M. Magnetic Properties of Ultrafine Magnetite Particles and Their Slurries Prepared via In-Situ Precipitation. *Colloids and Surfaces A: Physicochemical and Engineering Aspects* **1996**, *109*, 121–127, doi:10.1016/0927-7757(95)03479-X.
110. Sun, X.; Zheng, C.; Zhang, F.; Yang, Y.; Wu, G.; Yu, A.; Guan, N. Size-Controlled Synthesis of Magnetite (Fe3O4) Nanoparticles Coated with Glucose and Gluconic Acid from a Single Fe(III) Precursor by a Sucrose Bifunctional Hydrothermal Method. *J. Phys. Chem. C* **2009**, *113*, 16002–16008, doi:10.1021/jp9038682.
111. Bajaj, N.S.; Joshi, R.A. Chapter 3 - Energy Materials: Synthesis and Characterization Techniques. In *Energy Materials*; Dhoble, S.J., Kalyani, N.T., Vengadaesvaran, B., Kariem Arof, A., Eds.; Elsevier, 2021; pp. 61–82 ISBN 978-0-12-823710-6.
112. Wu, W.; He, Q.; Jiang, C. Magnetic Iron Oxide Nanoparticles: Synthesis and Surface Functionalization Strategies. *Nanoscale Res Lett* **2008**, *3*, 397, doi:10.1007/s11671-008-9174-9.
113. Munnik, P.; de Jongh, P.E.; de Jong, K.P. Recent Developments in the Synthesis of Supported Catalysts. *Chem. Rev.* **2015**, *115*, 6687–6718, doi:10.1021/cr500486u.
114. Cai, W.; Wan, J. Facile Synthesis of Superparamagnetic Magnetite Nanoparticles in Liquid Polyols. *Journal of Colloid and Interface Science* **2007**, *305*, 366–370, doi:10.1016/j.jcis.2006.10.023.
115. Eid, K.; Wang, H.; Wang, L. Chapter 6 - Nanoarchitectonic Metals. In *Supra-Materials Nanoarchitectonics*; Ariga, K., Aono, M., Eds.; Micro and Nano Technologies; William Andrew Publishing, 2017; pp. 135–171 ISBN 978-0-323-37829-1.
116. Denkbaş, E.B.; Çelik, E.; Erdal, E.; Kavaz, D.; Akbal, Ö.; Kara, G.; Bayram, C. Chapter 9 - Magnetically Based Nanocarriers in Drug Delivery. In *Nanobiomaterials in Drug Delivery*; Grumezescu, A.M., Ed.; William Andrew Publishing, 2016; pp. 285–331 ISBN 978-0-323-42866-8.
117. Bock, C.; Paquet, C.; Couillard, M.; Botton, G.A.; MacDougall, B.R. Size-Selected Synthesis of PtRu Nano-Catalysts: Reaction and Size Control Mechanism. *J. Am. Chem. Soc.* **2004**, *126*, 8028–8037, doi:10.1021/ja0495819.

118. Baranova, E.A.; Bock, C.; Ilin, D.; Wang, D.; MacDougall, B. Infrared Spectroscopy on Size-Controlled Synthesized Pt-Based Nano-Catalysts. *Surface Science* **2006**, *600*, 3502–3511, doi:10.1016/j.susc.2006.07.005.
119. Vega-Chacón, J.; Picasso, G.; Avilés-Félix, L.; Jafelicci, M. Influence of Synthesis Experimental Parameters on the Formation of Magnetite Nanoparticles Prepared by Polyol Method. *Adv. Nat. Sci: Nanosci. Nanotechnol.* **2016**, *7*, 015014, doi:10.1088/2043-6262/7/1/015014.
120. Fiévet, F.; Brayner, R. The Polyol Process. In *Nanomaterials: A Danger or a Promise? A Chemical and Biological Perspective*; Brayner, R., Fiévet, F., Coradin, T., Eds.; Springer: London, 2013; pp. 1–25 ISBN 978-1-4471-4213-3.
121. Panaritis, C.; Zgheib, J.; Ebrahim, S.A.H.; Couillard, M.; Baranova, E.A. Electrochemical In-Situ Activation of Fe-Oxide Nanowires for the Reverse Water Gas Shift Reaction. *Applied Catalysis B: Environmental* **2020**, *269*, 118826, doi:10.1016/j.apcatb.2020.118826.
122. (PDF) Polyol Synthesis of Nanoparticles: A Decade of Advancements and Insights. *ResearchGate* **2024**, doi:10.14233/ajchem.2023.30223.
123. Dahiya, M.S.; Tomer, V.K.; Duhan, S. 31 - Metal–Ferrite Nanocomposites for Targeted Drug Delivery. In *Applications of Nanocomposite Materials in Drug Delivery*; Inamuddin, Asiri, A.M., Mohammad, A., Eds.; Woodhead Publishing Series in Biomaterials; Woodhead Publishing, 2018; pp. 737–760 ISBN 978-0-12-813741-3.
124. Dorey, R. Chapter 2 - Routes to Thick Films: What Is a Thick Film? How Is It Made? In *Ceramic Thick Films for MEMS and Microdevices*; Dorey, R., Ed.; Micro and Nano Technologies; William Andrew Publishing: Oxford, 2012; pp. 35–61 ISBN 978-1-4377-7817-5.
125. Hasany, S.F.; Ahmed, I.; J, R.; Rehman, A. Systematic Review of the Preparation Techniques of Iron Oxide Magnetic Nanoparticles. *Nanoscience and Nanotechnology* **2012**, *2*, 148–158.
126. Tavakoli, A.; Sohrabi, M.; Kargari, A. A Review of Methods for Synthesis of Nanostructured Metals with Emphasis on Iron Compounds. *Chem. Pap.* **2007**, *61*, 151–170, doi:10.2478/s11696-007-0014-7.
127. Daou, T.J.; Pourroy, G.; Bégin-Colin, S.; Grenèche, J.M.; Ulhaq-Bouillet, C.; Legaré, P.; Bernhardt, P.; Leuvrey, C.; Rogez, G. Hydrothermal Synthesis of Monodisperse Magnetite Nanoparticles. *Chem. Mater.* **2006**, *18*, 4399–4404, doi:10.1021/cm060805r.
128. Feng, S.-H.; Li, G.-H. Chapter 4 - Hydrothermal and Solvothermal Syntheses. In *Modern Inorganic Synthetic Chemistry (Second Edition)*; Xu, R., Xu, Y., Eds.; Elsevier: Amsterdam, 2017; pp. 73–104 ISBN 978-0-444-63591-4.
129. Jeyapaul, A.S.; Ganesapillai, M. A Sustainable Solution: Mitigating Sulphur Dioxide Emissions through Adsorption on Chemically Modified Iron Oxide Nanoparticles. *Clean Techn Environ Policy* **2024**, doi:10.1007/s10098-024-02807-0.
130. Clay, D.T.; Lynn, S. Reduction and Removal of SO2 and NOx from Simulated Flue Gas Using Iron Oxide as Catalyst/Absorbent. *AIChE Journal* **1975**, *21*, 466–473, doi:10.1002/aic.690210306.

Chapter 2. Iron oxide-graphene oxide nanocomposites for low-temperature SO_2 removal process

Abstract

Sulfur dioxide (SO_2) still significantly contributes to air pollution. While conventional desulfurization techniques target high SO_2 concentrations, dry adsorption has emerged as an effective method for low-concentration capture. This study aims to synthesize an adsorbent combining the properties of graphene oxide and iron oxides, both showing potential for SO_2 capture. Iron oxide nanoparticles were synthesized using polyol and coprecipitation methods with a 1:2 ratio of iron (III) to iron (II) precursors. The polyol method used ethylene glycol and sodium hydroxide, while the coprecipitation method used water, ammonium hydroxide (NH_4OH), or sodium hydroxide (NaOH). The nanoparticles were deposited on the graphene oxide (GO) surface through wet deposition. Transmission electron microscopy (TEM) and inductively coupled plasma atomic emission spectroscopy (ICP-OES) were used to confirm the deposition of iron nanoparticles, which were identified, in all cases, as Fe_2O_3 through X-ray photoelectron spectroscopy (XPS) analysis. The capture experiments were conducted at room temperature with 25 ppm of SO_2 balanced with argon. The addition of iron oxide increased the capture capacities from 0.6 $mg_{SO2}/g_{sorbent}$ for GO to 1.3, 1.7, and 3.1 $mg_{SO2}/g_{sorbent}$ for GO Fe_2O_3-polyol, GO Fe_2O_3-NaOH, and GO Fe_2O_3-NH_4, respectively. High-resolution XPS analysis suggested that adsorbed SO_2 could be linked to both iron and GO. Finally, regeneration tests indicated an incomplete desorption at 100°C. These findings underscore the potential of GO-iron oxide nanocomposites for SO_2 capture and the significant impact of the iron oxide nanoparticle's properties.

Keywords : sulfur dioxide; graphene oxide; iron oxide; adsorption.

2.1. Introduction

Sulfur dioxide (SO_2) is one of the main gases contributing to air pollution [1]. While volcanic eruptions can naturally release SO_2 into the atmosphere, the predominant source is human activities [2], particularly the combustion of fossil fuels, which account for 87% of SO_x emissions

[3]. Once released, SO_2 can return to the Earth's surface as acid rain or dry acidic particles, posing severe threats to soil health, aquatic ecosystems, and infrastructure [4,5]. Additionally, SO_2 exposure has detrimental effects on the human respiratory system [6].

Conventional flue gas desulfurization (FGD) techniques include wet and dry scrubbers, which rely, respectively on the absorption of SO_2 using an alkaline slurry (limestone) or semi-dry pellets of calcium hydroxide [7,8]. Despite the disadvantages of wet (FGD) namely, wastewater treatments, and high energy consumption [8,9], they remain the most widely used technique and can remove up to 99% of the SO_2 from flue gases [7]. However, these techniques were designed for high SO_2 concentrations [10] and become cost inefficient at lower concentrations due to the need for longer columns and increased water usage. Therefore, it is crucial to develop new techniques to further reduce SO_2 emissions, especially since fossil fuel remains the second largest source of electricity in Canada [3,11].

Over the past years, adsorption has emerged as an attractive option for pollutant removal [3,8,10], particularly when the recovery of the adsorbate is desired or when the adsorbate concentration is low [10,12]. Consequently, it can serve as a supplementary method to the existing ones to achieve higher removal efficiency. This method is appealing due to its simplicity, low energy consumption, and minimal disposal problems [13,14]. Carbon-based adsorbents, in particular, are extensively studied for SO_2 removal due to their high stability against moisture and corrosive gases [9,15].

Porous structure and surface chemistry have been related to the adsorption capacity of the adsorbents for SO_2 removal [16–18]. Researchers have extensively studied the addition of functional groups on material surfaces to improve the adsorption performance [19–24]. Numerous investigations have shown that introducing oxygen functional groups onto the surface of activated carbon and carbon nanotubes can enhance their sorption capacity [19,23,24]. For instance, Liu et al. demonstrated that nitric acid treatment of activated carbon increases the concentration of C=O bonds, serving as Bronsted basic sites for SO_2 oxidation, resulting in enhanced SO_2 removal [19]. Hydroxyl-modified carbon nanotubes exhibit greater sensitivity to SO_2 compared to non-modified carbon nanotubes [24]. Graphene oxide (GO) has the advantage of having multiple oxygen functional groups on its surface [25] and the research conducted by Long et al. revealed that GO can act as both an oxidant and catalyst during SO_2 adsorption by GO foam or suspension at room temperature [26].

Metal oxides supported by carbon-based materials have also been extensively studied to improve carbon material removal capacity [19–22]. Liu et al.'s study demonstrated that the addition of iron oxide nanoparticles (Fe_3O_4) on activated carbon treated with nitric acid further increases the sorption capacity of the material by promoting the oxidation of SO_2 to other compounds with different oxidation states such as SO_3, H_2SO_4 in the presence of water and eventually $FeSO_4$ [19]. Metals-doped carbon nanotubes showed a higher adsorption energy, and charge transfer with SO_2 than pristine carbon nanotubes, suggesting chemical adsorption [21,22,27]. Additionally, graphene oxide-metal oxide nanocomposites have seen extensive application as heterogeneous catalysts in various organic reactions, including oxidation, reduction, and cross-coupling reactions [28,29], as well as serving as adsorbents in wastewater treatments [30].

The size and dispersion of the nanoparticles play important roles in the efficacity of metal oxide-supported nanocomposites [31]. Various factors can shape these characteristics during the synthesis including the choice of salt precursors, the reaction temperature, the pH level, and the reducing agent [32,33]. Therefore, selecting the right synthesis methods becomes important for achieving desired outcomes. The synthesis of iron oxide nanoparticles can be achieved through several common methods including co-precipitation, hydrothermal synthesis, impregnation, and polyol methods [32–34]. Co-precipitation is the most used method due to its simplicity, low energy consumption, and ability to produce water-soluble nanoparticles, although it allows limited control over particle size and distribution [33,35]. The hydrothermal route is the optimal method to produce monodispersed particles with control over their shape and size, but it requires high temperature and pressure [36,37]. Impregnation is typically used to produce supported nanoparticles. However, this method involves catalyst activation by calcination, necessitating a support that can withstand high temperatures [32,34]. While these methods generally use aqueous solvents, the polyol approach utilizes a polyol solution as both solvent and reducing agent [38,39]. This technique produces high crystalline nanoparticles with hydrophilic ligands, facilitating their dispersion in aqueous media and polar solvents [38]. However, the sensitivity of the reaction to temperature, time, and concentration of precursors can make reproducibility difficult [40].

Based on prior research conducted in our laboratory, which demonstrated that adding iron oxide nanoparticles to GO enhances its capture capacity toward SO_2 [41], this study aims to investigate the impact of different nanoparticle synthesis methods on the capture capacity of GO.

Iron oxide nanoparticles were synthesized using co-precipitation and polyol methods, and subsequently deposited onto GO through wet deposition. The resulting GO-iron oxide nanoparticle composites were then utilized to capture SO_2 at room temperature from a gas stream flowing at 15 mL/min, containing 25 ppm of SO_2 balanced with N_2. The objective was to reduce the outlet gas concentration to less than 1 ppm.

2.2. Experimental

2.2.1. Materials

High surface area graphene oxide was obtained from ACS Materials (type B GO) with a reported measured BET-specific surface area of 400 m^2/g. Ethylene glycol (99%), sodium hydroxide (NaOH) pellets, and iron chloride ($FeCl_3$) 98% were obtained from ThermoFisher Scientific. Iron chloride hexahydrate ($FeCl_3 \bullet 6H_2O$) 99%+ and iron sulfate heptahydrate ($FeSO_4 \bullet 7H_2O$) 99.5% were purchased from Acro Organic. Citric acid and ammonium hydroxide solution (NH_4OH) come from VWR chemicals BDH.

2.2.2. Graphene oxide-iron oxide nanocomposite preparation

Polyol method

A 1:2 molar ratio of 0.015 mol/L of Fe^{2+} ($FeSO_4 \bullet 7H_2O$) and 0.03 mol/L of Fe^{3+} ($FeCl_3$) ions were dissolved in 3 mL of ethylene glycol and a 0.25 M solution of sodium hydroxide in ethylene glycol was added dropwise until a pH of around 12 was obtained [42], around 20 mL. Ethylene glycol acted as the solvent and the reducing agent while sodium hydroxide was used to control nanoparticle size [38]. The mixture was then heated under reflux in a paraffin oil bath until the temperature reached 113°C, where the color of the solution changed from black to a rusty brown color, indicating the end of the reaction [42]. The pH dropped from ~12 to ~9. The suspension was then cooled and stored at room temperature.

Co-precipitation

An aqueous precursor solution of 25 mL containing 0.03 mol/L of $FeSO_4 \bullet 7H_2O$, 0.06 mol/L of $FeCl_3 \bullet 6H_2O$, and 0.03 mol/L of citric acid was heated until the temperature reached 80°C. A reducing agent consisting of 10 wt% of a solution of sodium hydroxide (NaOH) or ammonium hydroxide (NH_4OH) was then added to initiate the precipitation reaction. In both cases, the 3 mL

of reducing agent was added until a pH of around 8-9 was obtained. The color changed from yellow to black, indicating the formation of iron oxide. The suspension was cooled and stored at room temperature.

Wet deposition

200 mg of GO was dispersed in 50 mL of deionized water and 1.16 mL of the nanoparticle suspension from the polyol method or 0.825 mL of the nanoparticle suspension obtained from the co-precipitation methods were added (respectively 1.4 wt% and 1.8 wt% iron oxide deposition). The mixture was agitated for a minimum of 48 hours to ensure proper deposition. The mixture was then centrifuged, dried at 60°C for 2 hours, and ground to obtain a black powder of the catalyst iron oxide-supported GO. The nanocomposite containing nanoparticles from the polyol method is named GOFe_2O_3-polyol and the one containing nanoparticles from co-precipitation using NaOH and NH_4OH as reducing agents are respectively named GOFe_2O_3-NaOH and GOFe_2O_3 -NH_4.

2.2.3. SO_2 capture studies

The capture setup contains a quartz tube in which 50 mg of the synthesized adsorbent is introduced and sandwiched between quartz wool. This packed bed reactor is connected to the capture setup that allows either argon flow (to purge the system) or a 25 ppm gas of SO_2 balanced with argon for the capture experiments (see Figure A.1 in the appendices). Mass flow controllers were used to regulate the inlet gas flow rates, and a flow indicator at the reactor outlet measured the exiting flow rate. A Draeger X-am 2500 detector at the reactor outlet measured the SO_2 concentration in ppm per minute. All capture experiments were conducted at room temperature with a flow rate of 15 mL/min. The setup, from the mass flow controllers to the detector, was placed in the fume hood, where the exiting gas was vented.

In the regeneration process at room temperature, argon gas was utilized to desorb the adsorbed SO_2 from the synthesized adsorbent. When the exiting SO_2 gas concentration exceeded 10 ppm (the capture capacity is calculated at 1 and 10 ppm outlet concentration), the inlet gas was switched to argon still at a 15 mL/min flow rate, maintaining room temperature conditions. Desorption was continued until the SO_2 detector indicated 0 ppm in the outlet gas, indicating that no SO_2 gas was coming out of the reactor. For subsequent capture cycles, the gas was switched back to SO_2 without changing the adsorbent or setup.

For the regeneration at 100°C, the reactor (the quartz tube) is inserted into a furnace. Following the capture phase at room temperature, the gas was switched to argon, and the reactor was heated to 100°C at a rate of 5°C/min. A thermocouple was inserted in the outlet end of the reactor, near the adsorbent (sandwiched between quartz wool) to measure the temperature surrounding the material. The heating was stopped once the SO_2 detector showed 0 ppm in the outlet gas. After the reactor had cooled to room temperature, the gas entering the reactor was switched back to SO_2 for the next capture experiment.

2.2.4. Material characterization

Transmission electron microscopy (TEM) was used to examine the surface morphology of the materials. Pristine GO and nanoparticles TEM images were obtained using JEM-2100F FETEM (JOEL) and the TEM of GO-iron oxide was obtained using FEI's Tecnai Osiris TEM equipped with an X-FEG gun at 200 keV. The samples were dispersed in ethanol and a drop of the suspension was deposited onto a holey carbon copper grid. The iron weight percentage on the surface of the synthesized nanocomposites was obtained with inductively coupled plasma optical emission spectroscopy (ICP-OES) analysis done with the Agilent ICP-OES 5100 and 5110 spectrophotometer. Surface elemental analysis and oxidation state were determined using high-resolution X-ray photoelectron spectroscopy (XPS). The analysis was performed using a Thermo Scientific Nexsa G2 XPS with an aluminum-kα monochromatic x-ray source having a spot size of 400 µm. The survey scans were acquired at a 200 eV pass energy and high-resolution scans at 50 eV. The charging effect was corrected with the binding energy of sp^3 carbon hybridization at 284.8 eV [43]. A doublet separation value of 1.2 eV was used for sulfur 2p [44]. Data treatment was performed using Thermo Avantage (version 6.6.0).

2.3. Results and Discussion

2.3.1. Graphene oxide-iron oxide nanocomposites

The co-precipitation methods yielded a black suspension of nanoparticles, with those produced using NaOH as a reducing agent exhibiting magnetic properties. Meanwhile, the polyol method led to a yellowish-brown color. The TEM images of these nanoparticles and GO-iron oxide nanoparticles are shown in Figure 2.1. The nanoparticles produced by the polyol method and co-precipitation with NaOH were agglomerated and have a round shape with sizes less than 10 nm

(Figures 2.1a, b). The co-precipitation with NH_4OH produced even smaller nanoparticles (Figure 2.1c). The deposition of the nanoparticles on GO was confirmed with the TEM images of $GOFe_2O_3$-polyol, $GOFe_2O_3$-NaOH, and $GOFe_2O_3$-NH_4 in Figures 2.1d, e, and f. The thin, paper-like layered structure of graphene oxide [25] (see Figure A.2a), remained unchanged after the deposition of iron oxide nanoparticles. This two-dimensional structure provides a high external surface area for gas adsorption [45,46]. The nanoparticles were homogeneously dispersed on the surface of GO. The presence of iron oxide in all three types of materials was further confirmed through ICP-OES and XPS survey analysis, as presented in Figure 2.2.

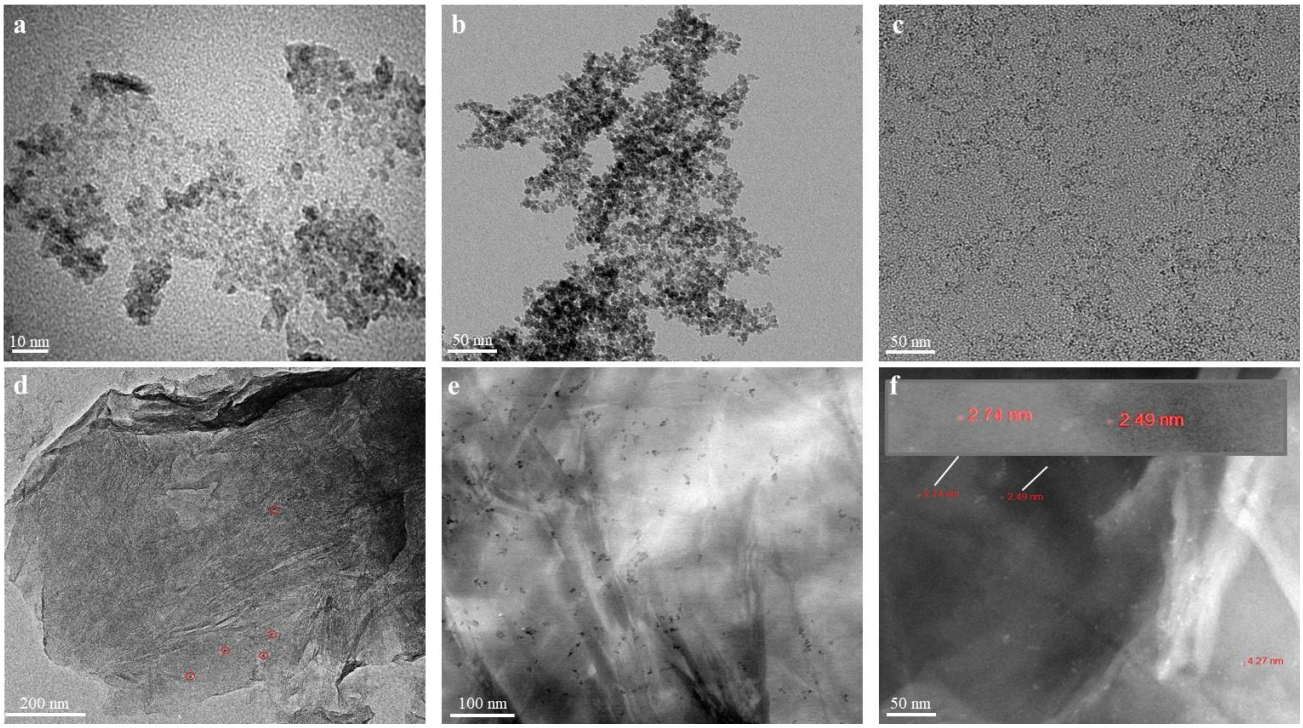

Figure 2.1: TEM of iron oxide nanoparticles from (a) the polyol method, (b) the co-precipitation using NaOH as a reducing agent, and (c) the co-precipitation using NH_4 as a reducing agent; (d) TEM of $GOFe_2O_3$-polyol; (e) STEM-BF of $GOFe_2O_3$-NaOH; (f) STEM-HAADF of $GOFe_2O_3$-NH_4.

The XPS survey of pristine GO in Figure 2.2a showed carbon and oxygen peaks as expected. The high-resolution C1s spectra, shown in Figure 2.2b, displayed the characteristic features of GO, with sp^2 and sp^3 carbon hybridization identified at 284.1 eV and 284.8 eV, respectively [43]. The sp^3 binding energy (BE) was used for calibration in all XPS analyses. Furthermore, the C–O and

C=O bonds were identified at 286.7 eV and 288.7 eV, respectively [43]. The XPS survey also indicated the presence of sulfur, likely a residual from the GO synthesis; the GO used in this study was prepared using the modified Hummer's method, which employs nitric acid and sulfuric acid as oxidizing and exfoliating agents [47]. The high-resolution S2p spectra of pristine GO in Figure 2.2c identified this sulfur species as SO_4^{2-}, with a single S $2p_{3/2}$ peak positioned at 168 eV [48,49].

The deposition of iron on the GO surface was analyzed through XPS survey analysis (Figure 2.2d and Table 2.1) and ICP-OES (Figure 2.2e). The spectra of $GOFe_2O_3$-Polyol before the capture shown in Figure 2.2d, is representative of all the samples (additional spectra can be found in the appendices) and confirm the presence of iron. ICP-OES analysis further validated the deposition of iron, revealing that 82% and 84% of the suspended nanoparticles were effectively deposited onto the GO surface for the polyol and the co-precipitation using NH_4 methods, respectively. In contrast, a lower deposition efficiency was observed for the co-precipitation using NaOH (45%), likely due to the stronger magnetic properties of the nanoparticles, which hinder proper mixing.

Table 2.1: XPS elemental quantitative surface analysis of $GOFe_2O_3$ materials.

Element (At%)	GO	$GOFe_2O_3$-polyol	$GOFe_2O_3$-NaOH	$GOFe_2O_3$-NH_4
Carbon	69.09	71.27	68.81	68.95
Oxygen	30.17	28.05	30.71	29.86
Sulfur	0.075	0.05	0.08	0.08
Iron	0.07	0.35	0.29	0.48

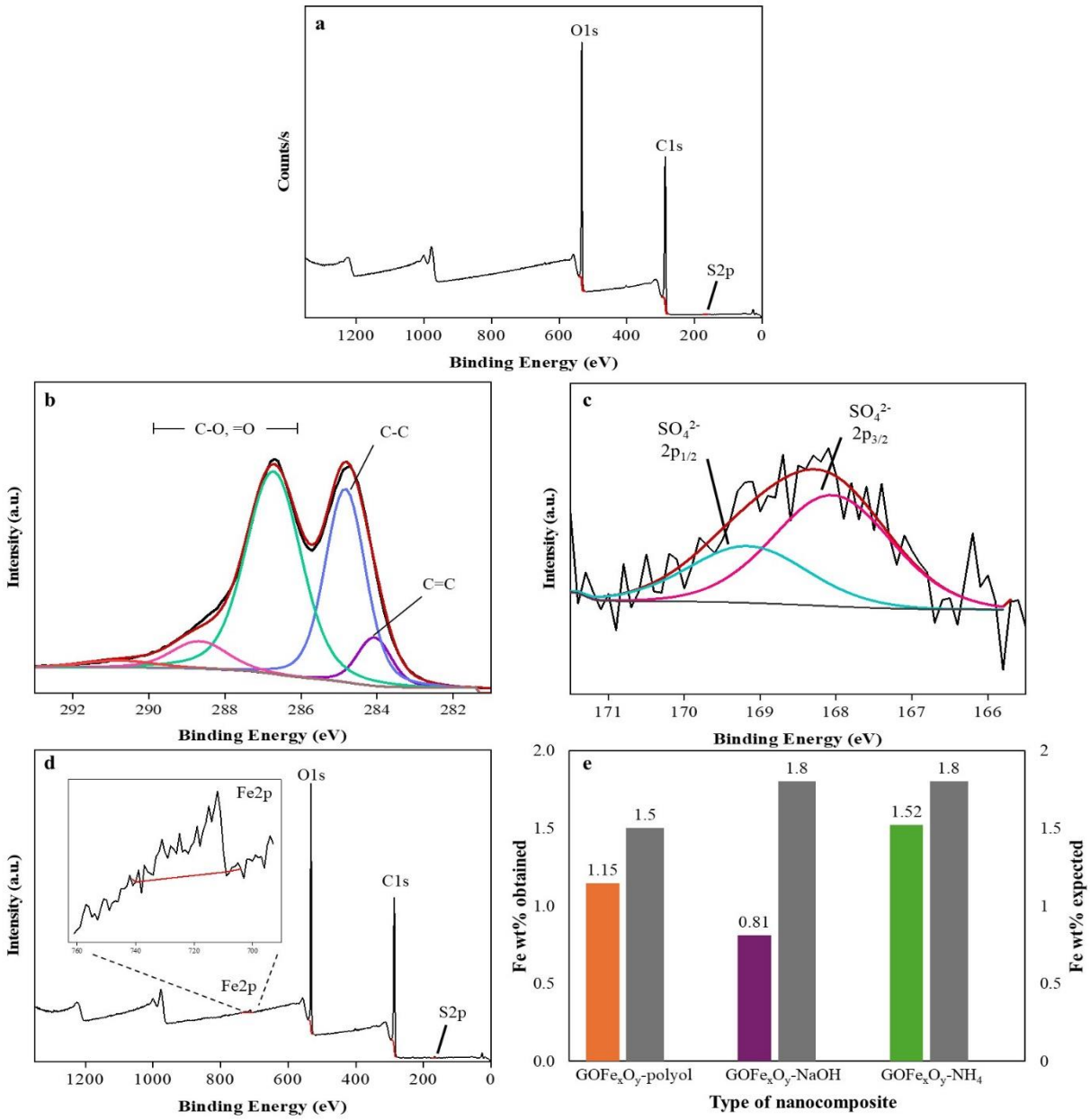

Figure 2.2: (a) XPS survey of pristine GO; high-resolution C1s spectra (b) and S 2p spectra (c) of pristine GO; (d) XPS survey of $GOFe_2O_3$-polyol; (e) ICP-OES analysis presenting the weight percentage of iron on the surface of GO-iron oxide nanocomposites after iron deposition.

To assess the oxidation state of the iron deposited on the GO surface, high-resolution analyses of iron 2p with deconvolution were performed using Thermo Avantage (version 6.6.0). The Fe 2p spectra in Figures 2.3a, b, and c show a peak between 710.8 eV and 711.5 eV, corresponding to

Fe_2O_3 [48,50]. Fe_3O_4 would appear between 708.3 eV and 710.7 eV [49–51] and was therefore not detected. To confirm, the peak of Fe_3O_4 was tentatively added but would result in a very small peak or not at the proper binding energy to minimize the error of the resulting calculated curve. Although Fe_3O_4 might be present in small amounts, it was not possible to confirm its presence through XPS. No FeO or metallic iron, which would be at 709 eV and 707 eV respectively, [50,52] were detected. Additionally, the broadness of the Fe 2p peaks suggests the presence of other iron compounds, possibly $FeSO_4$. As previously discussed, sulfur was detected in all the samples before the capture (Figure 2.2 and Table 2.1) and the S 2p analysis of GO identified these species as SO_4^{2-} (Figure 2.2b). Since iron is the only metal element on the surface of the samples, the presence of $FeSO_4$, which has a binding energy of around 713.5 eV [48], is plausible.

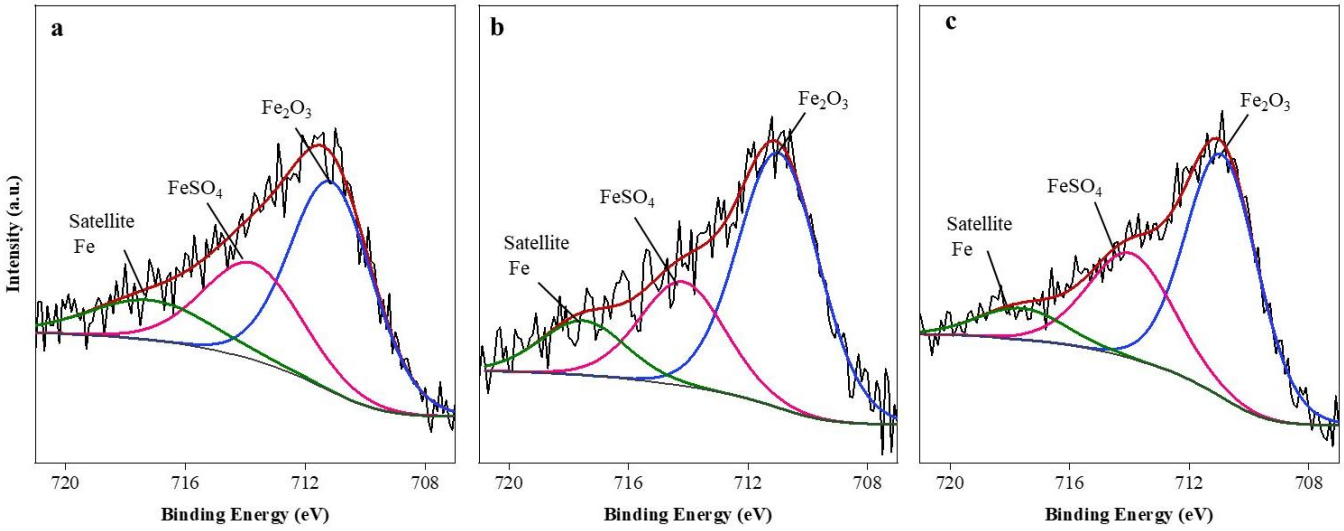

Figure 2.3: High-resolution Fe2p spectra of (a) $GOFe_2O_3$-polyol; (b) $GOFe_2O_3$-NaOH; (c) $GOFe_2O_3$-NH_4 before capture.

2.3.2. SO_2 capture

Capture capacity of the synthesized materials

The capture experiments were conducted at room temperature with a SO_2 gas flow rate of 15 mL/min. The SO_2 capture was done in triplicate for each type of sample and the average data is presented in Figure 2.4a. The blank curve was done without adsorbent, resulting in a steep slope with no capture (a breakthrough time corresponding only to the space-time in the system). The

blank serves to measure the concentration of SO_2 detectable by the SO_2 gas detector, with C_0 representing the maximum concentration of SO_2 measured by the detector, at 25 ppm.

As expected, the breakthrough time increased when GO was used as an adsorbent and further increased when GO modified with iron oxide nanoparticles was used, indicating that graphene oxide can act as an effective sorbent for SO_2 removal, with enhanced capture efficiency in the presence of iron oxide nanoparticles [41]. The addition of the iron oxide nanoparticles on the GO surface increased the breakthrough time by 70% for GOFe_2O_3-polyol, 200% for GOFe_2O_3-NaOH, and by more than 600% for GOFe_2O_3-NH_4 compared to pristine GO. The capacities of the synthesized materials at 1 ppm were 0.6, 1.3, 1.7, and 3.1 mg $SO_2/g_{sorbent}$ for GO, GOFe_2O_3-polyol, GOFe_2O_3-NaOH, and GOFe_2O_3-NH_4 respectively as presented in Figure 2.4b.

The higher capture capacity of GOFe_2O_3-NH_4 can be partially attributed to the higher weight concentration of nanoparticles deposited on the GO surface. However, the iron content of GOFe_2O_3-NH_4 is only 1.3 times higher than that of GOFe_2O_3-polyol (Figure 2.2e), yet it results in a 2.4 times increase in capture capacity. This difference highlights the efficiency of the co-precipitation method using NH_4 for nanoparticle synthesis in enhancing SO_2 capture. Additionally, GOFe_2O_3-NaOH materials demonstrated a higher capture capacity than GOFe_2O_3-polyol despite the presence of more nanoparticles in the latter. The method of nanoparticle synthesis, rather than just the quantity of nanoparticles, significantly impacts the performance of the nanocomposite. GOFe_2O_3-NaOH and GOFe_2O_3-NH_4 have the same mass of SO_2 captured per mass of iron content (207 mg SO_2/g_{Fe} as shown in Table 2.2) despite the low iron content of GOFe_2O_3-NaOH (0.81% and 1.51% for GOFe_2O_3-NH_4). This indicates the importance of the interaction between the iron oxide nanoparticles and the surface of GO. A more effective interaction, which results in a higher concentration of iron on the GO surface, leads to enhanced capture capacity of GO-iron oxide materials.

To evaluate the performance of iron oxide without support, additional capture experiments were conducted using iron oxide nanoparticles from co-precipitation with NaOH under the same conditions (room temperature and 15 mL/min). The particles were successfully isolated through centrifugation, then washed, and dried. To prevent channeling, 5 mg of iron oxide was used as adsorbent — 92% more than the corresponding amount of iron oxide in the 50 mg of GOFe_2O_3-NaOH used for other capture experiments. The capture experiment was conducted in triplicate using different batches, and the average capacity is presented in Figure 2.4.c. The corresponding

breakthrough curves are available in Figure A.3 of the appendices. While the SO_2 capture tests revealed a higher average capacity on the total amount of adsorbent, the capacity was significantly lower considering the relative amount of iron used, at 16.5±1.8 mg $SO_2/g_{Fe,}$ compared to 207.0 mg SO_2/g_{Fe} achieved with 0.81% of iron in $GOFe_2O_3$-NaOH. This highlights the critical role of nanoparticle dispersion on the GO surface.

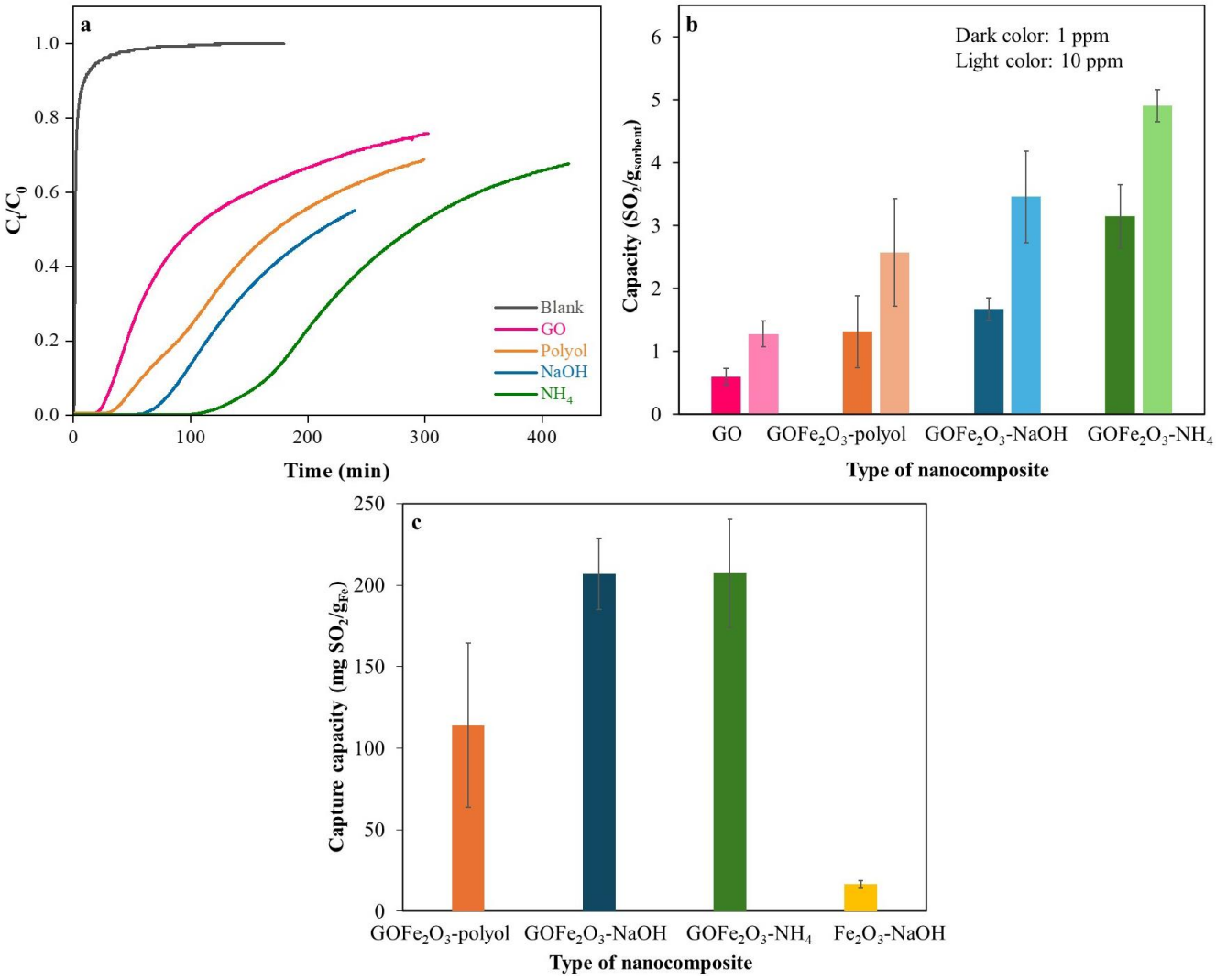

Figure 2.4: (a) breakthrough curves of GO, $GOFe_2O_3$-polyol, $GOFe_2O_3$-NaOH, and $GOFe_2O_3$-NH_4 samples used for SO_2 capture at 20°C and 15 mL/min; (b) capture capacity in mg $SO_2/g_{sorbent}$ at 1 and 10 ppm of the GO-iron oxide nanocomposites; (c) capture capacity in mgSO_2/g_{Fe} at 1 ppm of GO-iron oxide nanocomposites and iron oxide.

Table 2.2: SO_2 capture capacity of GO, GO-iron oxide materials, and iron oxide in mg $SO_2/g_{sorbent}$ and mg SO_2/g_{Fe} at 1 ppm.

	GO	$GOFe_2O_3$-polyol	$GOFe_2O_3$-NaOH	$GOFe_2O_3$-NH_4	Fe_2O_3-NaOH
Capture capacity (mg $SO_2/g_{sorbent}$)	0.6±0.1	1.3±0.6	1.7±0.2	3.1±0.5	16.5±1.8
Capture capacity relative to Fe wt% (mg SO_2/g_{Fe})	-	114.1±50	207.0±21	207.2±33	16.5±1.8

Compared to other adsorbents, the proposed material shows a notable SO_2 capture capacity. For instance, an amine-functionalized nanocellulose adsorbent under similar conditions achieved a capture capacity of 2 mg $SO_2/g_{sorbent}$ [53]. Another adsorbent, composed of metal oxide, demonstrated a capture capacity of 31 mg $SO_2/g_{sorbent}$ under ambient conditions, with an inlet SO_2 concentration of 100 ppm and 500 mg of adsorbent [54]. Several factors influence SO_2 adsorption capacity, including the inlet SO_2 concentration, the adsorbent concentration, operating temperature, and pressure [55–57]. Lower inlet SO_2 concentrations typically result in reduced adsorption capacity [57]. Therefore, direct comparisons between adsorbents can be challenging due to variations in experimental conditions. Furthermore, this study aims to achieve an outlet SO_2 concentration of less than 1 ppm using a low inlet SO_2 concentration.

Species on the surface of GO-iron composite

The Fe 2p analyses of the GO-iron oxide samples after capture and the S 2p analyses of the GO-iron oxide samples before and after capture are presented in Figure 2.5. The Fe 2p spectra (Figures 2.5a, b, and c) still show the Fe_2O_3 peak (between 710.8 eV and 711.5 eV) and the $FeSO_4$ peak around 713.5 eV. The sulfate species were identified between 168 and 169 eV [48,58]. Table 2.3 presents a semi-quantitative analysis of the variation in iron and sulfur species on the nanocomposite surface based on peak areas from the high-resolution XPS analysis, before and after the capture. The amount of SO_4^{2-} increased for all the samples after the SO_2 capture, with $GOFe_2O_3$-NaOH showing the highest increase. The increase in sulfate compounds is consistent with the adsorption of sulfur molecules. However, the increase in $FeSO_4$ is not high compared to the total sulfur content after the capture, which is probably due to a range of adsorption sites with

the weakest adsorbed molecules being desorbed during the sample preparation or analysis at vacuum for XPS. These interactions would then not have been captured during XPS analysis. It therefore indicates the possibility of weak physisorption combined with adsorption that tends toward chemisorption due to different types of adsorption sites. Additionally, sulfate compounds were also identified on graphene oxide without iron oxide. However, no carbon-sulfur bond was detected, as its S $2p_{3/2}$ biding energy would be at 163 eV [59]. The C–S peak could have overlapped with the C–O band in C 1s spectra (Figure 2.2a) as the binding energy is at 287 eV [60]. The low concentration of sulfur on the surface (less than 0.20% of the surface atom) also complicates the identification of specific interactions.

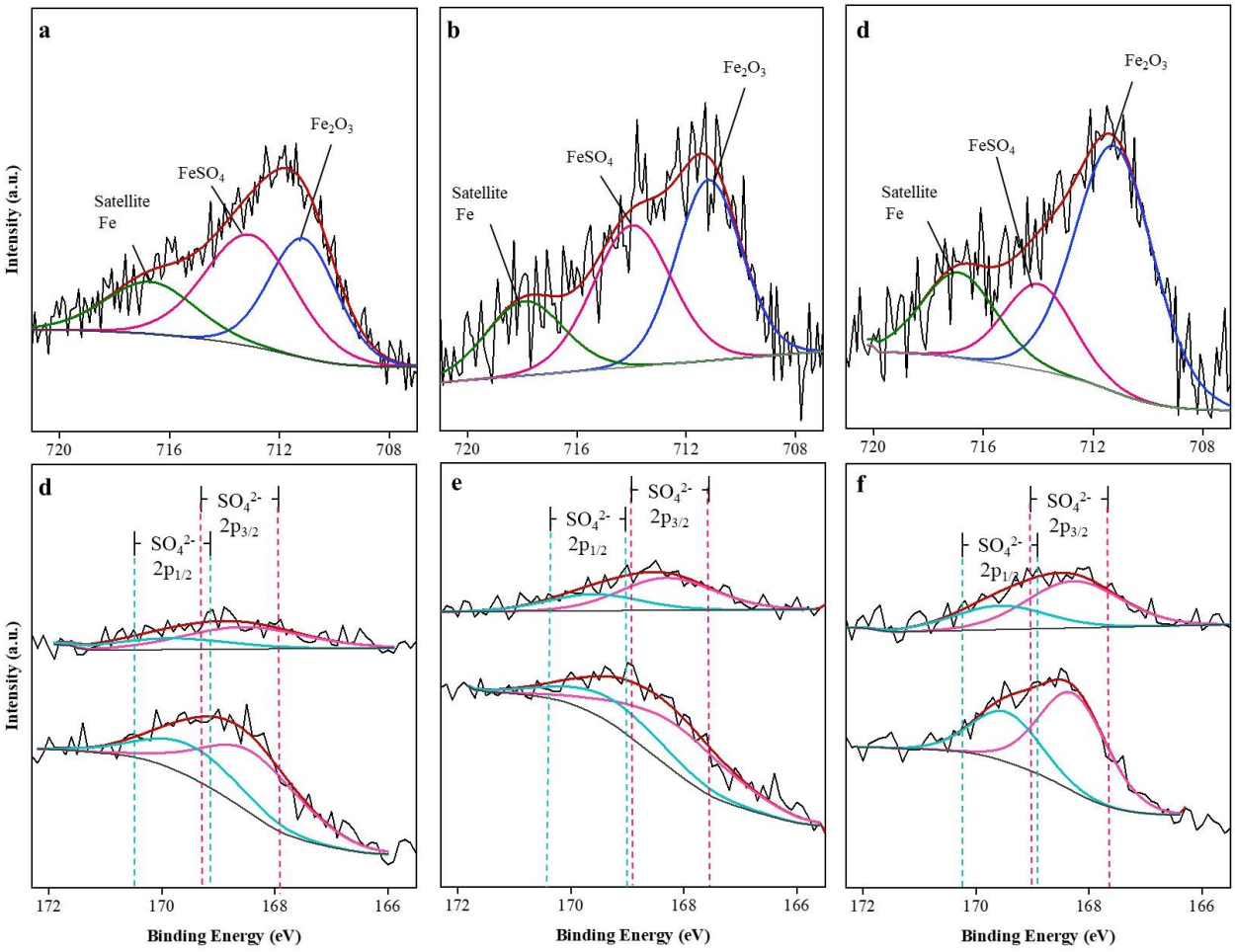

Figure 2.5: High-resolution XPS spectra of iron 2p after SO_2 capture and sulfur 2p before and after SO_2 capture for $GOFe_2O_3$-polyol (a, d), $GOFe_2O_3$-NaOH (b, e), and $GOFe_2O_3$-NH_4 (c, f). The dashed lines indicate the potential position of the peak center.

Table 2.3: Iron sulfate to iron oxide ratio and area under the S $2p_{3/2}$ peak for GO-iron oxide materials.

Samples name	**$FeSO_4/Fe_2O_3$ area ratio**		**The area under S $2p_{3/2}$**	
	Before	After	Before	After
GO	-	-	360	830
$GOFe_2O_3$-polyol	0.64	0.87	480	800
$GOFe_2O_3$-NaOH	0.54	0.65	530	1160
$GOFe_2O_3$-NH_4	0.63	0.59	630	950

Regeneration

For the regeneration tests, the material with the highest capture capacity ($GOFe_2O_3$-NH_4) was used. The capture experiments were done at 25°C and the regeneration was done at two different temperatures, 25°C and 100°C. After the first adsorption at 25°C, argon gas at a flow rate of 15 mL/min was introduced into the system for gas adsorption. The resulting breakthrough curves are presented in Figures 2.6a and b and the associated capture capacities are shown in Figures 2.6c and d. The term "cycle" refers to the number of capture experiments. The concentration of SO_2 released during the 25°C regeneration slightly increased from 12.6 ppm to 13 ppm, then dropped to 0 ppm. The measured SO_2 during this phase may represent the residual gas within the system rather than the gas desorbed from the surface of GO. Meanwhile, during 100°C regeneration, the SO_2 concentration reached the gas detector detection limit of 100 ppm and maintained this level for approximately 8 minutes before starting to decrease. However, the desorption was incomplete as only 32.9% of the adsorbed SO_2 was released during the first regeneration and 15.9% during the second. This indicates the presence of various bond types between SO_2 and the GO-iron composite, with some bonds being more resilient to thermal desorption at 100°C than others.

It can be seen from Figure 2.6 that both the breakthrough time and capture capacity decreased after the first capture in the two regeneration scenarios. This reduction in performance may be attributed to the reduction in the adsorption sites after the first capture. However, the performance decline between the fresh adsorbent and the 2^{nd} used adsorbent was more pronounced when the regeneration temperature was 100°C, although more sulfur was desorbed. Part of the reduction in performance is because the desorption is not complete and the second reason is a potential material

decomposition. Research by Siegfried et al. shows that CO_2 formation starts at 50°C and continues up to 120°C during thermal annealing of GO and explains this as results from the removal of carbon from the basal plane or edge, leading to defects in the carbon sheet structure [62]. However, the carbon loss at 50°C is minimal, as indicated by their TGA-MS analysis, which barely detects CO_2 until 130°C. Additionally, the capture capacity seems to stabilize after the second capture, suggesting that material decomposition has stopped and that only weakly adsorbed SO_2 was removed during the second desorption. Nonetheless, additional regeneration cycles are needed to confirm the material's stability.

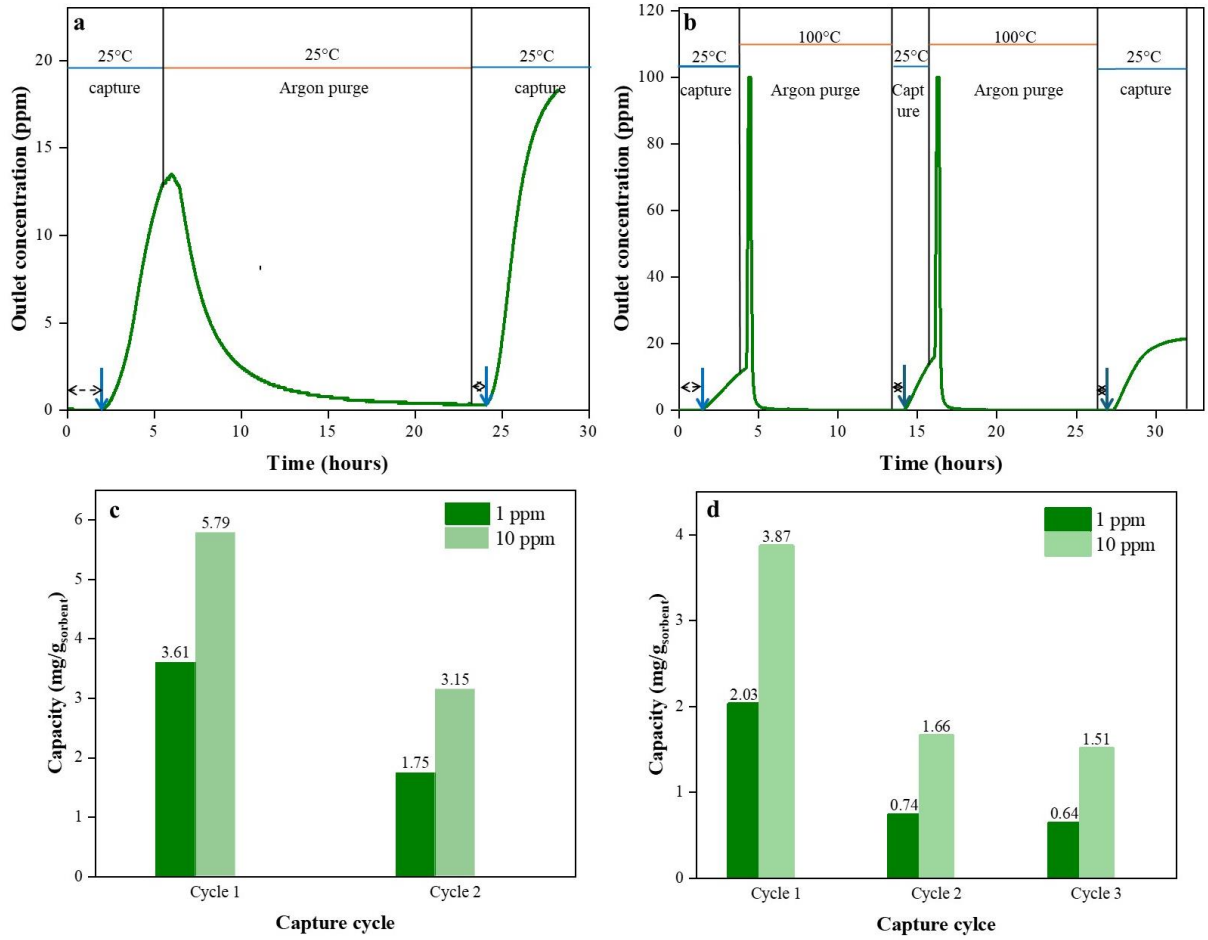

Figure 2.6: Regeneration tests at (a) 25°C and (b) 100°C of $GOFe_2O_3$-NH_4 nanocomposites. The capture experiments were conducted at 25 °C and 15 mL/min. Capture capacities at 1 ppm and 10 ppm for the capture tests conducted at (c) 25°C and (d) 100°C.

2.4. Conclusions

In this study, iron oxide nanoparticles were synthesized using the polyol method, and co-precipitation with NaOH or NH_4 as reducing agents. The deposition of iron oxide nanoparticles on the graphene oxide was confirmed through TEM, ICP-OES, and XPS analysis. The deposited nanoparticles were less than 10 nm in size and homogeneously dispersed on the support and homogeneously dispersed on the GO surface. Fe 2p high-resolution XPS spectra identified the presence of Fe_2O_3 on GO for the three synthesized materials.

The breakthrough curves and capture capacities of GO and GO-iron oxide demonstrated that the addition of iron significantly increases the performance of graphene oxide, with $GOFe_2O_3$-NH_4 having the highest increase of about 400%. The type and concentration of nanoparticles were found to play an important role in improving capture capacity. Notably, $GOFe_2O_3$-NaOH showed the same performance as $GOFe_2O_3$-NH_4 in terms mass of SO_2 per mass of iron, despite having 47% less iron on the GO surface. Moreover, supported iron oxide nanoparticles have a better capture capacity than bulk iron oxide material. The S 2p spectra of GO indicated the presence of sulfate species even before SO_2 capture, and the amount of sulfate increased for all the materials after the experiment, confirming the effective SO_2 capture.

In the regeneration experiments, the material's capture capacity decreased after the first cycle, with SO_2 desorption being incomplete even at 100°C, suggesting the presence of different types of bonds between SO_2 and the GO-iron oxide surface. However, the capture capacity appeared to stabilize after the second regeneration at 100°C.

Further studies will focus on identifying the interactions between the adsorbed SO_2 and the material by increasing the iron concentration on the surface of graphene oxide. Additionally, more regeneration experiences with multiple cycles will be conducted to confirm the material's stability over time. Furthermore, the effect of temperature and other flue gas components, such as CO_2, O_2, and moisture on SO_2 adsorption will also be investigated.

References

1. Canada's Air Pollutant Emissions Inventory Report 2023: Chapter 2.2 (accessed on 25 September 2023).
2. Read, A. Sulphur Dioxide and Health : Summary of Recent Findings from Health Canada Available online: //www.pembina.org/pubs (accessed on 27 May 2024).
3. Rezaei, F.; Rownaghi, A.A.; Monjezi, S.; Lively, R.P.; Jones, C.W. SOx/NOx Removal from Flue Gas Streams by Solid Adsorbents: A Review of Current Challenges and Future Directions. *Energy Fuels* **2015**, *29*, 5467–5486, doi:10.1021/acs.energyfuels.5b01286.
4. A. Tewari; N. P. Shukla Air Pollution - Adverse Effects of Sulfur Dioxide. *Reviews on Environmental Health* **1991**, *9*, 39–46, doi:10.1515/REVEH.1991.9.1.39.
5. US EPA, O. Effects of Acid Rain Available online: https://www.epa.gov/acidrain/effects-acid-rain (accessed on 21 January 2024).
6. Khalaf, E.M.; Mohammadi, M.J.; Sulistiyani, S.; Ramírez-Coronel, A.A.; Kiani, F.; Jalil, A.T.; Almulla, A.F.; Asban, P.; Farhadi, M.; Derikondi, M. Effects of Sulfur Dioxide Inhalation on Human Health: A Review. *Reviews on Environmental Health* **2022**, doi:10.1515/reveh-2022-0237.
7. Poullikkas, A. Review of Design, Operating, and Financial Considerations in Flue Gas Desulfurization Systems. *Energy Technology & Policy* **2015**, *2*, 92–103, doi:10.1080/23317000.2015.1064794.
8. Ahmadian, M.; Anbia, M.; Rezaie, M. Sulfur Dioxide Removal from Flue Gas by Supported CuO Nanoparticle Adsorbents. *Ind. Eng. Chem. Res.* **2020**, *59*, 21642–21653, doi:10.1021/acs.iecr.0c05629.
9. Hu, Z.; Xie, H.; Wang, Q.; Chen, S. Adsorption and Diffusion of Sulfur Dioxide and Nitrogen in Single-Wall Carbon Nanotubes. *Journal of Molecular Graphics and Modelling* **2019**, *88*, 62–70, doi:10.1016/j.jmgm.2019.01.003.
10. Yu, X.; Hao, J.; Xi, Z.; Liu, T.; Lin, Y.; Xu, B. Investigation of Low Concentration SO2 Adsorption Performance on Different Amine-Modified Merrifield Resins. *Atmospheric Pollution Research* **2019**, *10*, 404–411, doi:10.1016/j.apr.2018.08.015.
11. Canada, N.R. About-Electricity Available online: https://www.nrcan.gc.ca/our-natural-resources/energy-sources-distribution/electricity-infrastructure/about-electricity/7359 (accessed on 19 July 2022).
12. Carlson, J. Air Pollution Control Technology Review: Adsorption Available online: https://www.cpilink.com/blog/air-pollution-control-technology-review-adsorption-2 (accessed on 4 February 2024).
13. Erdoğan Alver, B. A Comparative Adsorption Study of C2H4 and SO2 on Clinoptilolite-Rich Tuff: Effect of Acid Treatment. *Journal of Hazardous Materials* **2013**, *262*, 627–633, doi:10.1016/j.jhazmat.2013.09.014.
14. Meimand, M.M.; Jafari, A.J.; Nasiri, A.; Malakootian, M. Sulfur Dioxide Adsorption by Iron Oxide Nanoparticles@clinoptilolite/HCl. *Journal of Air Pollution and Health* **2020**, *5*, 107–120, doi:10.18502/japh.v5i2.4239.
15. Babu, D.J.; Puthusseri, D.; Kühl, F.G.; Okeil, S.; Bruns, M.; Hampe, M.; Schneider, J.J. SO2 Gas Adsorption on Carbon Nanomaterials: A Comparative Study. *Beilstein J Nanotechnol* **2018**, *9*, 1782–1792, doi:10.3762/bjnano.9.169.

16. Raymundo-Piñero, E.; Cazorla-Amorós, D.; Salinas-Martinez de Lecea, C.; Linares-Solano, A. Factors Controling the SO2 Removal by Porous Carbons: Relevance of the SO2 Oxidation Step. *Carbon* **2000**, *38*, 335–344, doi:10.1016/S0008-6223(99)00109-8.
17. Ren, X.; Chen, C.; Nagatsu, M.; Wang, X. Carbon Nanotubes as Adsorbents in Environmental Pollution Management: A Review. *Chemical Engineering Journal* **2011**, *170*, 395–410, doi:10.1016/j.cej.2010.08.045.
18. Sun, F.; Gao, J.; Zhu, Y.; Chen, G.; Wu, S.; Qin, Y. Adsorption of SO2 by Typical Carbonaceous Material: A Comparative Study of Carbon Nanotubes and Activated Carbons. *Adsorption* **2013**, *19*, 959–966, doi:10.1007/s10450-013-9504-9.
19. Liu, X.-L.; Guo, J.-X.; Chu, Y.-H.; Luo, D.-M.; Yin, H.-Q.; Sun, M.-C.; Yavuz, R. Desulfurization Performance of Iron Supported on Activated Carbon. *Fuel* **2014**, *123*, 93–100, doi:10.1016/j.fuel.2014.01.068.
20. Davini, P. The Effect of Certain Metallic Derivatives on the Adsorption of Sulphur Dioxide on Active Carbon. *Carbon* **2001**, *39*, 419–424, doi:10.1016/S0008-6223(00)00134-2.
21. An, L.; Jia, X.; Liu, Y. Adsorption of SO_2 Molecules on Fe-Doped Carbon Nanotubes: The First Principles Study. *Adsorption* **2019**, *25*, 217–224, doi:10.1007/s10450-019-00026-4.
22. Li, W.; Ma, J.-J.; Liu, P.; Pan, Z.-L.; He, Q.-Y. First-Principles Study of the Adsorption Sensitivity of Ni-Doped Single-Walled Zigzag (n,0)CNTs (N=4,5,6) toward SO2 Molecules. *Applied Surface Science* **2015**, *335*, 17–22, doi:10.1016/j.apsusc.2015.01.181.
23. Zhang, X.; Cui, H.; Gui, Y.; Tang, J. Mechanism and Application of Carbon Nanotube Sensors in SF6 Decomposed Production Detection: A Review. *Nanoscale Res Lett* **2017**, *12*, 177, doi:10.1186/s11671-017-1945-8.
24. Zhang, X.; Meng, F.; Yang, B. Use of Hydroxyl-Modified Carbon Nanotubes for Detecting SF6 Decomposition Products under Partial Discharge in Gas Insulated Switchgear. *IEEE Transactions on Dielectrics and Electrical Insulation* **2013**, *20*, 2246–2253, doi:10.1109/TDEI.2013.6678876.
25. Dreyer, D.R.; Park, S.; Bielawski, C.W.; Ruoff, R.S. The Chemistry of Graphene Oxide. *Chem. Soc. Rev.* **2009**, *39*, 228–240, doi:10.1039/B917103G.
26. Long, Y.; Zhang, C.; Wang, X.; Gao, J.; Wang, W.; Liu, Y. Oxidation of SO_2 to SO_3 Catalyzed by Graphene Oxide Foams. *J. Mater. Chem.* **2011**, *21*, 13934–13941, doi:10.1039/C1JM12031J.
27. Lu, X.; Sun, C.; Li, F.; Cheng, H.-M. Selected Absorption Behavior of Sulfur on Single-Walled Carbon Nanotubes by DFT. *Chemical Physics Letters* **2008**, *454*, 305–309, doi:10.1016/j.cplett.2008.02.027.
28. Shabestari, M.E.; Martín, O.; Díaz-García, D.; Gómez-Ruiz, S.; Gonzalez, V.J.; Baselga, J. Facile and Rapid Decoration of Graphene Oxide with Copper Double Salt, Oxides and Metallic Copper as Catalysts in Oxidation and Coupling Reactions. *Carbon* **2020**, *161*, 7–16, doi:10.1016/j.carbon.2020.01.015.
29. Soni, J.; Sethiya, A.; Sahiba, N.; Agarwal, S. Recent Advancements in Organic Synthesis Catalyzed by Graphene Oxide Metal Composites as Heterogeneous Nanocatalysts. *Applied Organometallic Chemistry* **2021**, *35*, e6162, doi:10.1002/aoc.6162.
30. Su, H.; Ye, Z.; Hmidi, N. High-Performance Iron Oxide-Graphene Oxide Nanocomposite Adsorbents for Arsenic Removal. *Colloids and Surfaces A: Physicochemical and Engineering Aspects* **2017**, *522*, doi:10.1016/j.colsurfa.2017.02.065.
31. Narayan, N.; Meiyazhagan, A.; Vajtai, R. Metal Nanoparticles as Green Catalysts. *Materials (Basel)* **2019**, *12*, 3602, doi:10.3390/ma12213602.

32. Campanati, M.; Fornasari, G.; Vaccari, A. Fundamentals in the Preparation of Heterogeneous Catalysts. *Catalysis Today* **2003**, *77*, 299–314, doi:10.1016/S0920-5861(02)00375-9.
33. da Silva, A.K.; Ricci, T.G.; de Toffoli, A.L.; Maciel, E.V.S.; Nazario, C.E.D.; Lanças, F.M. Chapter 4 - The Role of Magnetic Nanomaterials in Miniaturized Sample Preparation Techniques. In *Handbook on Miniaturization in Analytical Chemistry*; Hussain, C.M., Ed.; Elsevier, 2020; pp. 77–98 ISBN 978-0-12-819763-9.
34. Perego, C.; Villa, P. Catalyst Preparation Methods. *Catalysis Today* **1997**, *34*, 281–305, doi:10.1016/S0920-5861(96)00055-7.
35. Shnoudeh, A.J.; Hamad, I.; Abdo, R.W.; Qadumii, L.; Jaber, A.Y.; Surchi, H.S. Chapter 15 - Synthesis, Characterization, and Applications of Metal Nanoparticles. In *Biomaterials and Bionanotechnology*; Academic Press, 2019; pp. 527–612 ISBN 978-0-12-814427-5.
36. Dorey, R. Chapter 2 - Routes to Thick Films: What Is a Thick Film? How Is It Made? In *Ceramic Thick Films for MEMS and Microdevices*; Dorey, R., Ed.; Micro and Nano Technologies; William Andrew Publishing: Oxford, 2012; pp. 35–61 ISBN 978-1-4377-7817-5.
37. Feng, S.-H.; Li, G.-H. Chapter 4 - Hydrothermal and Solvothermal Syntheses. In *Modern Inorganic Synthetic Chemistry (Second Edition)*; Xu, R., Xu, Y., Eds.; Elsevier: Amsterdam, 2017; pp. 73–104 ISBN 978-0-444-63591-4.
38. Cai, W.; Wan, J. Facile Synthesis of Superparamagnetic Magnetite Nanoparticles in Liquid Polyols. *Journal of Colloid and Interface Science* **2007**, *305*, 366–370, doi:10.1016/j.jcis.2006.10.023.
39. Hasany, S.F.; Ahmed, I.; J, R.; Rehman, A. Systematic Review of the Preparation Techniques of Iron Oxide Magnetic Nanoparticles. *Nanoscience and Nanotechnology* **2012**, *2*, 148–158.
40. (PDF) Polyol Synthesis of Nanoparticles: A Decade of Advancements and Insights. *ResearchGate* **2024**, doi:10.14233/ajchem.2023.30223.
41. Sanyal, T.S.; Mugisha, A.I.; Sowinski, A.; Fauteux-Lefebvre, C. Enhancement of Sulfur Oxide Capture Capacity by Deposition of Iron Oxide Particles on Graphene Oxide. *Catalysts* **2023**, *13*, 1469, doi:10.3390/catal13121469.
42. Panaritis, C.; Zgheib, J.; Ebrahim, S.A.H.; Couillard, M.; Baranova, E.A. Electrochemical In-Situ Activation of Fe-Oxide Nanowires for the Reverse Water Gas Shift Reaction. *Applied Catalysis B: Environmental* **2020**, *269*, 118826, doi:10.1016/j.apcatb.2020.118826.
43. Dave, K.; Park, K.H.; Dhayal, M. Two-Step Process for Programmable Removal of Oxygen Functionalities of Graphene Oxide: Functional, Structural and Electrical Characteristics. *RSC Adv.* **2015**, *5*, 95657–95665, doi:10.1039/C5RA18880F.
44. Naumkin, A.V.; Kraut-Vass, A.; Gaarenstroom, S.W.; Powell, C.J. X-Ray Photoelectron Spectroscopy Database XPS, NIST Standard Reference Database 20 2012.
45. Jiříčková, A.; Jankovský, O.; Sofer, Z.; Sedmidubský, D. Synthesis and Applications of Graphene Oxide. *Materials (Basel)* **2022**, *15*, 920, doi:10.3390/ma15030920.
46. Shanmugam, V.; Mensah, R.A.; Babu, K.; Gawusu, S.; Chanda, A.; Tu, Y.; Neisiany, R.E.; Försth, M.; Sas, G.; Das, O. A Review of the Synthesis, Properties, and Applications of 2D Materials. *Particle & Particle Systems Characterization* **2022**, *39*, 2200031, doi:10.1002/ppsc.202200031.

47. Kaur, M.; Kaur, H.; Kukkar, D. Synthesis and Characterization of Graphene Oxide Using Modified Hummer's Method. *AIP Conference Proceedings* **2018**, *1953*, 030180, doi:10.1063/1.5032515.
48. Descostes, M.; Mercier, F.; Thromat, N.; Beaucaire, C.; Gautier-Soyer, M. Use of XPS in the Determination of Chemical Environment and Oxidation State of Iron and Sulfur Samples: Constitution of a Data Basis in Binding Energies for Fe and S Reference Compounds and Applications to the Evidence of Surface Species of an Oxidized Pyrite in a Carbonate Medium. *Applied Surface Science* **2000**, *165*, 288–302, doi:10.1016/S0169-4332(00)00443-8.
49. Brion, D. Etude Par Spectroscopie de Photoelectrons de La Degradation Superficielle de FeS2, CuFeS2, ZnS et PbS a l'air et Dans l'eau. *Applications of Surface Science* **1980**, *5*, 133–152, doi:10.1016/0378-5963(80)90148-8.
50. Langevoort, J.C.; Sutherland, I.; Hanekamp, L.J.; Gellings, P.J. On the Oxide Formation on Stainless Steels AISI 304 and Incoloy 800H Investigated with XPS. *Applied Surface Science* **1987**, *28*, 167–179, doi:10.1016/0169-4332(87)90062-6.
51. McIntyre, N.S.; Zetaruk, D.G. X-Ray Photoelectron Spectroscopic Studies of Iron Oxides. *Anal. Chem.* **1977**, *49*, 1521–1529, doi:10.1021/ac50019a016.
52. Muhler, M.; Schlögl, R.; Ertl, G. The Nature of the Iron Oxide-Based Catalyst for Dehydrogenation of Ethylbenzene to Styrene 2. Surface Chemistry of the Active Phase. *Journal of Catalysis* **1992**, *138*, 413–444, doi:10.1016/0021-9517(92)90295-S.
53. Zafari, R.; Mendonça, F.G.; Tom Baker, R.; Fauteux-Lefebvre, C. Efficient SO2 Capture Using an Amine-Functionalized, Nanocrystalline Cellulose-Based Adsorbent. *Separation and Purification Technology* **2023**, *308*, 122917, doi:10.1016/j.seppur.2022.122917.
54. Gupta, N.K.; Kim, E.J.; Baek, S.; Bae, J.; Kim, K.S. Ternary Metal Oxide Nanocomposite for Room Temperature H2S and SO2 Gas Removal in Wet Conditions. *Sci Rep* **2022**, *12*, 15387, doi:10.1038/s41598-022-19800-6.
55. Babu, D.J.; Kühl, F.G.; Yadav, S.; Markert, D.; Bruns, M.; Hampe, M.J.; Schneider, J.J. Adsorption of Pure SO_2 on Nanoscaled Graphene Oxide. *RSC Adv.* **2016**, *6*, 36834–36839, doi:10.1039/C6RA07518E.
56. Muñiz, J.; Herrero, J.E.; Fuertes, A.B. Treatments to Enhance the SO2 Capture by Activated Carbon Fibres. *Applied Catalysis B: Environmental* **1998**, *18*, 171–179, doi:10.1016/S0926-3373(98)00039-3.
57. Li, B.; Zhang, Q.; Ma, C. Kinetics of SO2 Adsorption on Powder Activated Carbon in a Drop Tube Furnace. *International Journal of Chemical Engineering* **2021**, *2021*, 8886646, doi:10.1155/2021/8886646.
58. Wahlqvist, M.; Shchukarev, A. XPS Spectra and Electronic Structure of Group IA Sulfates. *Journal of Electron Spectroscopy and Related Phenomena* **2007**, *156–158*, 310–314, doi:10.1016/j.elspec.2006.11.032.
59. Lindberg, B.J.; Hamrin, K.; Johansson, G.; Gelius, U.; Fahlman, A.; Nordling, C.; Siegbahn, K. Molecular Spectroscopy by Means of ESCA II. Sulfur Compounds. Correlation of Electron Binding Energy with Structure. *Phys. Scr.* **1970**, *1*, 286, doi:10.1088/0031-8949/1/5-6/020.
60. Gelius, U.; Hedén, P.F.; Hedman, J.; Lindberg, B.J.; Manne, R.; Nordberg, R.; Nordling, C.; Siegbahn, K. Molecular Spectroscopy by Means of ESCA III. Carbon Compounds. *Phys. Scr.* **1970**, *2*, 70, doi:10.1088/0031-8949/2/1-2/014.

61. Jung, I.; Field, D.A.; Clark, N.J.; Zhu, Y.; Yang, D.; Piner, R.D.; Stankovich, S.; Dikin, D.A.; Geisler, H.; Ventrice, C.A.Jr.; et al. Reduction Kinetics of Graphene Oxide Determined by Electrical Transport Measurements and Temperature Programmed Desorption. *J. Phys. Chem. C* **2009**, *113*, 18480–18486, doi:10.1021/jp904396j.
62. Eigler, S.; Dotzer, C.; Hirsch, A.; Enzelberger, M.; Müller, P. Formation and Decomposition of CO2 Intercalated Graphene Oxide. *Chem. Mater.* **2012**, *24*, 1276–1282, doi:10.1021/cm203223z.

Chapter 3. Graphene oxide and iron oxide composites as catalysts for the oxidation of organic sulfides.

Abstract

The present work focuses on the development of a controlled and sustainable method for the preparation of graphene oxide-iron oxide composite and its application as a catalyst in the oxidation of sulfide. The nanoparticles were prepared from divalent and trivalent iron salts under basic pH in an aqueous reaction that produced a 2:1 mixture of Fe^{2+} and Fe^{3+} oxides identified as magnetite. Obtained nanocatalysts were immobilized over graphene oxide sheets to enhance their photocatalytic activity and light harvesting region and extend it to the visible range. Results confirmed the formation of iron oxides around 15 nm, homogeneously dispersed over graphene oxide layers. The application of the as-prepared catalysts resulted in effective thioanisole oxidation, achieving a 95% conversion in the presence of the catalyst and oxidizing agent. This oxidation process, and dimerization of sulfide compounds into heavy sulfones, indicates potential for use in wastewater treatment.

Keywords : sulfides, iron oxide, graphene oxide, catalyst, oxidation, photocatalytic activity

3.1. Introduction

The oxidation of organic sulfides is the most direct approach for producing sulfoxides and sulfones [1,2]. These compounds are essential synthetic intermediates in the synthesis of biologically active molecules, including high-value pharmaceuticals through asymmetric oxidation [1–3]. Sulfide oxidation is also utilized to produce large-scale solvents for metallurgy and improve the electronic properties of oligothiophene [1]. Another application is oxidative desulfurization, a process used to remove sulfur compounds from petroleum fuels [4–6]. This is important because sulfur in crude oil contributes to the corrosion of refining equipment, cause premature failures in combustion engines, and poisons catalysts in the refining industry [4]. Furthermore, these compounds contribute to the release of sulfur oxides (SO_x) into the atmosphere upon fuel combustion, resulting in acid rain formation and contributing to air pollution [4,7]. Additionally, the oxidation of sulfide compounds is effective in removing malodorous sulfur

compounds like dimethyl sulfoxide (DMSO) found in wastewater [8,9], addressing both environmental and public health concerns.

Given the importance of this reaction, numerous studies have aimed to enhance it. Strong oxidants like nitric acid, permanganate, or organic peracids (e.g., sulfonic acid) have been used, but require large amounts of oxidizing agents, produce significant liquid waste, and are not environmentally friendly [10]. Cheaper alternatives like molecular oxygen or hydrogen peroxide (H_2O_2) have also been explored. H_2O_2 is the most popular due to its accessibility, safety, and the fact that its only by-product is water [1,11]. Additionally, H_2O_2 has a good oxidation potential (E^0 = 1.77 V, [10]), and its oxidation reactions to sulfoxide can be more easily controlled compared to those using molecular oxygen or air [12].

To enhance the oxidation reaction with H_2O_2 at ambient conditions, both homogeneous and heterogeneous catalysts have been studied [10]. Various metal catalysts including Pt, Ru, Mn, Cu W have been studied for sulfide oxidation [13]. However, many of these catalysts require high amounts of the oxidizing agent, ranging from 1.1–8.0 equivalents relative to sulfide. Notably, catalytic systems based on Ti, V, and Fe have demonstrated high yields and selectivity for sulfoxides while using an equimolar amount of H_2O_2 [13]. Iron oxides, in particular, have emerged as environmentally friendly catalysts due to their low toxicity, abundance, and good catalytic activity that facilitate the utilization of mild reaction conditions [14,15].

Iron oxide-based materials are usually treated as superior heterogeneous Fenton catalysts [16,17], which is one of the most studied reactions for the oxidation and degradation/destruction of organic pollutants [15,18]. In Fenton reactions, hydrogen peroxide is typically used as an oxidant and reacts with Fe^{2+} to generate radical $OH\bullet$ (E^0=2.80 V), which is a highly reactive compound used to oxidize organic molecules [15,19]. However, it is difficult to regenerate the Fe^{2+} ion given the inherently slow $Fe^{3+}$to Fe^{2+} reduction kinetics [15,18]. Iron oxide can be used directly as a heterogenous catalyst or be incorporated into supporting materials like zeolites, metal-organic frameworks, and carbon materials [15,18], which prevents the leaching of the iron ions and increases their recyclability [15]. Incorporating carbon materials with heterogeneous Fenton catalysts helps in the quick reduction of Fe^{3+} to Fe^{2+} due to their fast single electron transfer ability [15,19,20]. Graphene is a two-dimensional monolayer of carbon atoms and exhibits superior electron mobility, mechanical stability, and electrical conductivity [15,19]. Recent reports indicate that both graphene oxide and iron oxide participate in the decomposition of H_2O_2 and the

generation of hydroxyl radicals [19,21]. Moreover, the active sites Fe^{2+} are constantly regenerated via the oxidation of the sp^2 domain which transfers electrons to the iron centers of Fe_3O_4 [21]. Additionally, the higher specific surface area and the several oxygen groups on its surface promote the adsorption of organic pollutants on the surface of GO [15,22].

It is proposed in this paper to use a facile co-precipitation method for the synthesis of iron oxide nanoparticles followed by a wet deposition on the surface of graphene oxide (GO) to produce GO-Fe_3O_4 as a catalyst in the oxidation of sulfide compounds. Thioanisole was used as a sulfide as it is a model aromatic thioether with widespread application as an intermediate in the production of dyes, pesticides, and pharmaceutical formulations [23]. The photocatalytic activity of the synthesized catalyst was also tested as it is known that certain iron oxides have the potential to act as photo-catalysts because of their semiconducting properties [15] and can produce radical $OH\bullet$ without the presence of H_2O_2.

3.2. Materials and methods

3.2.1. Reagents

Iron sulfate ($FeSO_4.7H_2O$, 99.0%) and iron chloride ($FeCl_3$, 97.0%) were purchased from Sigma Aldrich. Ammonium hydroxide, used for pH control and regulation was obtained from JT Baker. High surface area graphene oxide (GO) was purchased from ACS Materials (type B GO). As a solvent, deionized water (s=0.055 mS/cm @ 25 °C) was utilized in experimentation and HPLC grade Acetonitrile (CH_3CN), Ethanol, and Methanol (JT Baker) were utilized in identification analyses.

3.2.2. Instrumentation

Absorption and diffuse reflectance spectrophotometry analyses were performed in a HACH DR6000 UV Vis instrument (l=190-1100 nm) with a Labsphere integrating sphere accessory. Light scattering determinations were carried out in a Malvern Zeta Sizer Ultra, using DTS1070 cells. Atomic absorption was performed in an Agilent 240 FS AA instrument using a 90/10 acetylene/oxygen mixture (v/v). For Fourier Transform Infrared (FTIR) spectrometry: a Shimadzu IRTracer 100 with a QATR-10 accessory was used. High-performance liquid chromatography (HPLC) was performed using a Shimadzu Prominence 20 Series, DAD UV detector equipped with a 4.6x150 mm, f=5 mm (200 Å) Pursuit C-18 column. Gas chromatography-mass spectrometry

(GC-MS) analyses were done with an Agilent 7820A GC equipped with a 30m x 250µm x 0.25µm Agilent J&W column, He as carrier gas and coupled to single-quadrupole 5977C ESI+ MS detector. The developed method consisted of a low rate of 1mL/min with a heating ramp of 60°C x 1 min and an increase of 4°C/min until 160°C with a total runtime of 30 minutes. Transmission electronic microscopy (TEM) analyses were carried out in a JEOL 2010 TEM (200 kV) using a 200 mesh C-coated copper grid. For X-ray diffraction (XRD) a Bruker D8 Advance equipped with a CuKa (l=0.154 nm) X-ray source was used.

3.2.3. Synthesis of iron oxide nanoparticles

A 1:2 molar ratio of Fe^{2+} ($Fe_2SO4•7H_2O$) and Fe^{3+} ($FeCl_3$) ions were dissolved in 25 mL of deionized water containing 0.06 M of sucrose (sugar table) as surfactant [24]. The solution was heated to 80°C and the oxidation took place by the addition of a 32 wt% ammonium hydroxide solution. The hydroxide solution was added dropwise until a pH of 9 was reached, resulting in the formation of a brown-to-black suspension indicative of the formation of magnetite nanoparticles [25,26]. The effect of citric acid and sucrose as stabilizing agents was respectively studied as shown in Table 3.1. When synthesizing with sucrose, 0.06 M of sucrose granules were dissolved in water before the addition of the precursors and the reaction proceeded as described above. When using citric acid, the reaction was conducted as described above, without sucrose and the required amount of citric acid to decrease the pH from 9 to 7-8 was added to the solution. This was used as a neutralization solution to drop the pH and allow the introduction of stabilizers to attach to the particle surface and de-agglomerate the particles formed during precipitation [27].

Table 3.1: Iron oxide nanoparticles co-precipitation synthesis under different reaction conditions.

Sample	$[Fe^{2+}]$	$[Fe^{3+}]$	Sucrose (Scr)	Citric acid (CA)	Ammonia	System Volume	Final pH
	mol/L				µL	mL	
S1	0.01	0.02	-	-	600	25.6	9
S2	0.01	0.02	0.06	-	600	25.6	9
S3	0.01	0.02	-	0.014	600	26.8	8
S4	0.01	0.02	0.06	0.014	600	26.8	7

3.2.4. Wet deposition of nanoparticles on graphene oxide

200 mg of GO was dispersed in 50 mL of deionized water and 1.8 mL of the nanoparticles suspension was added to have 1.4 wt% iron deposition on the surface of GO. The mixture was agitated for 48-72 hours to ensure proper deposition. The mixture was then centrifuged, dried at 60°C for 2 hours, and ground to obtain a black powder of the catalyst iron oxide-supported GO (GO-Fe_3O_4).

3.2.5. Oxidation of thioanisole

A concentrated solution of thioanisole solution was diluted in 25 mL of deionized water to achieve a concentration of 0.3 g/L. The solution was stirred and heated to 50°C, then 30 mg of the synthesized catalyst was added to the solution (1:4 substrate-to-catalyst ratio) followed by the addition of hydrogen peroxide as an oxidizing agent. The effect of hydrogen peroxide was studied by varying its concentration from a reaction without H_2O_2 to low and high H_2O_2 as presented in Table 3.2. To study the light source effect, room illumination, visible LED, UV, and sunlight irradiation tests were performed (Table 3.2). All the reactions were carried out at 50°C for 180 min with samples collected every 30 minutes for HPLC analysis to study the kinetics of the reaction. The samples for HPLC were prepared by removing the leftover catalyst using a 16000 rpm/5-minute centrifugation. The detection of thioanisole was done at 250 nm, a mixture of H_2O:ACN:MIBK:formic acid (50:25:24:01 v/v ratio) was used as the eluent and the runtime was 15 min. To determine the effect of GO-Fe_3O_4 and H_2O_2 over reaction products, GC-MS analyses were carried out upon reaction of thioanisole (0.3 g/L) with dispersed GO-Fe_3O_4 (1:4 substrate-to-catalyst ratio) and in the presence (0.32 g/L) or absence of hydrogen peroxide.

Table 3.2: Reaction conditions for oxidation of Thioanisole by GO-Fe_3O_4 catalyst.

Treatment	Blank	Cat. Control	UV Control	No H_2O_2	Low H_2O_2	High H_2O_2	UV	Sun	Visible
[Thioanisole] (g/L)	0.3	0.3	0.3	0.3	0.3	0.3	0.3	0.3	0.3
[H_2O_2] (g/L)	-	0.16	-	-	0.16	0.32	-	-	-
Thioanisole: H_2O_2 (molar ratio)	1:0	1:2	1:0	1:0	1:2	1:4	1:0	1:0	1:0
[GO- Fe_3O_4 Catalyst] (mg)	-	-	-	30	30	30	30	30	30
Thioanisole: Catalyst (mass ratio)	1:0	1:0	1:0	1:4	1:4	1:4	1:4	1:4	1:4
Irradiation intensity (klux)	2.9	2.9	1.5	2.9	2.9	2.9	1.5	115.0	4.5
Light source	Room	Room	365 nm lamp	Room	Room	Room	365 nm lamp	19°03'17"-98°12'10"*	560 nm LED

*Geographic coordinates of Puebla, Mexico, where were conducted the reactions.

3.3. Results and discussion

3.3.1. Aqueous synthesis of iron oxide nanoparticles

Iron oxide nanoparticles were prepared by the controlled oxidation of soluble iron (II) and (III) salts to form non-soluble Fe_3O_4 crystals along with soluble ammonium chloride and soluble ammonium sulfate. This aqueous co-precipitation method (Equation 3.1) has been previously reported and is a common method for the preparation of magnetite and substituted ferrites [28–30]:

$$2FeCl_3 + FeSO_4 + 4H_2O + 8NH_4OH \rightarrow Fe_3O_4 + 6NH_4Cl_3 + (NH_4)_2SO_4 + 8H_2O \quad (3.1)$$

Under this method, magnetite is the main product. However, incomplete, side and reversible reactions occurring on the light-sensitive Fe_3O_4 surface in aqueous systems will tend to oxidize Fe^{2+} ions in ferrites to form iron (III) oxides with varying compositions and ratios [31]. Additionally, magnetite nanoparticles tend to agglomerate due to strong magnetic dipole-dipole attraction, their Van der Waals interactions, and high surface energy [32]. To prevent their agglomeration and oxidation, surfactants such as polyols, sucrose, and citric acid are typically used [33,34]. Citric acid (CA) is a common surfactant used to stabilize iron oxide nanoparticles [27,35–37] and sucrose (Scr) is a green alternative given its functionality and availability [32,34,38]. To evaluate the convenience in the utilization of surfactant and pH storage conditions, a set of

experiments was designed as presented in Table 3.1 to determine optimum reaction conditions and the stability of the iron oxide-based product.

The Fe^{2+} and Fe^{3+} content of iron oxide nanoparticles 28 days after the synthesis was determined using spectral lines at 248 nm (Fe^{2+}) and 372 nm (Fe^{3+}) through atomic absorption as shown in Figure 3.1. A calibration curve with a known concentration of each ion was performed (see Figure A.4 in the appendices).

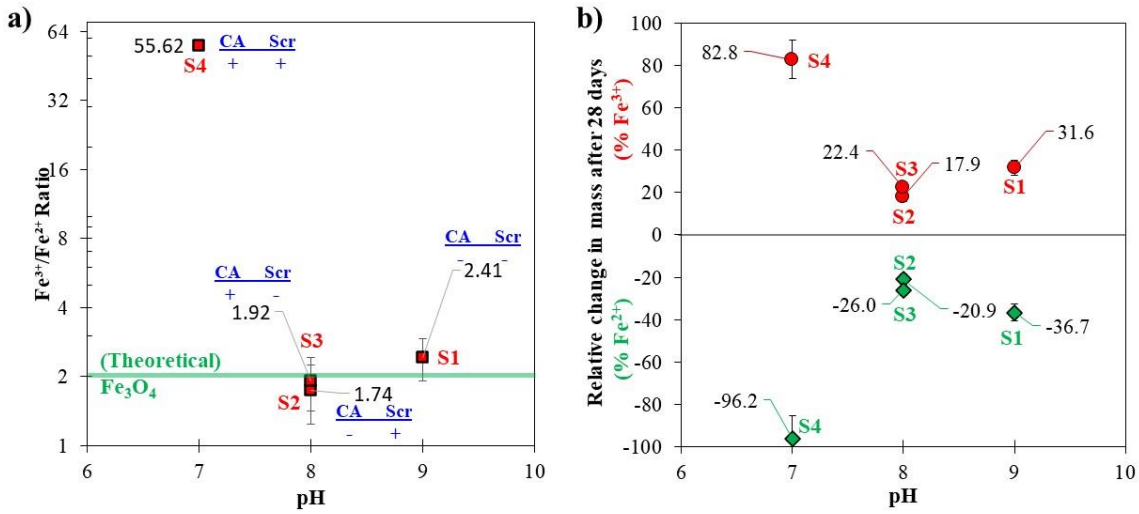

Figure 3.1: (a) Fe^{3+} and Fe^{2+} content of synthesized iron oxides with different combinations of CA and Scr; (b) Relative changes in Fe^{3+} and Fe^{2+} in iron oxides after 28 days of storage as aqueous suspensions.

Fe_3O_4 has a theoretical Fe^{2+}/Fe^{3+} ratio of 1:2 and it was observed in Figure 3.1a that synthesis carried out without surfactants or using either sucrose or citric acid led to similar ratios even after 28 days (respectively, S1=1:2.41, S2=1:1.74, and S3=1:1.92). On the other hand, using both surfactants together (CA+ and Scr+) increases the concentration of Fe^{3+} (S4=1:55.62). The change in mass was compared to the initial mass of iron used for the synthesis. After 28 days of storage in aqueous dispersion, a trend towards Fe^{3+} was observed in all cases (Figure 3.1b). Of all combinations, the system containing sucrose (S2) showed the least Fe^{3+} mass increase (17.9%) followed by S3, containing only CA (22.4%). When Fe_3O_4 was synthesized in the absence of surfactants (S1), Fe^{3+} increased by 31.6% in terms of relative mass. Even though surfactants are not mandatory in magnetite synthesis (S1), it can be inferred that CA and Scr as surfactants stabilize iron oxides freshly created during the co-precipitation process. When both surfactants are

used, preserving activity ceases, and gradual oxidation of magnetite towards Fe^{3+} oxides is clear. This behavior can be explained based on the capacity of citric acid to act as an interlinker in the formation of oligomers made of hexoses and disaccharides as sucrose [39,40]. At high temperatures, these molecules form ester-based chains and in some cases could yield to the formation of furans [41]. As oxygen-based groups are occupied by esterification and organic H bonds, there are few sites for Fe-O interactions which hinders the capping and surfactant capabilities of CA and Scr.

Magnetite iron composition is not stable and tends to decay to Fe^{3+}-rich compounds. The most common product of the oxidation of magnetite is maghemite (Fe_2O_3) [42]. Schwaminger et al. demonstrated that magnetite nanoparticles subjected to a temperature of 60°C and agitated in an air environment for 24 hours resulted in a complete oxidation of ferrous ions to ferric ions [43]. They elucidate the oxidation process of magnetite, highlighting that ferrous iron ions undergo oxidation before the structural changes into maghemite. The oxidation initiates at the surface of the nanoparticle, progressing inward to the core [43]. Additionally, it is established that divalent iron ions located on tetrahedral sites on the surface of magnetite nanoparticles are prone to rapid oxidation under ambient conditions due to direct contact with H_2O and air [44,45]. Nevertheless, this oxidation process can be mitigated or delayed by coating the nanoparticles with either organic or inorganic molecules during the precipitation process [30]. Such coating forms a protective layer around the nanoparticles, thereby impeding the oxidation process [30,46]. Consequently, nanoparticles synthesized with surfactants (S2 and S3) exhibit a lesser increase in Fe^{3+} mass, indicating the efficacity of this approach. Given its cost-effectiveness and availability, sucrose appears to be the most attractive option. As a result, sample S2, nanoparticles coated with sucrose, was selected for the subsequent stages of GO-Fe_3O_4 catalyst synthesis.

3.3.2. Wet deposition of nanoparticles on graphene oxide

The nanoparticles prepared using sucrose (S2), being the most stable among the produced nanoparticles, were subsequently utilized to prepare GO-Fe_3O_4. Electron microscopy confirmed the deposition of iron oxide nanoparticles over the surface of graphene oxide sheets. GO-Fe_3O_4 catalyst is composed of large sheets of graphene oxide with small dense particles associated with metal oxides that are homogeneously distributed over the carbon surface (Figure 3.2a). Closer observations reveal that these dense particles are agglomerations of smaller units with individual

units measuring approximately 15 nm in diameter and overall cluster sizes ranging from 50 to 150 nm (Figure 3.2b). The primary crystal planes were identified using the Joint Committee on Powder Diffraction Standards (JCPDS) cards 19-0629 and 11-614 for magnetite and 39-1346 for g-Fe_2O_3. High-resolution transmission electron microscopy (HRTEM) in Figure 3.2c, allowed us to observe single oxide particles and determine their crystalline properties. It is possible to observe that the predominant orientation has 2.8 Å spacing which corresponds to the [220] facet of magnetite [47]. It is also very clear to observe a periodic pattern with 4.9 Å spacing that corresponds to [111] facet of spinel ferrites [25,47]. Single Area Electron Diffraction (SAED) patterns presented in Figure 3.2d allowed us to further identify [222] and [440] facets with distances of 2.42 and 1.48 Å [25,47]. This confirms that the metal oxide particles over the GO surface are cubic spinel iron ferrites associated with Fe_3O_4. The X-ray diffraction pattern presented in Figure 3.2e corresponds to iron oxide prepared by co-precipitation and shows the typical pattern of cubic spinel magnetite with its characteristic signals at 30.65° [220]; 35.8° [311]; 43.52° [400]; 54.12° [422]; 57.51° [511] and 63.13° [440] [25,47–49]. From Scherrer Debye equation it was possible to determine crystallite size to be 10.90 nm which is in close resemblance to electron microscopy images. For the GO-Fe_3O_4 catalyst, it was still possible to observe the peaks of magnetite and a new peak emerged at 44.54°, associated with 100 facets of graphene oxide [50,51].

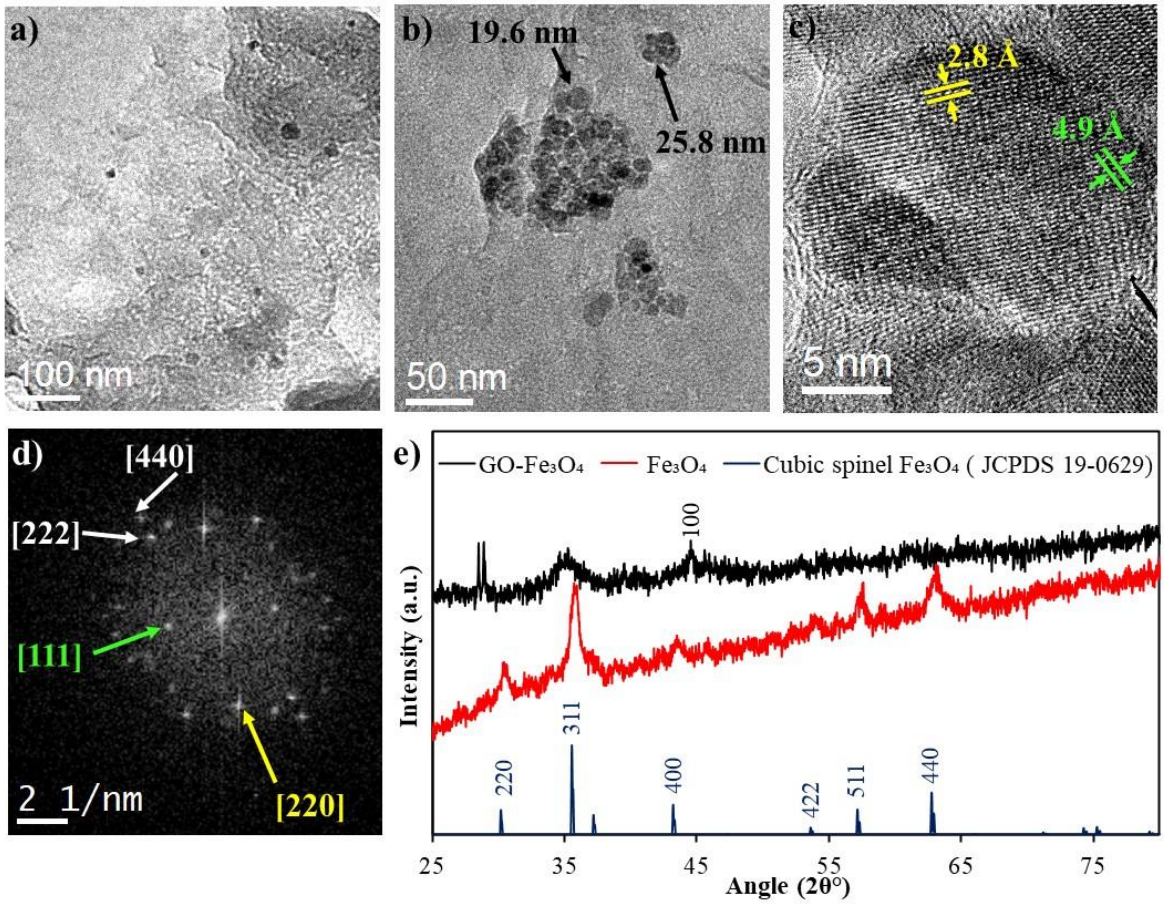

Figure 3.2: Morphology characterization of GO-Fe_3O_4 catalyst with nanoparticles from sample S2. (a) low magnification for general GO-Fe_3O_4 morphology; (b) high magnification of Fe_3O_4 particles over GO surface; (c) HR-TEM micrography showing principal lattice arrangements; (d) SAED pattern with identified Fe_3O_4 planes; (e) X-Ray diffractogram for bare Fe_3O_4 oxides and final GO-Fe_3O_4 catalysts.

FTIR analyses of the GO and GO-Fe_3O_4 presented in Figure 3.3a confirm the presence of organic and inorganic materials corresponding to GO and iron oxides. The broad peak appearing at 3500 cm^{-1}, attributed to the O-H bond, reveals the presence of hydroxyl groups in graphene oxide. The band observed at 1705 cm^{-1} was assigned to the carboxylic group (C=O stretching). The peaks found at 1611, 1222, and 1036 cm^{-1} were due respectively to aromatic C=C stretching, C-O-C stretching (epoxy group), and the vibrational mode of the alkoxy C-O group [52,53]. The presence of iron oxide on GO-Fe_3O_4 is confirmed by the peak found at 458 cm^{-1} associated with the vibrational mode of metal-oxygen bonds in the crystalline lattice of Fe_3O_4 [38,39]. However,

the addition of iron on the GO surface led to the loss of O-H, and C=O bonds. Peaks in the region 2158 - 2000 cm^{-1} suggest the presence of CO_2 intercalated between the GO layers which can be attributed to the 60°C drying step required to produce GO-Fe_3O_4 catalyst powder. According to research conducted by Siegfried et al., the formation of CO_2 starts at 50°C and progresses up to 120°C during thermal annealing of GO at 50°C to 150°C [56]. This formation results from the removal of carbon from the basal plane or edge, leading to defects in the carbon sheet structure [56,57].

The zeta potential curves in Figure 3.3b show a negative charge on the surface of the graphene oxide and the intensity increases with the addition of iron oxide without changing the zeta potential value. The UV-vis spectrum in Figure 3.3c reveals a peak around 300 nm corresponding to the n-π* transitions of the C=O bonds present in graphene oxide [53]. The peak around 260 nm for the GO-Fe_3O_4 material indicates the presence of iron oxide nanoparticles [58]. Figure 3.3c also indicates that the samples are more responsive in the ultraviolet region. The direct band gap energy (E_g) in Figure 3.3d was obtained using the Tauc's equation [59]:

$$(\alpha h\upsilon)^2 = k\left(h\upsilon - E_g\right) \tag{3.2}$$

where α is the absorbance coefficient, h the Planck's constant, hυ the incident photon energy, and k is the constant associated with the material. By plotting $(\alpha h\upsilon)^2$ as a function of hυ (Figure 3.3d) and extrapolation of the linear portion of the curve, E_g is the x value when $(\alpha h\upsilon)^2 = 0$. The E_g of GO-Fe_3O_4 was lower than that of pristine GO (2.24 eV and 3.23 eV respectively) indicating that the deposition of iron oxide nanoparticles on the GO surface increases the conductivity of the material.

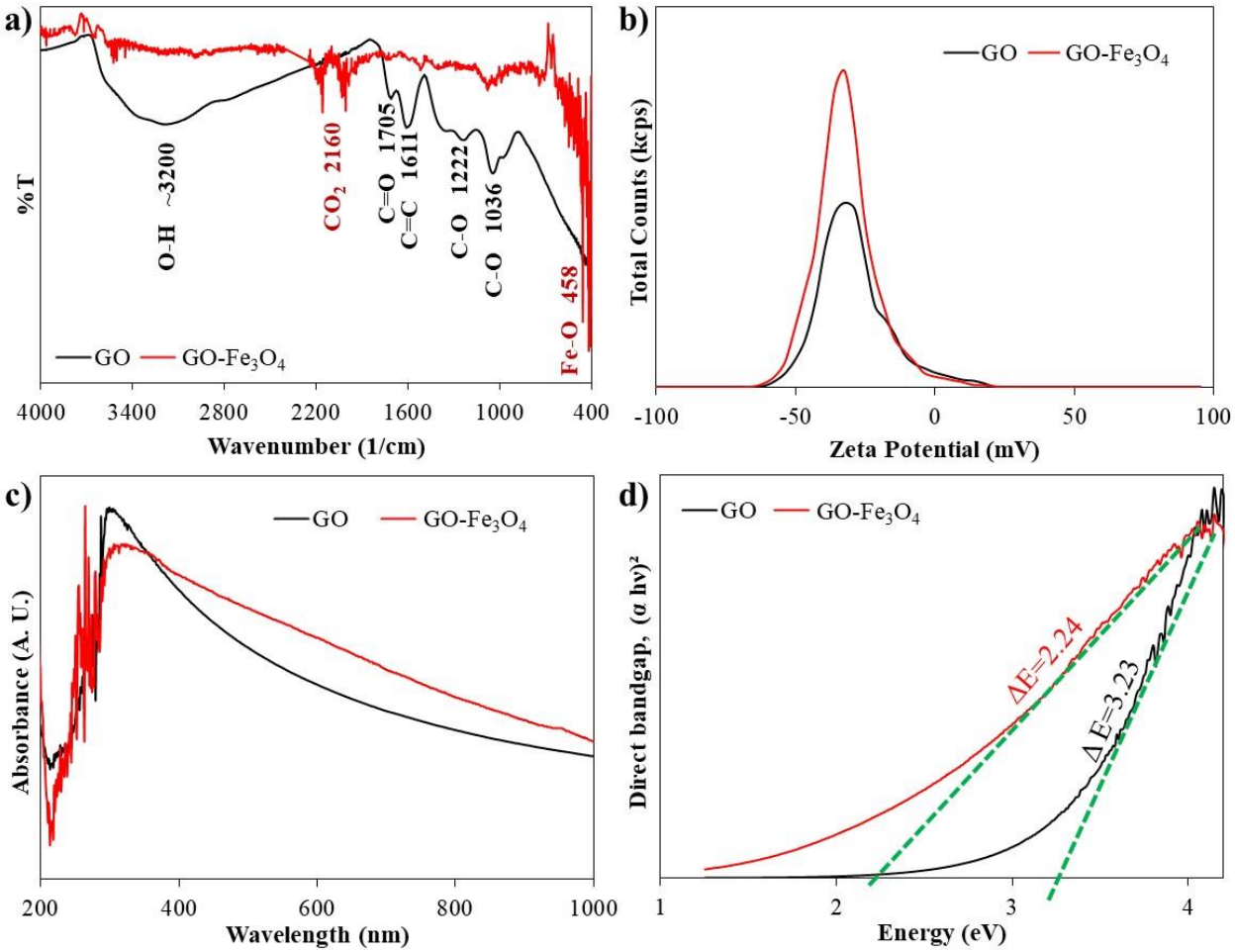

Figure 3.3: Characterization of GO and GO-Fe_3O_4 catalyst containing nanoparticles from sample S2: (a) FTIR; (b) Zeta potential; (c) UV-Vis spectrum; (d) Direct bandgap determination through Tauc's method.

3.3.3. Oxidation reaction with thioanisole

The catalytic properties of the synthesized GO-Fe_3O_4 catalyst were investigated under different oxidizing and light irradiation conditions as shown in Table 3.2. The conversion of thioanisole was monitored using HPLC as explained in section 2.5 and the results are presented in Figures 3.4a and b. The changes in thioanisole concentration for each reaction were calculated using a calibration curve showing the area under the thioanisole absorption peak at 250 nm as a function of the thioanisole concentrations (Figure A.5 in the appendices). The retention time (T_r) was found to be between 5 and 7 min. The control experiments, the reaction without the oxidizing

agent and catalyst (Blank) and the reaction containing only the oxidizing agent (Cat. control), have low thioanisole conversion (up to 8%) confirming the need for a catalyst for the reaction [60]. Conversely, in the presence of only the catalyst (no H_2O_2), a conversion of 64.2% of thioanisole was observed indicating the catalytic activity of the synthesized GO-Fe_3O_4 material. The addition of H_2O_2 increases the conversion from 64.2% to 92.8%. A possible explanation is that the addition of H_2O_2 leads to the formation of radical species, namely, hydroxyl radicals through Fenton chemistry [15,21,61] presented in Equation 3.3. The produced hydroxide radical then oxidized the sulfide compounds. The increase of the substrate: H_2O_2 molar ratio from 1:2 (Low H_2O_2) to 1:4 (High H_2O_2) did not show a significant increase in the conversion of thioanisole (going from 92.8% to 95.8%), indicating only a slight dependence on H_2O_2 concentration at these levels.

$$Fe^{2+} + H_2O_2 \rightarrow Fe^{3+} + OH\bullet + OH^- \quad (3.3)$$

The photocatalytic activity of the synthesized GO-Fe_3O_4 catalyst was studied as well. Figure 3.4b shows thioanisole concentration changes during reactions without H_2O_2 under visible light, room light, UV light, or sunlight irradiation. Thioanisole conversion under UV light was 89.6%, 77.7% under sunlight, 75.2% under visible light, and 64.2% under room light (no H_2O_2 condition in Table 3.2), indicating the photocatalytic property of the synthesized catalyst (see Table 3.3). This activity involves the absorption of a light photon of energy greater than or equal to the photocatalyst's band gap, exciting electrons from the valence band to the conduction band and generating charge carriers [62,63]. The excited electrons react with the available oxygen (O_2) molecules to form superoxide anion ($O_2^{\bullet -}$) radicals [62], while the holes in the valence band react with water to produce hydroxyl radicals ($OH\bullet$). $O_2^{\bullet -}$ further react with H_2O to produce hydrogen peroxide (H_2O_2), which decomposes into $OH\bullet$ in presence of light [62]. The produced radicals are highly oxidative [62,64].

The UV light irradiation without H_2O_2 showed the highest thioanisole conversion with 89.6%, closer to the conversion obtained when using the catalyst and H_2O_2 (92.8%). The bandgap energy, being the minimum energy required to excite an electron from the valance band to the conductive band, determined the energy a photon must have to activate the photocatalyst [62,63]. UV light photons, with energy ranging from 3.1 to 12.0 eV [65] exceed those of visible light photons, which range from 2.00 to 2.75 eV [66]. Given the catalyst's bandgap energy of 2.24 eV, the higher conversion under UV light is explained. Moreover, the conversion of thioanisole under visible

light (75.2%) and sunlight (77.7%) indicates that the material could potentially be optimized to function effectively under low light energy. However, it is important to note that the reaction temperature was maintained at 50°C when using different light sources. Additional experiments without supplemental heat are therefore necessary to fully evaluate the photocatalytic efficiency of the material.

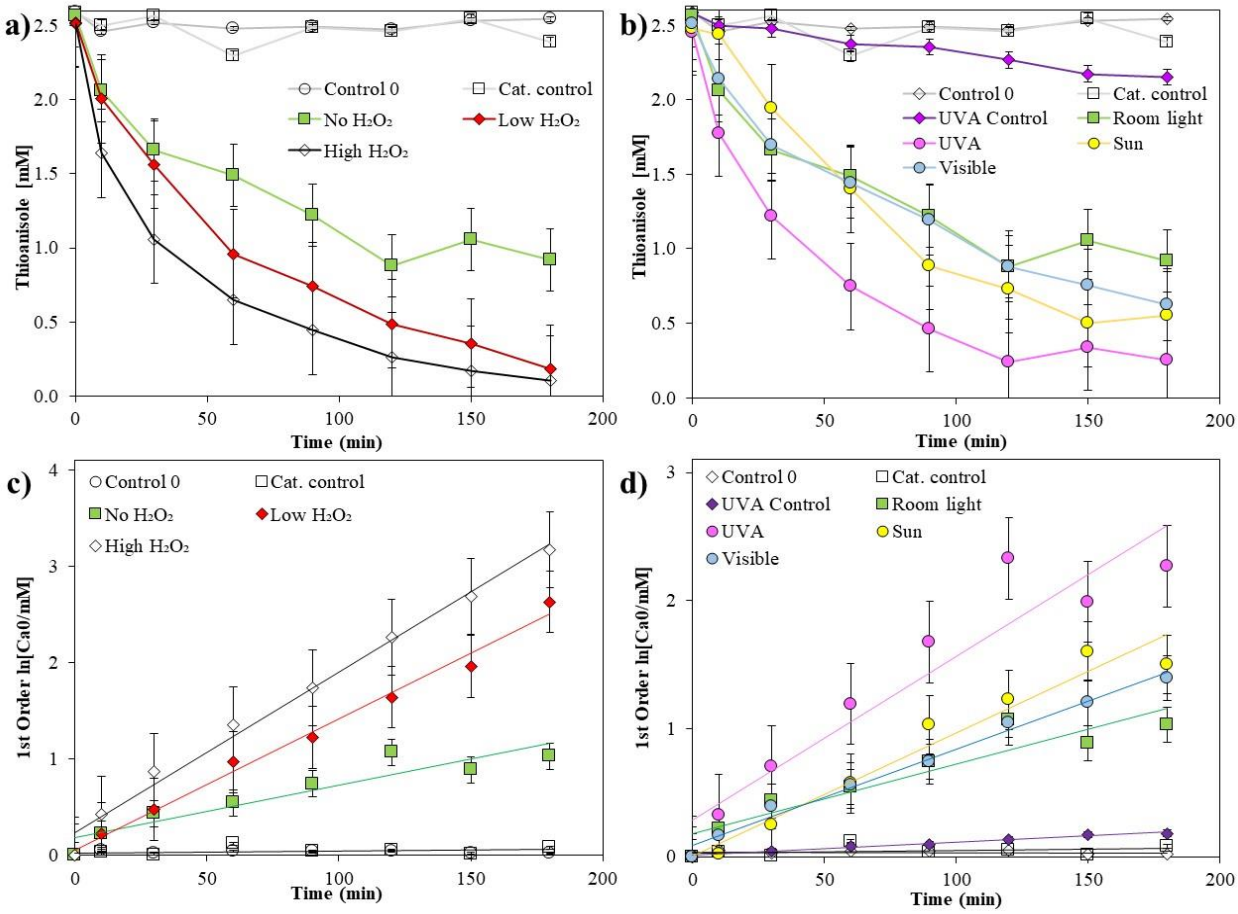

Figure 3.4: Changes in thioanisole concentration as a function of time and kinetic studies under different catalytic treatments. All the reactions were done at 50°C for 3 hours and GO-Fe_3O_4 catalyst containing nanoparticles from sample S2 was used in a ratio of 4:1 to the substrate. Blank: -catalyst-H_2O_2; Cat. control: -catalyst+H_2O_2; the substrate to oxidizing agent molar ratio for low and high H_2O_2 are 1:2 and 1:4. UV control: -catalyst-H_2O_2+UV light (365 nm lamp); reactions under UV light, Sunlight (19°03'17"-98°12'10"), visible (560 nm LED) and room light (no H_2O_2 and no particular irradiation) were done in the absence of H_2O_2. (a) presents the effect of catalyst and H_2O_2 over thioanisole conversion; (b) is the effect of light irradiation over thioanisole conversion; (c) and (d) presents the first-order kinetics of the reactions.

The catalytic activity of the synthesized catalyst was analyzed using the first-order kinetic model theory expressed by Equation (3.4) [67]:

$$\ln(C_0/C_t) = -kt \tag{3.4}$$

Where k is the rate constant of thioanisole consumption, C_0 and C_t are the concentrations of thioanisole at times $t = 0$ and $t = t$ minutes, respectively. Figures 3.4d and c show the plots of ln (C_0/C_t) versus time. The rate constants k of each reaction are presented in Table 3.3. As expected, the GO-Fe_3O_4 catalyst with high H_2O_2 had the highest rate of conversion (0.017 min^{-1}), followed by GO-Fe_3O_4 without H_2O_2 under UV light irradiation (0.013 min^{-1}). These results indicate promising photocatalytic activity of the material under UV light, and further optimization of the material could enhance its performance. For instance, studies by Adrian Radoń et al. [59] and Mamotaj Khatun et al. [62] demonstrated that increasing the particle size of Fe_3O_4 and nickel stannate ($NiSnO_3$) nanomaterials leads to a decrease in the energy band gap which improves the catalyst's efficiency.

Table 3.3: Rate of thioanisole oxidation and conversion percentage under various oxidation treatments with GO-Fe_3O_4 catalyst at 50°C. Low and high H_2O_2 conditions correspond respectively to molar ratios of 1:2 and 1:4 for substrate: H_2O_2. Reactions under UV light (365 nm), Sunlight (19°03'17"-98°12'10"), and visible light (560 nm LED) were conducted without H_2O_2.

	Blank	Cat. Control	UV Control	No H_2O_2	Low H_2O_2	High H_2O_2	UV	Sun	Visible
Rate constant k (1/min)	-	0.0002	0.001	0.005	0.014	0.017	0.013	0.009	0.0075
Conversion of thioanisole (%)	-	7.6	16.7	64.2	92.8	95.8	89.6	77.7	75.2

Product analysis by gas chromatography coupled with mass spectrometry (GC-MS) was carried out to identify the effect of H_2O_2 as a reactive oxygen species (ROS) primary source (Figure 3.5). Thioanisole was identified at T_r=18.7 min with its distinctive m/z=124 ($C_7H_8S^+$). In the case of treatment with H_2O_2 (+ GO-Fe_3O_4 + H_2O_2), only one main adduct, identified as Product A (P_A) was observed at T_r=11.8 min with m/z=266 [M^+] and $C_{12}H_{10}O_3S_2^+$ formula. This compound is identified as phenyl benzene sulfinyl sulfone, a sulfone-sulfoxide dimer that confirms the oxidation

of thioanisole, and similar structures have been previously reported [68,69]. In the case of oxidation with GO-Fe_3O_4 with no H_2O_2, two main products were observed: P_A (T_r=11.7 min m/z=266 [M^+], $C_{12}H_{10}O_3S_2^+$), and a secondary product (P_B) at T_r=11.1 min with m/z=282 associated to $C_{12}H_{10}O_4S_2^+$ (phenyl disulfone) formula, which was not observed in H_2O_2-driven reaction. Reactions in the absence of H_2O_2 typically show lower reaction rates [70] and the milder conditions present in H_2O_2-free environments allow secondary pathways to produce additional adducts that are not typically observed in highly oxidant environments [71,72].

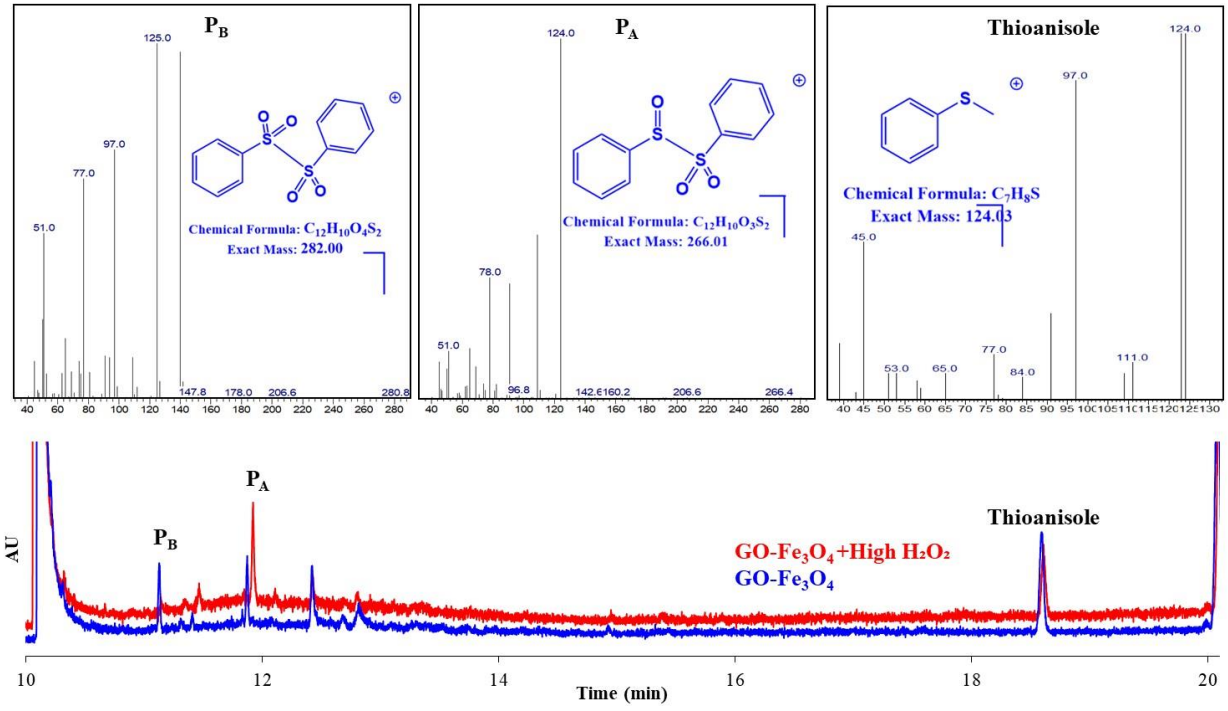

Figure 3.5: GC-MS identification of major adducts upon oxidation of thioanisole by GO-Fe_3O_4 catalyst containing nanoparticles from sample S2. High H_2O_2 indicates a molar ratio of 1:4 of substrate to H_2O_2. The reactions were conducted at 50°C under room light.

The full FTIR spectra of fresh thioanisole and its oxidation products in the presence or absence of H_2O_2 are presented in Figure 3.6a. For a closer analysis of functional groups, different regions were identified and labeled as R_1 (Aromatic stretches); R_2 (Fingerprint region) and R_3 (far IR). In all cases, it was possible to identify typical features of aromatic C=C-H bonds at ~2970 cm^{-1}. At 3020 cm^{-1}, the thioether (R-S-R') signal is clear for thioanisole but, this signal fades upon oxidation treatment. The formation of S-H thiol groups was discarded as its distinctive signal at 2550 cm^{-1}

was not present in any reactions [73]. This confirms that the oxidation of thioanisole takes place at aliphatic groups and does not cleavage the benzenic ring (Figure 3.6b) as reported before [74]. The fingerprint region (1300 to 1000 cm^{-1}) showed the presence of R-S-R' skeletal vibrations at 1090 cm^{-1} in the case of thioanisole and the reaction without H_2O_2 (Figure 3.6c); however, this signal was not noticeable when H_2O_2 was present. Signals at 1290 cm^{-1} and 1050 cm^{-1} associated with sulfones and sulfoxides respectively, are present in GO-Fe_3O_4 but are not noticeable when H_2O_2 is present. In the R_3 region (between 650-800 nm) the peak at 680 cm^{-1} is associated with disulfide bonds that were observed after any of the catalytic treatments [75]; the evidence suggests an oxidation consisting of dimerization through the formation of oxidized S-S bonds.

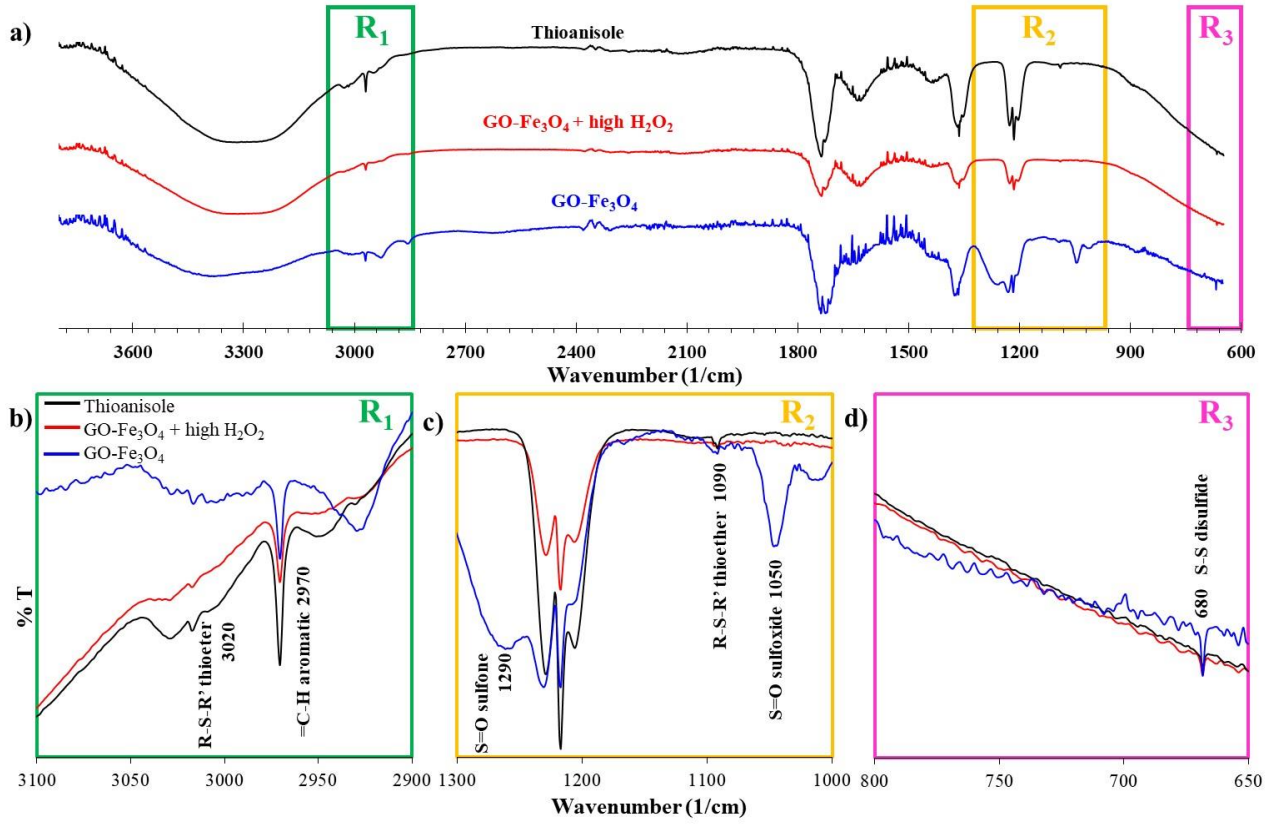

Figure 3.6: FTIR analyses of the oxidation products of thioanisole oxidation by GO-Fe_3O_4 (with S2 nanoparticles) at 50°C under room light. H_2O_2 indicates a molar ratio of 1:4 of the substrate to H_2O_2. (a) Full spectra; (b) Aromatic region (2900-3100 cm^{-1}); (c) Fingerprint region (1000-1300 cm^{-1}) and (d) Far IR (650-800 cm^{-1}).

3.4. Conclusions

In this study, Fe_3O_4 nanoparticles have been synthesized by co-precipitation. The presence of surfactant, particularly sucrose, did improve the stability of the nanoparticle. GO-Fe_3O_4 nanocomposite was prepared through wet deposition of the nanoparticles containing sucrose and the TEM, XRD, and FTIR confirmed the deposition of nanoparticles on the GO surface. TEM analysis revealed round-shaped nanoparticles of 15 nm on the GO surface and the HRTEM, and SAED analyses identified the nanoparticles as Fe_3O_4.

The prepared nanocomposite showed catalytic activity during the oxidation of thioanisole at 50°C independently of the presence of the oxidizing agent, H_2O_2. However, the rate of the thioanisole conversion increased in the presence of H_2O_2, going from 0.005 min^{-1} to 0.014 min^{-1}, highlighting the role of H_2O_2 as an oxidizing agent. The main product of the oxidation of thioanisole in the presence of GO-Fe_3O_4 and H_2O_2 was phenyl benzene sulfinyl sulfone, a sulfone-sulfoxide dimer. This indicates that the oxidation of thioanisole is achievable with this catalyst and under these conditions, although the reaction lacks selectivity.

The optical band gap value of 2.24 eV indicated the semiconductive nature of the synthesized GO-Fe_3O_4 material and the possibility of being activated under visible light. The photocatalytic activity of the GO-Fe_3O_4 catalyst was evaluated at 50°C without H_2O_2 under various light sources, resulting in conversion percentages of 89.6% under UV light, 77.7% under sunlight, 75.2% under visible light, and 64.2% under room light. These results suggest the potential for using the GO-Fe_3O_4 catalyst under low-energy light sources. However, the material should be further optimized and tested at room temperature for a more comprehensive evaluation.

Reference

1. Tumula, V.R.; Bondwal, S.; Bisht, P.; Pendem, C.; Kumar, J. Oxidation of Sulfides to Sulfones with Hydrogen Peroxide in the Presence of Acetic Acid and Amberlyst 15. *Reac Kinet Mech Cat* **2012**, *107*, 449–466, doi:10.1007/s11144-012-0491-8.
2. Browne, W.R.; de Boer, J.W.; Pijper, D.; Brinksma, J.; Hage, R.; Feringa, B.L. Manganese-Catalyzed Oxidation with Hydrogen Peroxide. In *Modern Oxidation Methods*; John Wiley & Sons, Ltd, 2010; pp. 371–419 ISBN 978-3-527-63203-9.
3. Fernández, I.; Khiar, N. Recent Developments in the Synthesis and Utilization of Chiral Sulfoxides. *Chem. Rev.* **2003**, *103*, 3651–3706, doi:10.1021/cr990372u.
4. Trehoux, A.; Roux, Y.; Guillot, R.; Mahy, J.-P.; Avenier, F. Catalytic Oxidation of Dibenzothiophene and Thioanisole by a Diiron(III) Complex and Hydrogen Peroxide. *Journal of Molecular Catalysis A: Chemical* **2015**, *396*, 40–46, doi:10.1016/j.molcata.2014.09.030.
5. Hulea, V.; Fajula, F.; Bousquet, J. Mild Oxidation with H2O2 over Ti-Containing Molecular Sieves—A Very Efficient Method for Removing Aromatic Sulfur Compounds from Fuels. *Journal of Catalysis* **2001**, *198*, 179–186, doi:10.1006/jcat.2000.3149.
6. Campos-Martin, J. m.; Capel-Sanchez, M. c.; Perez-Presas, P.; Fierro, J. l. g. Oxidative Processes of Desulfurization of Liquid Fuels. *Journal of Chemical Technology & Biotechnology* **2010**, *85*, 879–890, doi:10.1002/jctb.2371.
7. Effects of Acid Rain Available online: https://www.epa.gov/acidrain/effects-acid-rain.
8. Maciuca, A.-L.; Dumitriu, E.; Fajula, F.; Hulea, V. Catalytic Oxidation Processes for Removing Dimethylsulfoxide from Wastewater. *Chemosphere* **2007**, *68*, 227–233, doi:10.1016/j.chemosphere.2007.01.028.
9. Cojocariu, A.M.; Mutin, P.H.; Dumitriu, E.; Vioux, A.; Fajula, F.; Hulea, V. Removal of Dimethylsulfoxide from Wastewater Using Mild Oxidation with H2O2 over Ti-Based Catalysts. *Chemosphere* **2009**, *77*, 1065–1068, doi:10.1016/j.chemosphere.2009.08.059.
10. Hulea, V.; Dumitriu, E.; Fajula, F. Mild Oxidation of Organosulfur Compounds with H2O2 over Metal-Containing Microporous and Mesoporous Catalysts. *Catalysts* **2021**, *11*, 867, doi:10.3390/catal11070867.
11. Sato, K.; Hyodo, M.; Aoki, M.; Zheng, X.-Q.; Noyori, R. Oxidation of Sulfides to Sulfoxides and Sulfones with 30% Hydrogen Peroxide under Organic Solvent- and Halogen-Free Conditions. *Tetrahedron* **2001**, *57*, 2469–2476, doi:10.1016/S0040-4020(01)00068-0.
12. Bayat, A.; Shakourian-Fard, M.; Ehyaei, N.; Mahmoodi Hashemi, M. A Magnetic Supported Iron Complex for Selective Oxidation of Sulfides to Sulfoxides Using 30% Hydrogen Peroxide at Room Temperature. *RSC Advances* **2014**, *4*, 44274–44281, doi:10.1039/C4RA07356H.
13. Kamata, K.; Hirano, T.; Mizuno, N. Highly Efficient Oxidation of Sulfides with Hydrogen Peroxide Catalyzed by [SeO4{WO(O2)2}2]2−. *Chem. Commun.* **2009**, 3958–3960, doi:10.1039/B907952A.
14. Rajabi, F.; Kakeshpour, T.; Saidi, M.R. Supported Iron Oxide Nanoparticles: Recoverable and Efficient Catalyst for Oxidative S-S Coupling of Thiols to Disulfides. *Catalysis Communications* **2013**, *40*, 13–17, doi:10.1016/j.catcom.2013.05.017.
15. Thomas, N.; Dionysiou, D.D.; Pillai, S.C. Heterogeneous Fenton Catalysts: A Review of Recent Advances. *J Hazard Mater* **2021**, *404*, 124082, doi:10.1016/j.jhazmat.2020.124082.

16. Pereira, M.C.; Oliveira, L.C.A.; Murad, E. Iron Oxide Catalysts: Fenton and Fentonlike Reactions – a Review. *Clay Minerals* **2012**, *47*, 285–302, doi:10.1180/claymin.2012.047.3.01.
17. Munoz, M.; de Pedro, Z.M.; Casas, J.A.; Rodriguez, J.J. Preparation of Magnetite-Based Catalysts and Their Application in Heterogeneous Fenton Oxidation – A Review. *Applied Catalysis B: Environmental* **2015**, *176–177*, 249–265, doi:10.1016/j.apcatb.2015.04.003.
18. Oturan, M.A.; Aaron, J.-J. Advanced Oxidation Processes in Water/Wastewater Treatment: Principles and Applications. A Review. *Critical Reviews in Environmental Science and Technology* **2014**, *44*, 2577–2641, doi:10.1080/10643389.2013.829765.
19. Nidheesh, P.V. Graphene-Based Materials Supported Advanced Oxidation Processes for Water and Wastewater Treatment: A Review. *Environ Sci Pollut Res* **2017**, *24*, 27047–27069, doi:10.1007/s11356-017-0481-5.
20. Ma, J.; Yang, M.; Yu, F.; Chen, J. Easy Solid-Phase Synthesis of pH-Insensitive Heterogeneous CNTs/FeS Fenton-like Catalyst for the Removal of Antibiotics from Aqueous Solution. *Journal of Colloid and Interface Science* **2015**, *444*, 24–32, doi:10.1016/j.jcis.2014.12.027.
21. Zubir, N.A.; Yacou, C.; Motuzas, J.; Zhang, X.; Zhao, X.S.; Costa, J.C.D. da The Sacrificial Role of Graphene Oxide in Stabilising a Fenton-like Catalyst GO–Fe3O4. *Chem. Commun.* **2015**, *51*, 9291–9293, doi:10.1039/C5CC02292D.
22. Suárez-Iglesias, O.; Collado, S.; Oulego, P.; Díaz, M. Graphene-Family Nanomaterials in Wastewater Treatment Plants. *Chemical Engineering Journal* **2017**, *313*, 121–135, doi:10.1016/j.cej.2016.12.022.
23. de Aguiar, G.C.; Batalha, D.C.; Fajardo, H.V.; Filho, J.B.G.; Bruziquesi, C.G.O.; de Oliveira, L.C.A.; Gonçalves, M.A.; Ramalho, T. de C.; Silva, A.C. Thioanisole Oxidation Promoted by New Niobium-Based Catalyst: The Effect of Surface Hydroxyl Groups on Catalytic Performance. *Korean J. Chem. Eng.* **2023**, *40*, 2434–2441, doi:10.1007/s11814-023-1447-6.
24. Landfester, K.; Ramírez, L.P. Encapsulated Magnetite Particles for Biomedical Application. *Journal of Physics: Condensed Matter* **2003**, *15*, S1345–S1345, doi:10.1088/0953-8984/15/15/304.
25. Martínez-Mera, I.; Espinosa-Pesqueira, M.E.; Pérez-Hernández, R.; Arenas-Alatorre, J. Synthesis of Magnetite (Fe3O4) Nanoparticles without Surfactants at Room Temperature. *Materials Letters* **2007**, *61*, 4447–4451, doi:10.1016/j.matlet.2007.02.018.
26. Mugutkar, A.B.; Gore, S.K.; Mane, R.S.; Patange, S.M.; Jadhav, S.S.; Shaikh, S.F.; Al-Enizi, A.M.; Nafady, A.; Thamer, B.M.; Ubaidullah, M. Structural Modifications in Co–Zn Nanoferrites by Gd Substitution Triggering to Dielectric and Gas Sensing Applications. *Journal of Alloys and Compounds* **2020**, *844*, 156178–156178, doi:10.1016/J.JALLCOM.2020.156178.
27. Besenhard, M.O.; LaGrow, A.P.; Hodzic, A.; Kriechbaum, M.; Panariello, L.; Bais, G.; Loizou, K.; Damilos, S.; Margarida Cruz, M.; Thanh, N.T.K.; et al. Co-Precipitation Synthesis of Stable Iron Oxide Nanoparticles with NaOH: New Insights and Continuous Production via Flow Chemistry. *Chemical Engineering Journal* **2020**, *399*, 125740, doi:10.1016/j.cej.2020.125740.
28. Synthesis and Characterization of Magnetite Nanoparticles via the Chemical Co-Precipitation Method. *Materials Science and Engineering: B* **2012**, *177*, 421–427, doi:10.1016/j.mseb.2012.01.003.

29. Iida, H.; Takayanagi, K.; Nakanishi, T.; Osaka, T. Synthesis of Fe3O4 Nanoparticles with Various Sizes and Magnetic Properties by Controlled Hydrolysis. *J Colloid Interface Sci* **2007**, *314*, 274–280, doi:10.1016/j.jcis.2007.05.047.
30. Kim, D.K.; Zhang, Y.; Voit, W.; Rao, K.V.; Muhammed, M. Synthesis and Characterization of Surfactant-Coated Superparamagnetic Monodispersed Iron Oxide Nanoparticles. *Journal of Magnetism and Magnetic Materials* **2001**, *225*, 30–36, doi:10.1016/S0304-8853(00)01224-5.
31. Valenzuela, R.; Fuentes, M.C.; Parra, C.; Baeza, J.; Duran, N.; Sharma, S.K.; Knobel, M.; Freer, J. Influence of Stirring Velocity on the Synthesis of Magnetite Nanoparticles (Fe3O4) by the Co-Precipitation Method. *Journal of Alloys and Compounds* **2009**, *488*, 227–231, doi:10.1016/J.JALLCOM.2009.08.087.
32. Sun, X.; Zheng, C.; Zhang, F.; Yang, Y.; Wu, G.; Yu, A.; Guan, N. Size-Controlled Synthesis of Magnetite (Fe3O4) Nanoparticles Coated with Glucose and Gluconic Acid from a Single Fe(III) Precursor by a Sucrose Bifunctional Hydrothermal Method. *J. Phys. Chem. C* **2009**, *113*, 16002–16008, doi:10.1021/jp9038682.
33. Javed, R.; Zia, M.; Naz, S.; Aisida, S.O.; Ain, N. ul; Ao, Q. Role of Capping Agents in the Application of Nanoparticles in Biomedicine and Environmental Remediation: Recent Trends and Future Prospects. *Journal of Nanobiotechnology* **2020**, *18*, 172, doi:10.1186/s12951-020-00704-4.
34. Gulati, S.; Sachdeva, M.; Bhasin, K.K. Capping Agents in Nanoparticle Synthesis: Surfactant and Solvent System. *AIP Conference Proceedings* **2018**, *1953*, 030214, doi:10.1063/1.5032549.
35. Dheyab, M.A.; Aziz, A.A.; Jameel, M.S.; Noqta, O.A.; Khaniabadi, P.M.; Mehrdel, B. Simple Rapid Stabilization Method through Citric Acid Modification for Magnetite Nanoparticles. *Sci Rep* **2020**, *10*, 10793, doi:10.1038/s41598-020-67869-8.
36. Mikelashvili, V.; Kekutia, S.; Markhulia, J.; Saneblidze, L.; Maisuradze, N.; Kriechbaum, M.; Almásy, L. Synthesis and Characterization of Citric Acid-Modified Iron Oxide Nanoparticles Prepared with Electrohydraulic Discharge Treatment. *Materials (Basel)* **2023**, *16*, 746, doi:10.3390/ma16020746.
37. Singh, A.; Lenin, R.; Bari, N.K.; Bakli, C.; Bera, C. Mechanistic Insights into Surface Contribution towards Heat Transfer in a Nanofluid. *Nanoscale Adv 2*, 3507–3513, doi:10.1039/d0na00452a.
38. Saladino, G.M.; Hamawandi, B.; Demir, M.A.; Yazgan, I.; Toprak, M.S. A Versatile Strategy to Synthesize Sugar Ligand Coated Superparamagnetic Iron Oxide Nanoparticles and Investigation of Their Antibacterial Activity. *Colloids and Surfaces A: Physicochemical and Engineering Aspects* **2021**, *613*, 126086, doi:10.1016/j.colsurfa.2020.126086.
39. Mahato, N.; Sharma, K.; Sinha, M.; Baral, E.R.; Koteswararao, R.; Dhyani, A.; Hwan Cho, M.; Cho, S. Bio-Sorbents, Industrially Important Chemicals and Novel Materials from Citrus Processing Waste as a Sustainable and Renewable Bioresource: A Review. *Journal of Advanced Research* **2020**, *23*, 61–82, doi:10.1016/J.JARE.2020.01.007.
40. Ramesh, P.I.; Ali, M.S.; Ghosh, S.; Babu Tatina, M. Citric Acid Mediated Simple and Stereoselective Synthesis of O-Linked Glycosides by Ferrier Rearrangement. *Results in Chemistry* **2022**, *4*, 100347–100347, doi:10.1016/J.RECHEM.2022.100347.
41. Bhaumik, P.; Dhepe, P.L. Solid Acid Catalyzed Synthesis of Furans from Carbohydrates. *Catalysis Reviews* **2016**, *58*, 36–112, doi:10.1080/01614940.2015.1099894.

42. Schwaminger, S.P.; Syhr, C.; Berensmeier, S. Controlled Synthesis of Magnetic Iron Oxide Nanoparticles: Magnetite or Maghemite? *Crystals* **2020**, *10*, 214, doi:10.3390/cryst10030214.
43. P. Schwaminger, S.; Bauer, D.; Fraga-García, P.; E. Wagner, F.; Berensmeier, S. Oxidation of Magnetite Nanoparticles: Impact on Surface and Crystal Properties. *CrystEngComm* **2017**, *19*, 246–255, doi:10.1039/C6CE02421A.
44. Basset, K.; Domenichini, B.; Merle, J.; Perriat, P.; Bourgeois, S. Surface Composition Analysis during the Oxidation of Ferrites: A Necessity. *The European Physical Journal - Applied Physics* **1998**, *4*, 157–159, doi:10.1051/EPJAP:1998255.
45. Guijarro, N.; Bornoz, P.; Prévot, M.; Yu, X.; Zhu, X.; Johnson, M.; Jeanbourquin, X.; Le Formal, F.; Sivula, K. Evaluating Spinel Ferrites MFe2O4 (M = Cu, Mg, Zn) as Photoanodes for Solar Water Oxidation: Prospects and Limitations. *Sustainable Energy & Fuels* **2017**, *2*, 103–117, doi:10.1039/C7SE00448F.
46. Klekotka, U.; Satuła, D.; Basa, A.; Kalska-Szostko, B. Importance of Surfactant Quantity and Quality on Growth Regime of Iron Oxide Nanoparticles. *Materials (Basel)* **2020**, *13*, 1747, doi:10.3390/ma13071747.
47. Cheng, W.; Tang, K.; Qi, Y.; Sheng, J.; Liu, Z. One-Step Synthesis of Superparamagnetic Monodisperse Porous Fe3O4 Hollow and Core-Shell Spheres. *J. Mater. Chem.* **2010**, *20*, 1799–1805, doi:10.1039/B919164J.
48. Xiong, Z.; Sun, Z.-B.; Zheng, M.-L.; Cao, Y.-Y.; Jin, F.; Chen, W.-Q.; Zhao, Z.-S.; Duan, X.-M. A Facile Method for the Room-Temperature Synthesis of Water-Soluble Magnetic Fe3O4 Nanoparticles: Combination of in Situ Synthesis and Decomposition of Polymer Hydrogel. *Materials Chemistry and Physics* **2011**, *130*, 72–78, doi:10.1016/j.matchemphys.2011.05.083.
49. Karthick, A.; Roy, B.; Chattopadhyay, P. Comparison of Zero-Valent Iron and Iron Oxide Nanoparticle Stabilized Alkyl Polyglucoside Phosphate Foams for Remediation of Diesel-Contaminated Soils. *Journal of Environmental Management* **2019**, *240*, 93–107, doi:10.1016/j.jenvman.2019.03.088.
50. Neelgund, G.M.; Oki, A.; Luo, Z. ZnO and Cobalt Phthalocyanine Hybridized Graphene: Efficient Photocatalysts for Degradation of Rhodamine B. *Journal of Colloid and Interface Science* **2014**, *430*, 257–264, doi:10.1016/j.jcis.2014.04.053.
51. Neelgund, G.M.; Oki, A. Graphene-Coupled ZnO: A Robust NIR-Induced Catalyst for Rapid Photo-Oxidation of Cyanide. *ACS Omega* **2017**, *2*, 9095–9102, doi:10.1021/acsomega.7b01398.
52. Xu, C.; Shi, X.; Ji, A.; Shi, L.; Zhou, C.; Cui, Y. Fabrication and Characteristics of Reduced Graphene Oxide Produced with Different Green Reductants. *PLoS One* **2015**, *10*, e0144842, doi:10.1371/journal.pone.0144842.
53. Khalili, D. Graphene Oxide: A Promising Carbocatalyst for the Regioselective Thiocyanation of Aromatic Amines, Phenols, Anisols and Enolizable Ketones by Hydrogen Peroxide/KSCN in Water. *New J. Chem.* **2016**, *40*, 2547–2553, doi:10.1039/C5NJ02314A.
54. Fekri Aval, S.; Akbarzadeh, A.; Yamchi, M.R.; Zarghami, F.; Nejati-Koshki, K.; Zarghami, N. Gene Silencing Effect of SiRNA-Magnetic Modified with Biodegradable Copolymer Nanoparticles on hTERT Gene Expression in Lung Cancer Cell Line: Artificial Cells, Nanomedicine & Biotechnology. *Artificial Cells, Nanomedicine & Biotechnology* **2016**, *44*, 188–193, doi:10.3109/21691401.2014.934456.

55. Ali, A.; Zafar, H.; Zia, M.; Haq, I. ul; Phull, A.R.; Ali, J.S.; Hussain, A. Synthesis, Characterization, Applications, and Challenges of Iron Oxide Nanoparticles. *NSA* **2016**, *9*, 49–67, doi:10.2147/NSA.S99986.
56. Eigler, S.; Dotzer, C.; Hirsch, A.; Enzelberger, M.; Müller, P. Formation and Decomposition of CO2 Intercalated Graphene Oxide. *Chem. Mater.* **2012**, *24*, 1276–1282, doi:10.1021/cm203223z.
57. Acik, M.; Lee, G.; Mattevi, C.; Pirkle, A.; Wallace, R.M.; Chhowalla, M.; Cho, K.; Chabal, Y. The Role of Oxygen during Thermal Reduction of Graphene Oxide Studied by Infrared Absorption Spectroscopy. *J. Phys. Chem. C* **2011**, *115*, 19761–19781, doi:10.1021/jp2052618.
58. Xu, J.; Yang, H.; Fu, W.; Du, K.; Sui, Y.; Chen, J.; Zeng, Y.; Li, M.; Zou, G. Preparation and Magnetic Properties of Magnetite Nanoparticles by Sol–Gel Method. *Journal of Magnetism and Magnetic Materials* **2007**, *309*, 307–311, doi:10.1016/j.jmmm.2006.07.037.
59. Radoń, A.; Drygała, A.; Hawełek, Ł.; Łukowiec, D. Structure and Optical Properties of Fe3O4 Nanoparticles Synthesized by Co-Precipitation Method with Different Organic Modifiers. *Materials Characterization* **2017**, *131*, 148–156, doi:10.1016/j.matchar.2017.06.034.
60. Lima, N.A.; Alencar, L.D.D.S.; Mendonça, G.C.; Mesquita, A.; Silva, A.V.P.; Rosmaninho, M.G.; Taylor, J.G.; Fajardo, H.V.; Moraes, L.C.; Bernardi, M.I.B. *Heterogeneous Catalysis for Thioanisole Oxidation Using Hydrogen Peroxide and Copper, Nickel and Zinc Tungstates Prepared by the Polymeric Precursor Method*; In Review, 2020;
61. WANG, J.L.; XU, L.J. Advanced Oxidation Processes for Wastewater Treatment: Formation of Hydroxyl Radical and Application. *Critical Reviews in Environmental Science and Technology* **2012**, *42*, 251–325, doi:10.1080/10643389.2010.507698.
62. Effect of Band Gap and Particle Size on Photocatalytic Degradation of NiSnO3 Nanopowder for Some Conventional Organic Dyes. *Hybrid Advances* **2023**, *4*, 100079, doi:10.1016/j.hybadv.2023.100079.
63. Murakami, N.; Abe, R.; Prieto Mahaney, O.O.; Torimoto, T.; Ohtani, B. 96 - Photoacoustic Spectroscopic Estimation of Electron Mobility in Titanium(IV) Oxide Photocatalysts. In *Studies in Surface Science and Catalysis*; Eguchi, K., Machida, M., Yamanaka, I., Eds.; Science and Technology in Catalysis 2006; Elsevier, 2007; Vol. 172, pp. 429–432.
64. Kaur, H.; Hippargi, G.; Pophali, G.R.; Bansiwal, A.K. 6 - Treatment Methods for Removal of Pharmaceuticals and Personal Care Products from Domestic Wastewater. In *Pharmaceuticals and Personal Care Products: Waste Management and Treatment Technology*; Prasad, M.N.V., Vithanage, M., Kapley, A., Eds.; Butterworth-Heinemann, 2019; pp. 129–150 ISBN 978-0-12-816189-0.
65. ISO 21348 Definitions of Solar Irradiance Spectral Categories 2020.
66. Prangnell, L. Visible Light-Based Human Visual System Conceptual Model. *ArXiv* **2016**.
67. Fogler, H.S. *Elements of Chemical Reaction Engineering*; Sixth edition.; 2021; ISBN 978-0-13-745943-8.
68. Moussa, N.; Fraile, J.M.; Ghorbel, A.; Mayoral, J.A. Catalytic Oxidation of Thioanisole Ph–S–CH3 over VOx/SiO2 and VOx/Al2O3 Catalysts Prepared by Sol–Gel Method. *Journal of Molecular Catalysis A: Chemical* **2006**, *255*, 62–68, doi:10.1016/j.molcata.2006.04.010.
69. Tojo, S.; Fujitsuka, M.; Majima, T. Structures of 4-Substituted Thioanisole Radical Cations Studied by Time-Resolved Resonance Raman Spectroscopy during Pulse Radiolysis and

Theoretical Calculations. *RSC Advances* **2016**, *6*, 109334–109339, doi:10.1039/C6RA21460F.
70. Saha, D.; Desipio, M.M.; Hoinkis, T.J.; Smeltz, E.J.; Thorpe, R.; Hensley, D.K.; Fischer-Drowos, S.G.; Chen, J. Influence of Hydrogen Peroxide in Enhancing Photocatalytic Activity of Carbon Nitride under Visible Light: An Insight into Reaction Intermediates. *Journal of Environmental Chemical Engineering* **2018**, *6*, 4927–4936, doi:10.1016/j.jece.2018.07.030.
71. Rapado, P.; Faba, L.; Ordóñez, S. Role of the Different Catalytic Sites in the H2O2-Mediated Aqueous-Phase Furfural Partial Oxidation. *Journal of Environmental Chemical Engineering* **2023**, *11*, 111466, doi:10.1016/j.jece.2023.111466.
72. Song, Y.; Xin, F.; Zhang, L.; Wang, Y. Oxidation of Cyclohexene in the Presence of Transition-Metal-Substituted Phosphotungstates and Hydrogen Peroxide: Catalysis and Reaction Pathways. *ChemCatChem* **2017**, *9*, 4139–4147, doi:10.1002/cctc.201700856.
73. Xia, Z.; Baird, L.; Zimmerman, N.; Yeager, M. Heavy Metal Ion Removal by Thiol Functionalized Aluminum Oxide Hydroxide Nanowhiskers. *Applied Surface Science* **2017**, *416*, 565–573, doi:10.1016/j.apsusc.2017.04.095.
74. Masnabadi, N.; Ghasemi, M.H.; Beyki, M.H.; Sadeghinia, M. Oxidative Dimerization of Thiols to Disulfide Using Recyclable Magnetic Nanoparticles. *Research on Chemical Intermediates* **2017**, *43*, 1609–1618, doi:10.1007/s11164-016-2718-1.
75. Sihota, P.; Yadav, R.N.; Dhiman, V.; Bhadada, S.K.; Mehandia, V.; Kumar, N. Investigation of Diabetic Patient's Fingernail Quality to Monitor Type 2 Diabetes Induced Tissue Damage. *Sci Rep* **2019**, *9*, 3193, doi:10.1038/s41598-019-39951-3.

Chapter 4. Conclusions

4.1. Summary of key findings

Sulfur pollutants are commonly found in the air as SO_2 or in wastewater as sulfides, typically originating from sulfur-containing fuel combustion and fuel refining processes in the oil and refinery industries, respectively. Given the continued reliance on fossil fuels as a source of energy, it is crucial to enhance and develop new desulfurization techniques. In this research, GO-iron oxide composites were synthesized and utilized as adsorbents and catalysts, for room-temperature SO_2 removal and sulfide oxidation reactions.

For SO_2 gas removal, the impact of various nanoparticle synthesis methods on the capture capacity of graphene oxide was evaluated. Iron oxide nanoparticles were synthesized using co-precipitation and polyol methods, with NaOH and NH_4OH as reducing agents for the co-precipitation method. TEM analysis revealed that the deposition of nanoparticles did not alter the layered structure of graphene oxide. In the case of nanoparticles from co-precipitation, TEM confirmed the presence of well-dispersed, round-shaped nanoparticles, less than 10 nm in size, on the GO surface. High-resolution XPS analysis led to the identification of the iron oxide nanoparticles as Fe_2O_3. The as-prepared GOFe_2O_3-polyol, GOFe_2O_3-NaOH, and GOFe_2O_3-NH_4 were tested for SO_2 capture at 25°C and a flow rate of 15 mL/min. The breakthrough curves and capture capacity calculations showed enhanced capture with the addition of Fe_2O_3. The highest capture capacity was obtained with the GOFe_2O_3-NH_4 sample, at 3.1 mg $SO_2/g_{sorbent}$, followed by GOFe_2O_3-NaOH, GOFe_2O_3-polyol and GO, with 1.7, 1.3, and 0.6 mg $SO_2/g_{sorbent}$, respectively. The superior capture capacity of GOFe_2O_3-NH_4 was partially attributed to the effective deposition of iron oxide nanoparticles on the GO surface, leading to a higher concentration of nanoparticles. Despite having only 1.3 times more iron than GOFe_2O_3-polyol, GOFe_2O_3-NH_4 achieved a capture capacity 2.4 times higher, thus indicating the influence of the nanoparticle on material performance. The influence was further confirmed by the quantity of SO_2 captured per mass of iron. In that case, GOFe_2O_3-NaOH demonstrated similar performance to GOFe_2O_3-NH_4 relative to the iron content (207.0 and 207.2 mg SO_2/g_{Fe}), despite a lower surface iron concentration (0.81% and 1.52% of Fe wt%, respectively). Additionally, supported nanoparticles were found to have a better capture capacity than bulk iron oxide. The S 2p spectra of GO and Fe 2p of GO-iron oxide indicated the presence of SO_4^{2-} and $FeSO_4$, respectively, before capture. These are associated with

residual sulfur from the synthesis of graphene oxide and the presence of iron in the GO-iron oxide samples. After capture, the amount of SO_4^{2-} increased in all samples, while the amount of $FeSO_4$ slightly increased. This suggests that the adsorbed SO_2 may bond with either the iron or GO. Additionally, SO_2 desorption was found to be incomplete, even at 100°C, indicating a potential combination of physisorption and chemisorption. The adsorbents still kept part of their capture capacity during cycle runs.

The GO-iron oxide composite was also evaluated for its ability to oxidize sulfides, particularly thioanisole. The nanoparticles were synthesized using the co-precipitation method, and the effects of sucrose and citric acid as surfactants on the stability of the nanoparticles over time were explored. Atomic absorption analysis indicated that it was possible to achieve nanoparticles with a Fe^{2+}: Fe^{3+} mass ratio of 1:2 without surfactants. However, the addition of surfactants appeared to slow the increase in Fe^{3+} mass, suggesting that surfactants can slow the oxidation of Fe^{2+} over time. Nanoparticles synthesized with sucrose, which resulted in the least increase in Fe^{3+} mass, were chosen for the subsequent deposition on the GO surface through wet deposition. HRTEM, XRD, and SAED analyses identified the nanoparticles as Fe_3O_4. TEM analysis confirmed the deposition of round-shaped nanoparticles with a size of around 15 nm. FTIR and UV-Vis spectra further confirmed their deposition on the GO surface. The introduction of Fe_3O_4 on GO reduced the direct band gap energy from 3.23 eV to 2.24 eV, suggesting a potential photocatalytic activity under low light energy. GO-Fe_3O_4 was then tested for thioanisole oxidation at 50°C in the presence of H_2O_2 as an oxidizing agent. The material demonstrated catalytic properties by achieving a conversion of thioanisole of 64.2% even without H_2O_2. The photocatalytic activity was evidenced when the UV-catalyst system, without H_2O_2, achieved a thioanisole conversion rate of 89.6% similar to the 92.8% conversion observed with the H_2O_2-catalyst system. Under visible light, the conversion reached 75.2%, suggesting potential for further optimization to enhance performance under visible light conditions. GC-MS and FTIR analyses confirmed the production of sulfone compounds, specifically phenyl benzene sulfinyl sulfone and phenyl disulfone.

4.2. Future work

The GO-iron oxide composite has shown potential as an adsorbent for SO_2 removal and a catalyst for thioanisole oxidation. However, further optimization of the material is required in both applications. Future works for SO_2 removal will focus on investigating the interaction between the adsorbed SO_2 and the material. Characterization techniques such as HR-TEM or XRD are needed to identify the type of Fe_2O_3 produced. Additionally, the influence of temperature and other flue gas components like CO_2, O_2, and moisture, on SO_2 adsorption will be investigated. In the context of catalytic sulfide oxidation, studies will explore how the nanoparticle size could enhance the photocatalytic activity of the GO-Fe_3O_4 material under low-energy light sources like visible light. Furthermore, in both applications, the material's activity should be evaluated over multiple cycles of experiments to ensure its reusability.

Appendices

Experiment setup

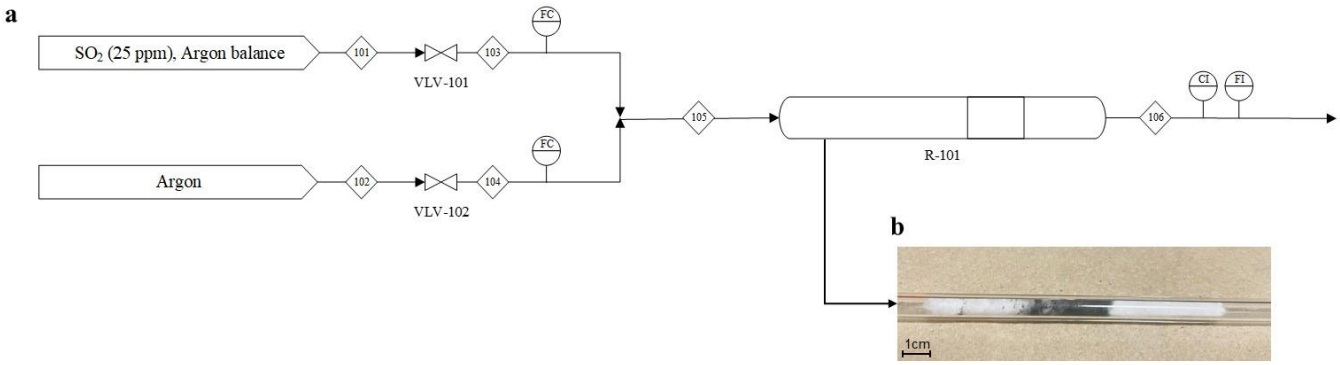

Figure A.1: (a) SO_2 capture setup; (b) quartz tube containing the adsorbent sandwiched between quartz wool.

Additional GO and $GOFe_2O_3$ characterization

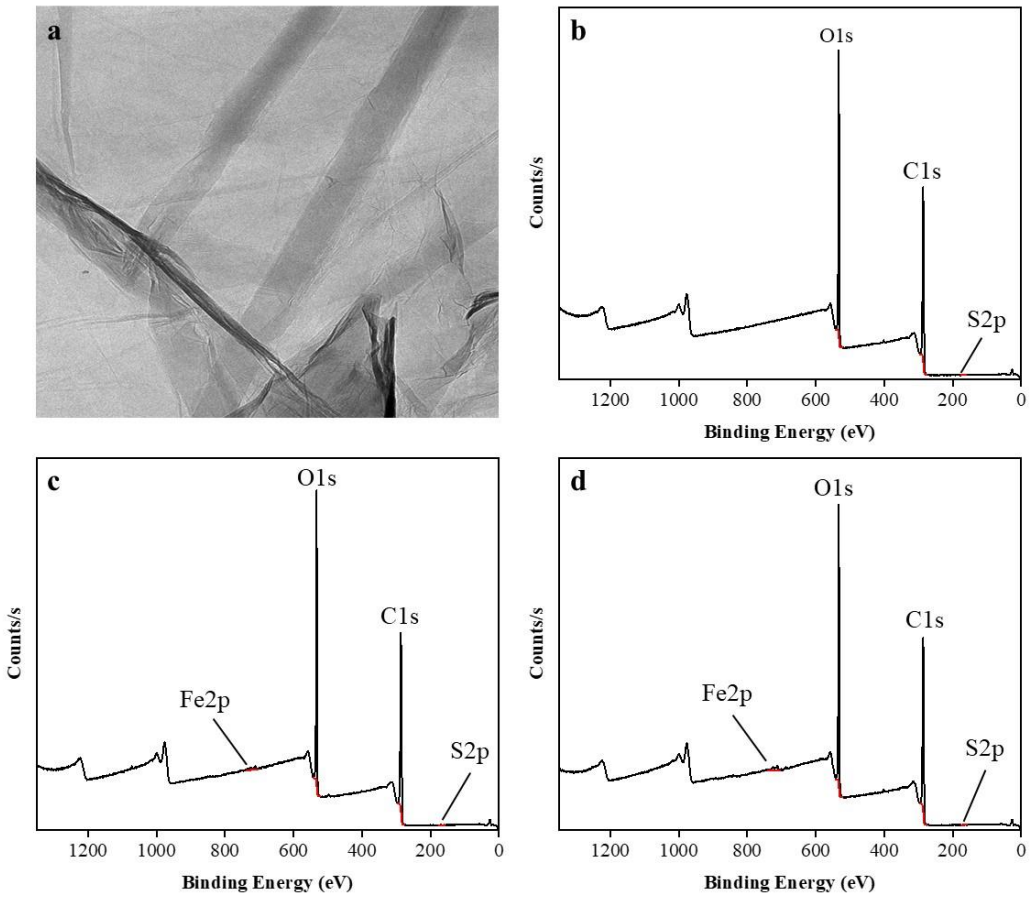

Figure A.2: (a) TEM of pristine GO; XPS survey of (b) GO; (c) $GOFe_2O_3$-NaOH; (d) $GOFe_2O_3$-NH_4.

Breakthrough curve

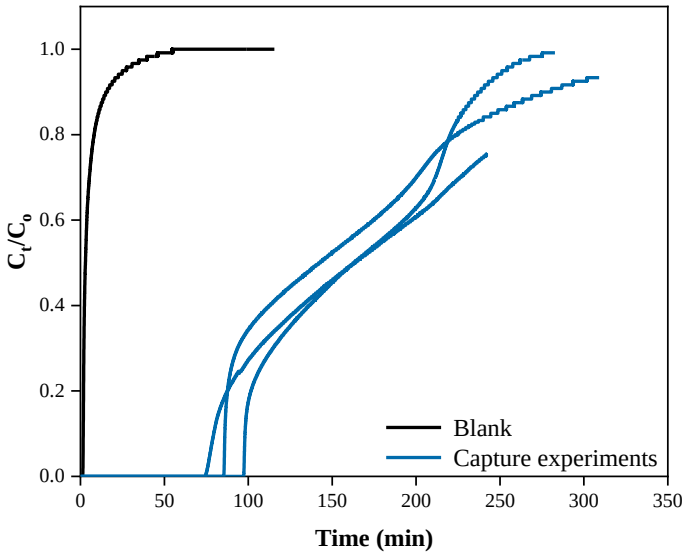

Figure A.3: Breakthrough curves of iron oxide nanoparticles from the co-precipitation method using NaOH as a reducing agent. The SO_2 capture was done at 20°C and 15 mL/min.

Atomic absorption and HPLC calibration curve

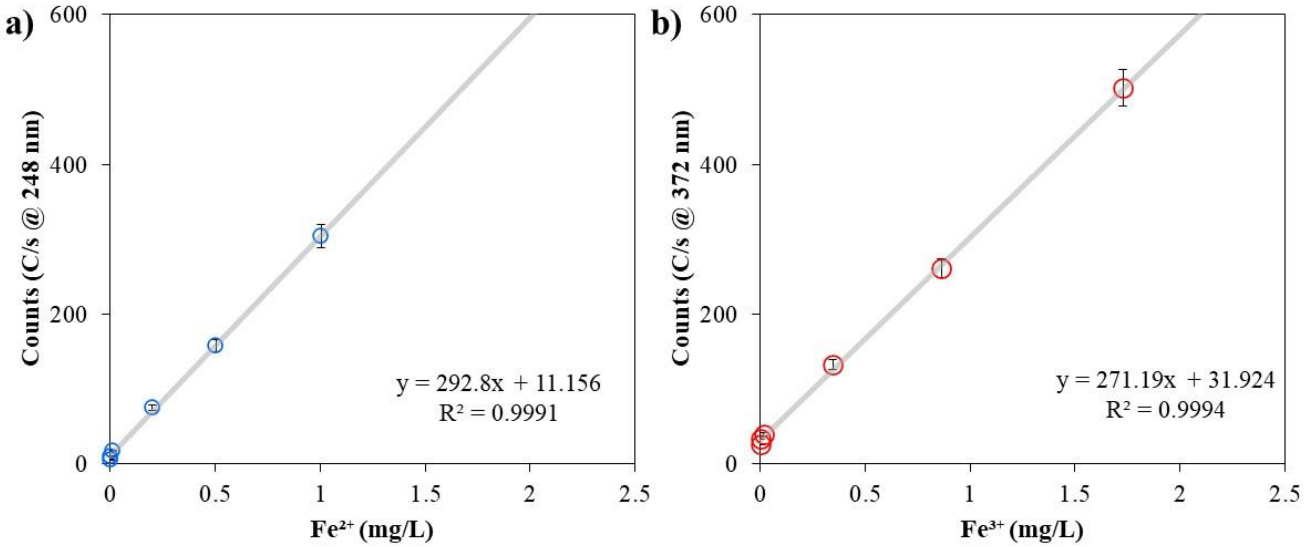

Figure A.4: Atomic adsorption calibration curve for quantification of Fe^{2+} and Fe^{3+} in iron oxide catalysts. Atomic absorption was performed in an Agilent 240 FS AA instrument using a 90/10 acetylene/oxygen mixture (v/v).

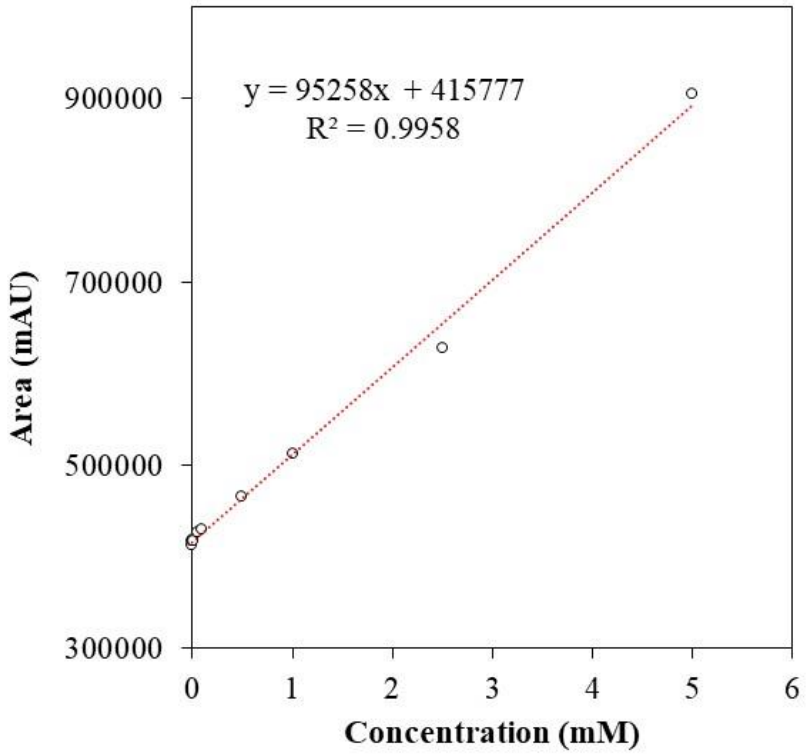

Figure A.5: Calibration curve from HPLC analysis for determining thioanisole concentrations.

The detection of thioanisole was done at 250 nm, a mixture of H_2O:ACN:MIBK:formic acid (50:25:24:01 v/v ratio) was used as the eluent and the runtime was 15 min. The retention time (T_r) was found to be between 5 and 7 min. The area values under the thioanisole peaks were plotted as a function of thioanisole concentrations ranging from 0 to 5 mM.

Sample calculations

Capture capacity calculation

The SO_2 capture capacity was calculated using the following formula:

$$q = \frac{\int (C_i - C_0) dT \times volumetric\ flow\ rate}{masse\ of\ material} \qquad (A.1)$$

The integral term was calculated by subtracting the area under the curve of the sample of the area under the curve of the blank curves.

The area is calculated using the trapezoidal rule:

$$area\ under\ the\ curve = \sum_{t=0}^{t=(t-1)} (0.5 \times (y_1 + y_2) \times (x_1 + x_2) \qquad (A.2)$$

$$Amount\ of\ gas\ adsorbed = blank\ area - sample\ area = a\ (ppm.min) \qquad (A.3)$$

By multiplying the amount adsorbed with the flow rate during the reaction (f) and applying the unit conversion:

$$q = a \times f(ppm.\text{mL}) \times 10^{-6} \frac{\frac{mol\ SO_2}{mol}}{ppm} \times 64 \frac{g\ SO_2}{mol\ SO_2} \times \frac{1mol}{22.4\ L} \times \frac{1L}{10^3 mL} \times \frac{1000mg}{1g}$$

$$q = a \times f(ppm.\text{mL}) \times 2.8571 \times 10^{-6}\ mgSO_2$$

The quantity of SO_2 captured in mg per mass of adsorbent in g will be:

$$q = \frac{a \times f(ppm.\text{mL}) \times 2.8571 \times 10^{-6}\ mgSO_2}{50\ mg\ of\ GOFe_2O_3} \times \frac{1\ mg}{10^{-3}\ g}$$

$$q = a \times f \times 5.714 \times 10^{-5}\ mg_{SO_2}/g_{sorbent}$$

Direct band gap energy calculation:

The absorbance of the material at each wavelength is obtained from the UV-vis spectrum.

$Abs = 0.594$ & $\lambda = 190nm$

$$T = R = 10^{-Abs} = 10^{-0.594} = 0.255$$

$$\alpha = \frac{(1-R)^2}{2R} = 1.09$$

$$\lambda = 1.9 \times 10^{-7} m$$

$$E = \frac{hc}{\lambda} = ((6.62608 \times 10^{-34}) * (2.997925 \times 10^8))/1.9 \times 10^{-7}$$

$$E = 1.05 \times 10^{-18}\ J$$

$$h\upsilon\ (eV) = E\ (J) \times \frac{1\ eV}{1.60218 \times 10^{-19}\ J} = 6.53\ eV$$

$$(\alpha h\upsilon)^2 = (1.09 \times 6.53)^2 = 50.66$$